Transient finite element simulations and experiments on active control of sound transmission loss through plates

Vom Fachbereich Maschinenbau an der
Technischen Universität Darmstadt
zur Erlangung des Grades eines
Doktor-Ingenieurs (Dr.-Ing.)
genehmigte

Dissertation

vorgelegt von

Maarten C. Brink, MSc

aus Oss, den Niederlanden

Berichterstatter:	Prof. Dr-Ing. H. Hanselka
Mitberichterstatter:	Prof. Dr-Ing. R. Nordmann
Tag der Einreichung:	16.10.2007
Tag der mündlichen Prüfung:	23.01.2008

Darmstadt 2008

D 17

For Sonja and my parents

Ottobrunn, den 04.03.2008

Hiermit versichere ich, die vorliegende Doktorarbeit unter der Betreuung von Prof. Dr.-Ing. H. Hanselka nur mit den angegebenen Hilfsmitteln selbständig angefertigt zu haben.

Maarten Brink

Abstract

In this thesis the sound transmission loss of a plate has been investigated. It serves as an abstract model for the noise barrier between engine and passengers in a bus. A finite element simulation model has been developed to be able to predict the plate's noise reduction effect. To increase this reduction without adding too much mass, the integration of active noise control (ANC) has been investigated. The active system contained a controller, microphones and piezoelectric actuators. The influence of this system on the plate's transmission loss has been determined for three noise types: random noise, tonal noise and sweep function.

The transient character of the simulations allows the possibility of directly integrating the ANC algorithm with corresponding sensors and actuators into the simulation model. For that, all controller tasks including sample rate changes and anti-aliasing filtering are included in the simulation algorithm. Doing so, the ANC's critical adaptation phase can be investigated during the simulations. Configuration changes can be tested before the actual noise barrier is built.

The ANC experiments showed very good reduction for the tonal noise and good reduction for the sweep noise. This reduction could be increased even more if the used controller would allow more channels. Due to the stochastic character the reduction of random noise was lower; here only the highest peaks could be reduced. The passive and active simulations were in reasonable agreement with the experimental results. They showed that this simulation approach allows an optimisation of the system before it is constructed and tested experimentally.

Zusammenfassung

Im Rahmen dieser Arbeit wurde der Schalldurchgangsverlust einer Platte, eines abstrakten Modells einer Trennwand zwischen Motor und Fahrgästen eines Busses, untersucht. Dazu wurde unter anderem eine Finite-Elemente-Simulation zur Vorhersage der Schallreduzierung der Platte entwickelt. Zur Steigerung dieser Schallreduzierung ohne viel Gewichtszunahme ist eine Integration mit aktiven Schallreduzierungsmaßnahmen (ANC) betrachtet. Das aktive System bestand aus einem Controller, Mikrofonen und piezoelektrischen Aktuatoren. Die Auswirkungen dieses Systems auf die Schallreduzierung wurde für drei verschiedene Signale bestimmt: stochastisches Rauschen, tonales Rauschen und Frequenzdurchlauf.

Der transiente Aufbau der Simulationen erlaubt die direkte Integration des aktiven Algorithmus mit dazugehörenden Sensoren und Aktuatoren. Dazu werden alle Controlleraufgaben inklusive Abtastrateänderungen und Antialiasing-Filter in das Simulationsmodell integriert. Auf diese Weise kann die kritische Adaptierungsphase während der Simulationen untersucht werden. Konfigurationsänderungen können geprüft werden bevor tatsächlich eine Schalltrennwand gebaut wird.

Die ANC-Experimenten zeigten eine sehr gute Reduzierung bei tonalem Rauschen und eine gute Reduzierung beim Frequenzdurchlauf. Diese Reduzierung könnte zusätzlich verbessert werden, wenn der Controller mehr Kanäle erlauben würde. Die Reduktion beim stochastischen Rauschen war wegen dessen Unvorhersagbarkeit deutlich geringer; nur die höchsten Frequenzspitzen konnten hier verringert werden. Die passiven und aktiven Simulationen stimmten größtenteils mit den Ergebnissen der Experimente überein. Sie zeigten, dass diese Simulationsmethode eine Optimierung des Systems erlaubt bevor dieses realisiert und experimentell getestet wird.

Contents

Symbols and Notation conventions

List of Symbols

a	Downscale factor
b	Damping constant [N s m^{-1}]
$\boldsymbol{B}$	Damping matrix
c_0	Acoustic velocity in air (at room temperature) [m s^{-1}]
c_x	Phase velocity along the $x-$direction [m s^{-1}]
d	Signal at the error sensor (ANC off)
D	Bending stiffness [N m]
$\boldsymbol{D}$	Elasticity matrix
e	Signal at the error sensor (ANC on)
e	Euler's number (≈ 2.718282)
E	Young's modulus [N m^{-2}]
f	Frequency [Hz]
f	Force [N]
f_s	Sample rate [Hz]
F	Fourier transform matrix
g	Plant's impulse response (secondary source to error sensor)
G	Shear modulus [N m^{-2}]
h	Filter signal
h	Thickness [m]
I	Acoustic intensity [W m^-2]
I	Electrical current [A]
I	Moment of inertia [kg m^2]
j	Complex number ($= \sqrt{-1}$)
J	Cost function
J	Number of reference sensors/signals
k	Wavenumber [m^{-1}]
k	Spring constant [N m^{-1}]
K	Number of secondary sources/signals
K	Stiffness matrix
L	Length [m]

L	Buffer length
m	Mass [kg]
M	Mass matrix
M	Number of error sensors/signals
n	Discrete time [s]
N	Number of pressure sources
p	Pressure [Pa]
P	Power [W]
q	Moment [Nm]
Q	Discrete time delay radiation matrix
r	Distance [m]
r	Filtered-reference signal
R	Transmission loss
S	Surface [m^2]
t	Continuous time [s]
T	Strain-displacement matrix
u	Displacement [m]
v	Air particle velocity [ms^{-1}]
V	Volume [m^3]
V	Voltage [V]
w	Adaptive filter
x	Input/reference signal
y	Output signal at the secondary source
y	Mode shape participation factor
Y	Discrete time delay incident diffuse field matrix

$\alpha_{1,2}$	Rayleigh damping factor
β	Leaking ANC factor
β_i	Mode shape weighting factor
γ	Interpolation weighting factor
Γ	Substitution matrix
δ	Kronecker delta
ϵ	Strain
ζ	Time delay integer [s]
η_{hu}	Relative humidity in air
θ	Rotation, moment [Nm]
λ	Wave length [m]
μ	Convergence step-size
ν	Poisson's ratio
π	Circular constant (≈ 3.1415)

ρ	Density [kg m^{-3}]
σ	Stress [N m^{-2}]
τ	Transmission coefficient
Φ	Power spectral density (PSD) [W Hz^{-2}]
ϕ	Mode shape
ψ	Angle or phase
ω	Angular frequency [s^{-1}]
Ω	Angular frequency [s^{-1}]

Notation conventions

$p(t)$	Signal as a function of the continuous-time variable t
$p[n]$	Sampled signal as a function of the discrete-time variable n
$\boldsymbol{A}$	Matrix, filled with elements a_{ij}
$\boldsymbol{A}^{\mathrm{T}}$	Transposed of matrix $\boldsymbol{A}$
$\boldsymbol{A}^{-1}$	Inverse of matrix $\boldsymbol{A}$
$a_{i,j}$	Element in $\mathbf{A}$ at position (i, j): i^{th} row and j^{th} column
$\boldsymbol{b}$	Column vector with coefficients: $[b_1\, b_2\, b_3\, \cdots]^{\mathrm{T}}$
$\hat{\boldsymbol{b}}$	Estimation of the vector $\boldsymbol{b}$
b_i	Coefficient inside vector $\boldsymbol{b}$ at position i
$\boldsymbol{b}_{n+1}$	Column vector $\boldsymbol{b}$ at time $n+1$
$\boldsymbol{b}[n]$	Column vector with elements: $\begin{bmatrix} b[n] & b[n-1]] & b[n-2] & \cdots \end{bmatrix}^{\mathrm{T}}$
$\mathbf{F}$	Fourier transformation matrix
∇	Partial derivative in all (spatial) directions
$\tilde{\boldsymbol{B}}[f_k]$	Discrete Fourier transform of $\boldsymbol{b}[n]$
${u_z}^{(\mathrm{m})}$	Displacement of node m along the z-axis
${u_z}^{(\mathrm{e})}$	Displacement inside element e along the z-axis
$\dot{u}$	Time-derivative of displacement, velocity ($= \partial u/\partial t$)
$\ddot{u}$	Double time-derivative of displacement ($= \partial^2 u/\partial t^2$)
$\theta_x^{(\mathrm{m})}$	Rotation of node m around the x-axis
$\boldsymbol{u}^{(\mathrm{m})}$	DOF vector with displacements and rotations of node m
$\mathrm{E}\{p\}$	Mean or average of p
$\hat{p}$	Estimation of p
$\lfloor a \rfloor$	Floor function which rounds a to the nearest integer downwards
$\tilde{\boldsymbol{\phi}}$	Normalised eigenvector
$\lvert a \rvert$	Absolute value of a

Chapter 1

Introduction

With the constant development of lighter vehicle constructions to save precious fuel and reduce exhaust gases, the noise that propagates to its passengers is an increasing problem. The mass reduction of a partition between passenger and engine consequently leads to more unwanted acoustic transmission. To make it more pleasurable for the passengers to use the means of transport, extra mass in ways of acoustic damping has to be added. A measure that partly overrides the benefits of lighter constructions[1]. This problem asks for intelligent ways of noise control, preferably lightweight.

A solution to this noise problem could be the integration of active noise control (ANC). Actuators on or near a lightweight barrier can be used in such a way that they further reduce the noise that is transmitted trough the barrier using destructive interference. Goal always is a region of silence around the people that are affected by the noise.

Thus using this technique to increase the transmission loss of a plate, one can attach actuators to the plate and excite vibrations in such a way that the sound pressure level behind it is reducing (Fuller [23]). In this Active Structural Acoustic Control (ASAC) approach of ANC an increase in mass of the structure is usually unwanted. To still be able to excite structural vibrations, often actuators made of piezoceramic material are used. These crystalline materials have the ability of converting electrical into mechanical energy and vice versa and deform when an electric field if applied. Fixed on a surface as thin PVDF (polyvvinylidene fluoride) film sheets or thicker PZT (lead zirconate titanate) patches they can introduce bending (Rosen [50]).

The combination of ANC and transmission loss has been the topic of many investigations. Approaches vary from piezoelectric patches on the structure (Al-Bassyiouni [3]), PVDF-films on the surfaces (Henrioulle [26]), smart foams that not only introduce vibrations but also radiate noise (Akl [2]), active mounts that can introduce structural translation and rotation (Tewes [52]), adaptive tuned vibration absorbers (Carneal [16]) and, in case of double wall partitions, actuators between the plates for active cavity control (Fonseca [22]).

[1] An increase of 100 kg of the mass of a normal passenger car leads to an extra fuel usage of about 1 litre per 100 km.

Computer simulations play an increasingly important role in the design of new products (Bathe [5]). To reduce development time and costs, effort is made to completely simulate its structural behaviour before any part is actually constructed. The advantage will be that design errors can be discovered and corrected in an early stage; passenger comfort can be optimised and no expensive production changes are needed.

For a representative simulation of vehicle acoustic behaviour, the reduction of sound transmitted through, for example, an engine partition needs to be predicted. To be able to simulate the behaviour of such a partition with ANC installed, the actuators, the sensors as well as the algorithm itself need to be implemented into the model. If successful, it can be predicted how profitable an ANC system with specific parameters will be.

To predict the transmission loss of a rectangular plate, a number of analytical approaches is available. Some are based on the noise transmission through infinite plates not considering modes (Beranek [8]), others predict a "worst-case" transmission loss (Fahy [21]). If the partition would not have a standard shape like a rectangle, an analytical solution gets more complicated. The same goes if actuators for future active control need to be integrated into the model. In this case the finite element method (FEM) looks more promising.

Disadvantage of FEM is that the simulation of noise propagation through air is a tremendous effort. Expanding the structural model with fluid elements is possible, but the model size, and therefore the calculation time, increases exponentially. Simulation of noise into the far-field will be an almost impracticable task, and possible unwanted reflections at the boundaries of the simulated air-space will disturb the simulation.

A technique that solves the difficulties of simulating acoustic radiation is the Boundary Element Method (BEM) (Estorff [20]). Using this technique, only the radiated surface has to be discretised and acoustic radiation is calculated by numerical integration applying the theorems of Green, Gauss and Stokes (Beer [6]). Also the acoustic radiation towards a structure can be simulated using BEM, and the response of the structure can be calculated if one combines the methods of FEM and BEM. This way the transmission loss of a partition can be predicted for the lower-frequency area (Sysnoise [37]).

In case of increasing frequency the simulation methods mentioned require smaller elements and thus more calculation time. To efficiently predict the sound transmission through a structure in the high-frequency area (above approx. 1 kHz) the Statistical Energy Analysis (SEA) can be used (AutoSEA [55]). It presumes a high modal density and therefore is less accurate for the frequency area in which FEM and BEM work well.

A way to numerically predict the transmission loss of a partition only using the finite element method is proposed by Ackermann ([1]). It consists of a model with two boxes of air and the partition of interest in between. This approach works reasonably well for thick

wall partitions for which the element size of the model can be relatively large. For thin panels the resonance wavelengths for the same frequency area are generally shorter and therefore the elements need to be smaller. The presence of an additional larger amount of air elements considerably increases the model size and slows down the solving process.

Instead, a different approach will be proposed in which the FE model that is used does not contain any air elements. Acoustic radiation to and from the plate is calculated during the pre- and postprocessing phase by solving the Huygens-Rayleigh integral and is not a part of the equation of motion to be solved. Radiation equations are transformed into single matrix multiplications leading to an efficient and time-inexpensive calculation of the acoustic radiation. The FE model is created in such a way that the simulations can be verified by standardised transmission loss measurements.

The advantage of this proposed model will mainly be speed. Being able to quickly solve the equation of motion, the simulation of the plate's behaviour in the time domain will be more efficient; for every simulated time step the FE equations have to be solved, which would be very time-consuming for large models. The great advantage of this time-domain simulation is that ANC algorithms, which are mostly in the time-domain too, can be easily integrated into the FE model. Now a possible ANC application and its behaviour and structural response can be investigated before actually being built.

A structural simulation with integrated control system can overcome the shortcoming that other ANC-FEM investigations have. An often used investigation approach determines the frequency responses from control actuators and structure to control sensors inside FEM/BEM. These responses are exported to a different programme that simulates the control system (Johnson [35]). Also FEM modal analysis results can be exported to be used for ANC simulation outside the finite element environment (Oude Nijhuis [45]). Disadvantage of these approaches is the use of two separated and uncoupled simulation programmes to describe a single measurement procedure. Other investigation methods are only able to predict the best possible reduction and can not describe the adaptation phase which should lead to this optimised state (Henrioulle [26]). The proposed ANC integration using transient FEM offers the advantages of having a single simulation programme and being able to look into the optimisation process of the algorithm. Aspects as stability, robustness and adaptation speed can now be investigated and improved.

This dissertation will start by discussing three major fields: transmission loss, active noise control and finite element simulation (Chapter 2-4). With the obtained knowledge the experiments and simulations are prepared (Chapter 5). The results of those experiments and simulations are presented next (Chapter 6) and the last chapter contains a summary of the work that is done, conclusions and recommendations for future work (Chapter 7).

Chapter 2

Sound Transmission Loss

2.1 Introduction

One of the major fields of research for the acoustic engineer is reducing unwanted noise. If produced by machinery, its workers need to be protected. If produced by a vehicle, its passengers prefer the comfort of low-noise transportation, so they can decide themselves what to hear. People that live close to main roads, railway tracks, industries and airports often suffer from health problems due to the exposure to noise.

The most effective way to solve a problem is to tackle its source. If the problem is noise, the best solution is, of course, reducing the output of the noise source. If a further reduction of the emitted noise is not possible anymore or economically inefficient, the second-best solution would be isolating the source. If isolated by a closed barrier, the sound waves first need to pass this obstruction before arriving at the observer; inevitably losing a part of their energy.

The determination of *sound transmission loss* through partitions plays an important role in acoustics. Through measurements and/or calculations the energy reduction that sound waves undergo if travelling through the barrier is determined. To be able to compare different materials and set-ups, an international standard procedure for the measurements exists (ISO 140 [29]). These standards contain a list of requirements for the laboratory rooms, the aperture in which the test specimen is built and the way the data is obtained and processed.

This chapter will explain the theory of acoustic transmission through plates. Throughout the rest of this thesis some equations from this chapter will be used to predict transmission loss values. Other equations will be used for measurement post-processing.

Usually, the transmission loss is represented in 1/3-octave bands, where, instead of a *narrowband* representation, the acoustic energy is summed for bands around certain frequencies (IEC 61260 [28]). One of the reasons for this is to mask the poor modal density

in the low frequency area of reverberation rooms. This 1/3-octave band processing makes it more easy to compare results with measurements done in other laboratories. Disadvantages is that interesting narrowband information disappears. In this thesis, where all measurements are done in the same laboratory and using the same installation, the results are often presented in both band filtered and narrowband diagrams, so possible narrowband changes can be investigated.

2.2 Analytical prediction of transmission loss

The sound transmission loss or *reduction index* R of a partition or plate is defined as ten times the common logarithm of the sound power incident on the plate, divided by the sound power transmitted by the plate (see Eq. 2.1) (ISO 140 [29]).

Instead of using the sound power, the transmission loss can also be described by the ratio between incident and transmitted intensity ($I_{\text{inc}}/I_{\text{trans}}$) or by the reciprocal of the transmission coefficient τ (Beranek [8]):

$$R = 10\log\left(\frac{W_{\text{inc}}}{W_{\text{trans}}}\right) = 10\log\left(\frac{I_{\text{inc}}}{I_{\text{trans}}}\right) = 10\log\left(\frac{1}{\tau}\right) \qquad \text{dB}, \tag{2.1}$$

where the sound power W is the integral of the intensity over the surface S of the partition:

$$W = \int I \ \mathrm{d}S$$

and this (average) intensity is (Boone [12]):

$$I = \mathrm{E}\{p(t)\}_{\text{RMS}}\mathrm{E}\{v_{\text{n}}(t)\}_{\text{RMS}}. \tag{2.2}$$

Here $p(t)$ is the time-dependent acoustic pressure[1], v_{n} is the velocity in the direction normal to the surface and $\mathrm{E}\{\dots\}$ is the *expectation operator* or *mean* (Papoulis [46]). Practically, the *root-mean-square* of the pressure, written as $\mathrm{E}\{p(t)\}_{\text{RMS}}$, is determined over a certain length of time T as follows:

$$\mathrm{E}\{p(t)\}_{\text{RMS}} = \sqrt{\frac{1}{T}\int_0^T p^2(t)\mathrm{d}t}.$$

For a *plane harmonic wave* in air, incoming under an angle ψ with the normal of the plane, the intensity becomes (Boone [11]):

[1] In acoustics the pressure p in Pascal as a function of time t is a fluctuation from the ground state: it is the real time-dependent pressure p_{real} minus the static pressure p_{static}:

$$p(t) = p_{\text{real}}(t) - p_{\text{static}}$$

$$I_{\text{inc}}(\psi) = \frac{1}{2}\rho_0 c_0 v_{\text{n},0}^2 \cos(\psi) = \frac{1}{2}\frac{p_0^2}{\rho_0 c_0}\cos(\psi), \tag{2.3}$$

with for $v_{\text{n},0}$ the amplitude of the particle velocity in direction of the normal of the plane, for p_0 the amplitude of the pressure wave, for ρ_0 the density of air and c_0 is the propagation velocity of acoustic waves in air.

2.2.1 Transmission loss of infinite plates

The term *infinite plate* is often used in structural acoustics to denote a situation without boundary conditions and consequently without structural resonance modes. Although physically not possible, it can be a good model for a finite plate with high damping or with damped boundaries. Being resonance free, the wave equation and its interaction with the surrounding air is less complicated to describe.

Although more types of waves inside a thin plate are possible, this thesis will only discuss the *flexural* or *bending waves*, the plate vibrations with out-of-plane amplitude that are mainly responsible for the radiated noise. Amplitudes are assumed small compared to the plate's thickness and shear displacements due to shearing forces are neglected, which means that plane cross sections remain plane during bending deformation. Strain and stress are considered linear and the normal stress with direction perpendicular to the plane is neglected (Fahy [21]).

Bending waves

Let's presume a homogeneous isotropic infinite plate in the $x, y-$plane ($z = 0$) with thickness h and density ρ. The equation of this two-dimensional free bending wave is given as (Cremer [17]):

$$\left(D\nabla^4 + \rho h \frac{\partial^2}{\partial t^2}\right) u_z(x, y, t) = 0, \tag{2.4}$$

with for u_z a displacement in the z-direction, depending on the location (x, y) and on time t. The Laplace operator ∇^2 for our two-dimensional waves is defined as:

$$\nabla^2 \equiv \frac{\partial^2}{\partial x^2} + \frac{\partial^2}{\partial y^2},$$

and D is the *bending stiffness*:

$$D = \frac{Eh^3}{12(1-\nu^2)}.$$

Here ν is Poisson's ratio, a material constant and measure for the contraction of a material in one direction due to stretch in the other direction. In the case of bending plates, it determines the curvature of the plate perpendicular to the bending direction. The Young's modulus E, describes the stiffness of the material. Damping can be introduced by making E complex.

A simple harmonic damping-free plane bending wave in the space-frequency domain can be described by:

$$\tilde{U}(x, y, \omega) = U_0(\omega)\, \mathrm{e}^{-\mathrm{j}(k_x x + k_y y)} \tag{2.5}$$

with for $U_0(\omega)$ the amplitude[2] depending on the angular frequency ω, and k_x and k_y are the wavenumbers in the x- and y-direction respectively. The tilde sign ($\tilde{}$) tells us that we are in the frequency-domain. Wavenumber k is defined as:

$$k \equiv \frac{\omega}{c} = \frac{2\pi}{\lambda}$$

with $\omega \equiv 2\pi f$, f is the frequency, c is the propagation velocity and λ is the wavelength (see Fig. 2.1).

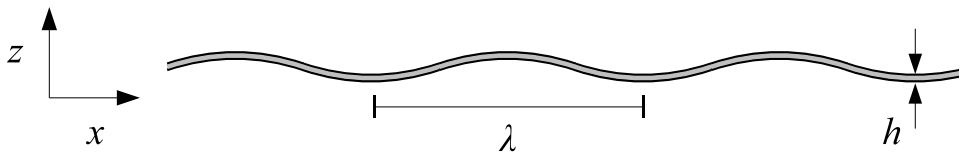

Figure 2.1: Cross-sectional view of a free bending wave in a plate with thickness h. The amplitude in the z-direction is highly exaggerated.

Using Eq. 2.5 and solving the space and time derivatives of Eq. 2.4 it becomes (Soedel [51]):

$$\left(Dk_b^4 - \rho h \omega^2\right)\tilde{U}(x, y, \omega) = 0. \tag{2.6}$$

For this equation the following frequency-domain time-derivative rule is used (see also paragraph 4.4.2 and Oppenheim [44]):

$$\frac{\partial}{\partial t}\tilde{U} \leftrightarrow \mathrm{j}\omega\tilde{U}$$

and the two wavenumbers in direction x and y are replaced by a single wavenumber in direction of propagation using the following equation (Fahy [21]):

$$k_b^2 = k_x^2 + k_y^2. \tag{2.7}$$

The wavenumber k_b of this 2D-bending wave can be solved from Eq. 2.6 and is:

$$k_b = \sqrt[4]{\frac{\rho h}{D}}\,\sqrt{\omega} = \sqrt[4]{\frac{12\rho\left(1-\nu^2\right)}{E}}\,\sqrt{\frac{\omega}{h}}. \tag{2.8}$$

[2]For notation convenience the vibration direction z is omitted in the displacement notations.

As we can see, the bending wavenumber depends on the square root of the frequency, an important difference with acoustic waves in air for which a linear dependency exists. This means that also the propagation velocity depends on the frequency, a typical property of bending waves which is called *dispersion* (Brink [14]).

Plane wave incidence

So far the right hand side of the bending wave equation 2.6 is left zero, meaning a free plane bending wave without any source. If a plane acoustic wave with angle ψ with the plate's normal falls in, a pressure difference appears between both sides of the plate. This pressure difference $\Delta\tilde{P}(x, y, \omega)$ between both sides of the plate at $z = 0$ is the source for *forced* bending waves (see Fig. 2.2):

$$\left(Dk_b^4 - \rho h\omega^2\right)\tilde{U}(x, y, \omega) = \Delta\tilde{P}. \tag{2.9}$$

The incoming acoustic plane wave can be written as:

$$\tilde{P}_\mathrm{i}(x, y, z, \omega) = P_0\, \mathrm{e}^{-\mathrm{j}(k_x x + k_y y + k_z z)}\, \mathrm{e}^{\mathrm{j}(\omega t + \phi)}, \tag{2.10}$$

and if we choose our coordinate system such that this wave is parallel to the y-axis, the wavenumber k_y falls out and this equation becomes:

$$\tilde{P}_\mathrm{i}(x, z, \omega) = P_0\, \mathrm{e}^{-\mathrm{j}(k_x x + k_z z)}\, \mathrm{e}^{\mathrm{j}(\omega t + \phi)}. \tag{2.11}$$

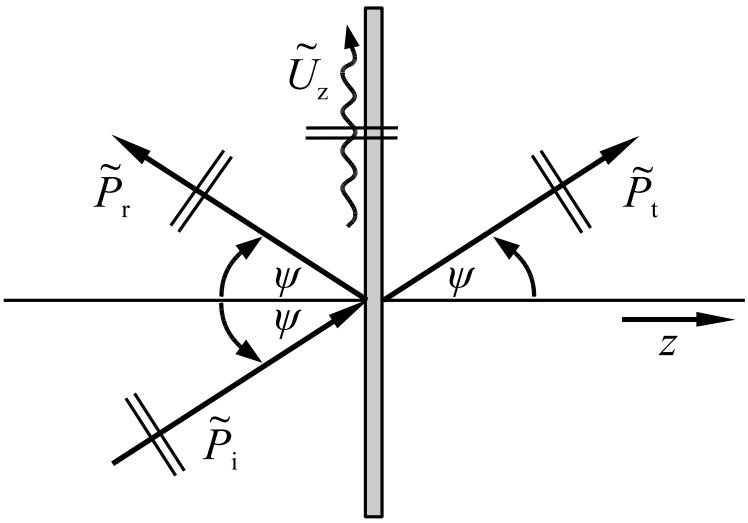

Figure 2.2: Sound transmission by a forced bending wave. A plane wave $\tilde{P}_\mathrm{i}$ comes in with angle ψ, is partly reflected ($\tilde{P}_\mathrm{r}$) and, due to a forced plane bending wave $\tilde{U}_z$, partly transmitted ($\tilde{P}_\mathrm{t}$).

We can say for the pressure difference at the plate's surface, which is the sum of the incoming wave $\tilde{P}_i$ and reflected[3] wave $\tilde{P}_r$ minus the transmitted wave $\tilde{P}_t$:

$$\Delta\tilde{P} = \tilde{P}_\mathrm{i} + \tilde{P}_\mathrm{r} - \tilde{P}_\mathrm{t}. \tag{2.12}$$

We can also say that the plate's normal velocity $\dot{\tilde{U}}_z$ has to be the same as the air particle normal velocity $\tilde{V}_z$ at both the left and the right side of the plate:

$$\begin{aligned} \tilde{V}_{\mathrm{left},z} &= \dot{\tilde{U}}_z &&= \tilde{V}_{\mathrm{right},z} \\ &\downarrow \\ \tilde{V}_{\mathrm{i},z} - \tilde{V}_{\mathrm{r},z} &= \mathrm{j}\omega\tilde{U}_z &&= \tilde{V}_{\mathrm{t},z}. \end{aligned} \tag{2.13}$$

The normal direction part of the particle velocity of a plane wave in air written in the space-frequency domain is (Boone [12]):

$$\tilde{V}_z(x,y,\omega) = \frac{1}{\rho_0 c_0}\tilde{P}(x,y,\omega)\cos(\psi) \tag{2.14}$$

and, combining the last equations, we obtain the following equalities:

$$\begin{aligned} \tilde{P}_\mathrm{i} - \tilde{P}_\mathrm{r} &= \tilde{P}_\mathrm{t} \\ \mathrm{j}\omega\rho_0 c_0\tilde{U}_z &= \tilde{P}_\mathrm{t}\cos(\psi). \end{aligned} \tag{2.15}$$

The plate's bending wave will not have the same wavenumber as a free bending wave at the given ω, but is forced to have the same wavenumber as the plane wave in air at $z = 0$ (see also Eq. 2.10):

$$k_{b,forced} = k_x = k\sin(\psi) = \frac{\omega}{c_0}\sin(\psi), \tag{2.16}$$

where k is the wavenumber of the plane wave in air in direction of propagation.

Inserting Eq. 2.12, Eq. 2.15 and Eq. 2.16 in the bending wave equation Eq. 2.9, we get:

$$\left[D\left(\frac{\omega}{c_0}\right)^4\sin^4(\psi) - \rho h\omega^2\right]\frac{\tilde{P}_\mathrm{t}\cos(\psi)}{\mathrm{j}\omega\rho_0 c_0} = 2\left(\tilde{P}_\mathrm{i} - \tilde{P}_\mathrm{t}\right) \tag{2.17}$$

and solving the fraction $\tilde{P}_\mathrm{i}/\tilde{P}_\mathrm{t}$ out of this equation gives:

$$\frac{\tilde{P}_\mathrm{i}}{\tilde{P}_\mathrm{t}} = 1 + \mathrm{j}\,\frac{\omega\cos(\psi)}{2\rho_0 c_0}\left(\rho h - \frac{D\omega^2\sin^4(\psi)}{c_0^4}\right) \tag{2.18}$$

[3]The reflection of the incoming wave acts according to Snell's law, which says that the incoming angle with the normal of the surface equals the outgoing angle (Boone [11]). For the transmission goes that the angle does not change if the fluid properties on both sides are the same (Fahy [21]).

The transmission coefficient, already introduced in Eq. 2.1, is equal to the transmitted intensity I_{trans} divided by the incident intensity I_{inc}. This is for plane waves with angle ψ:

$$\tau = \frac{I_{\text{trans}}}{I_{\text{inc}}} = \frac{2\rho_0 c_0 |\tilde{P}_{\text{trans}}|^2 \cos(\psi)}{2\rho_0 c_0 |\tilde{P}_{\text{inc}}|^2 \cos(\psi)} = \frac{|\tilde{P}_{\text{trans}}|^2}{|\tilde{P}_{\text{inc}}|^2} = \left| \frac{\tilde{P}_{\text{trans}}}{\tilde{P}_{\text{inc}}} \right|^2 . \tag{2.19}$$

Here $|\tilde{P}|$ is the absolute value of the pressure. In case of the incoming wave it is equal to the amplitude P_0.

And finally, we can write for the transmission loss R due to a plane with with angular frequency ω and incident angle ψ, combining Eq. 2.1, Eq. 2.18 and Eq. 2.19 :

$$R(\omega, \psi) = 10 \log \left[1 + \left(\frac{\omega \cos(\psi)}{2\rho_0 c_0} \right)^2 \left(\rho h - \frac{D\omega^2 \sin^4(\psi)}{c_0^4} \right)^2 \right] \quad \text{dB}. \tag{2.20}$$

Normal, random and field incidence

Normal incidence is the situation where the incident plane wave falls in perpendicular to the plate ($\psi = 0$). In this case the stiffness controlled part of Eq. 2.20 which contains D falls out and R reduces to the *mass law*:

$$R_0(\omega) = 10 \log \left[1 + \left(\frac{\rho h \omega}{2\rho_0 c_0} \right)^2 \right] \quad \text{dB}. \tag{2.21}$$

An important aspect in sound insulation quantification of plates is the transmission loss with *random incidence*. The source side of the plate is in contact with a *diffuse sound field* which, due to multiple reflections, can be seen as a sound field where plane waves are uncorrelated and come from all directions.

Instead of an analytical solution for all frequencies, it is common practise to use an approximation of the transmission loss for frequencies *below the critical frequency* ω_{cr}. This critical frequency depends on the material and thickness of the plate and on the incident angle of the wave. It is defined as the frequency for which the forced bending wave number coincides with the free bending wave number of the plate (Boone [11]). Combining Eq. 2.8 and Eq. 2.16 gives:

$$\frac{\omega_{\text{cr}}}{c_0} \sin(\psi) = \sqrt[4]{\frac{\rho h}{D}} \sqrt{\omega_{\text{cr}}} \tag{2.22}$$

and the critical frequency becomes:

$$\omega_{\text{cr}} = \left(\frac{c_0}{\sin(\psi)} \right)^2 \sqrt{\frac{\rho h}{D}}. \tag{2.23}$$

Often the angle is omitted and with *critical frequency* is meant: the critical frequency for

an incidence of 90^o. It is the minimum frequency for which the phenomenon can occur[4].

Far below the lowest critical frequency, the transmission loss for random incidence is approximated by (Fahy [21], Cremer [17]):

$$R_{\text{random}}(\omega) \approx R_0(\omega) - 10\log\left(0.23R_0(\omega)\right) \qquad \text{dB}, \tag{2.24}$$

where $R_0(\omega)$ is again the transmission loss at normal incidence of Eq. 2.21.

Practically, the ideal situation of a diffuse field on the source side is not reached, and instead of integrating over the full range of ψ from 0^o to 90^o, a maximum of 78^o has become generally accepted (Beranek [8]). This so called *field incidence* results into a low-frequency approximation of the transmission loss of:

$$R_{\text{field}}(\omega) \approx R_0(\omega) - 5 \qquad \text{dB}. \tag{2.25}$$

2.2.2 Transmission loss of finite plates

The boundary free model with infinite plates gives a good insight into bending waves, critical frequency and transmission loss. As a model for a real finite plate it is however not sufficient, the boundaries play an important role that can not be ignored.

A bending wave travelling through a real and finite plate will at some point encounter an edge or a boundary in which the plate is fixed. This sudden change in *impedance*[5] causes the wave to reflect and propagate away from this boundary. It will interfere with other incoming waves or reflections from other boundaries and in time a complex reflection pattern appears.

Modal behaviour

In a steady state situation, the build-up of bending wave reflections in the plate is finished and an energy-stable situation is reached. Due to *destructive* and *constructive interferences* only the waves with wavelengths that "match" the dimensions of the plate remain and form a vibration pattern with maxima and minima. The boundary conditions of the plate have influence on the way the waves reflect at the edges and therefore on the resonance shapes and frequencies[6].

Let us consider a thin rectangular plate with width L_x and height L_y. The thickness is negligible compared to the area dimensions. The origin of the x, y, z-coordinate system is

[4] As an example, the lowest critical frequency f_{cr} of an aluminium plate with thickness 1 mm is about 12 kHz.

[5] In the case of bending waves, the impedance can be seen as either the force or the moment per unit displacement.

[6] This thesis only discusses *simply supported* boundary conditions, for which the local displacement and the curvature, the second spatial derivative of the displacement, are zero.

in the center of the plate, so the boundaries of the plate are at $x = -L_x/2$, $x = L_x/2$, $y = -L_y/2$ and $y = L_y/2$. The *simply supported* boundary condition says that the plate's displacement $\tilde{U}(x, y, t)$ and its spatial second derivative are zero at those edges. Also, the bending wave equation Eq. 2.4 or its space-frequency version has to be fulfilled. If we introduce the concept of *mode shapes* $\phi(x, y)$, which are harmonic displacement solutions to the damping-free wave equation, this wave equation can be written as:

$$\left(D\nabla^4 - \rho h\omega^2\right)\phi(x, y) = 0,$$

and its $(i_x, i_y)^{\text{th}}$ solution for simply supported boundaries will be of the form (Cremer [17]):

$$\phi_{i_\text{x},i_\text{y}}(x, y) = \sin\left(\frac{i_\text{x}\pi}{L_\text{x}}x\right)\ \sin\left(\frac{i_\text{y}\pi}{L_\text{y}}y\right), \quad i_\text{x}, i_\text{y} = 1, 2, \dots\ . \tag{2.26}$$

Solving the natural frequency out of the wave equation for a certain natural mode shape ϕ_{n_x,n_y}, it becomes:

$$f_{i_\text{x},i_\text{y}} = \frac{1}{2\pi}\sqrt{\frac{D}{\rho h}}\left[\left(\frac{i_\text{x}\pi}{L_\text{x}}\right)^2 + \left(\frac{i_\text{y}\pi}{L_\text{y}}\right)^2\right], \quad i_\text{x}, i_\text{y} = 1, 2, \dots\ . \tag{2.27}$$

For convenience, the list of mode shapes can be reordered into increasing natural frequency, and mode shape $\phi_{i_\text{x},i_\text{y}}$ will from now on be called the i^{th} mode shape ϕ_i, and similar for its frequency.

Modal participation

The principle of modal participation is that for the steady state or *harmonic* situation the plate can only vibrate in modes. The previously calculated mode shapes now do not necessarily vibrate in their own resonance frequency, but can be forced to vibrate in the source's frequency. It means that for every load on the model, its displacement $\boldsymbol{u}$ can be written as a summation of all mode shapes (Cremer [17]). The complex factor β_i is a weight factor which determines how dominant the i^{th} mode shape ϕ_i is compared to the other modes and which phase it has relative to the load (see also appendix A):

$$U_\text{z}(x, y) = \sum \beta_i\phi_i(x, y). \tag{2.28}$$

Modal density

The extensive theory of modal response and its acoustic transmission to incident waves is not discussed in this thesis but can be found in Fahy [21] and Cremer [17]. An analytical equation for the transmission loss of a finite plate with random incidence is impossible to give due to the very complex modes fields and the fact that each mode shape has a different radiation pattern.

Usually, a general equation is calculated which deals with *mode densities* instead of considering every individual mode. An approximation of the difference between random noise transmission loss for finite and infinite plates is given by Fahy [21] for frequencies below the critical frequency ($\omega < \omega_{\mathrm{cr}}$):

$$R_{\mathrm{modal}}(\omega) \approx R_0(\omega) - 10\log\left[\ln\left(\frac{\omega\sqrt{S}}{c_0}\right)\right] + 20\log\left[1 - \left(\frac{\omega}{\omega_c}\right)^2\right] \qquad \mathrm{dB}. \tag{2.29}$$

This equation takes into account the presence of modes in such a way that it gives the highest possible transmission loss value, practically meaning the transmission loss between two natural resonances. Around such a resonance frequency the transmission of sound will usually be much higher.

2.3 Measuring the transmission loss

Room and aperture requirements

The international standard (ISO 140 [29]) for measuring the transmission loss of a panel prescribes the use of two *reverberation rooms*, one at each side of the panel. The test specimen is fixed in the aperture of the baffle or wall between the rooms. To ensure reliable measurement results, it should be ensured that the *flanking transmission*, the transmission of sound through any indirect path, is negligible compared to the sound transmitted through the specimen. More specific, the measured transmission loss value should be less than or equal to $R_{\mathrm{max}} - 15$, where R_{max} is the transmission loss between the rooms without an aperture or with a highly insulating construction in the test opening. To this requirement should of course be paid special attention when using heavy, well-isolating test objects.

The opening inside the wall between the laboratory rooms in which the test panel is built is advised to be 10 m^2. A smaller size is possible as long as the wavelength of free bending waves at the lowest frequency f_{min} considered is smaller than half the minimum dimension L_{min} of the specimen:

$$\lambda_{\mathrm{max}} = \sqrt[4]{\frac{D}{\rho h}}\sqrt{\frac{2\pi}{f_{\mathrm{min}}}} < \frac{L_{\mathrm{min}}}{2}. \tag{2.30}$$

The shape of the structure of which the transmission loss is to be measured is not restricted, as long as the previous rules are fulfilled. The frame in which the structure is fixed should have a mass per unit surface that is at least six times bigger than that of the structure to be measured.

Sound pressure level approach

In one of the reverberations rooms one or more loudspeakers excite broadband noise which leads to an approximation of a diffuse sound field. The acoustic energy that is transmitted by the panel that is investigated builds up a diffuse field in the second room. When a stationary situation is reached, microphones[7] record the acoustic pressure over a certain time, their average sound pressure levels L are calculated and the transmission loss is determined using the following equation:

$$R = L_1 - L_2 + 10\log\left(\frac{S}{A}\right) \qquad \text{dB}. \tag{2.31}$$

In this equation the second part of the right hand side contains the area of the test panel S and the sound absorption area in the receiving room A. The absorption area A has to be determined with an absorption measurement (ISO 354 [32]), which is not discussed in this thesis. The average sound pressure level L is determined as follows:

$$L = 10\log\left(\frac{\mathrm{E}\{p^2\}}{p_0^2}\right).$$

Here p_0 is the reference pressure which is equal to 20 μPa and $\mathrm{E}\{p^2\}$ is the mean-square pressure (see also Eq. 2.2).

Intensity approach

Instead of using the sound power in both rooms, a newer international standard describes how the incident intensity can be used to measure the transmission loss correctly (ISO 15186 [30]). Advantage of this measurement technique is that background noise and possible flanking transmissions by walls, ceilings or by the frame are highly suppressed in the result. Another advantage is that, using an intensity probe (see also paragraph 5.2.1), it can be measured which part of the test specimen radiates the most noise.

In the diffuse sound field, plane waves ideally travel in all directions and, considering all plane waves that travel *towards* the plate, the incidence intensity of such a diffuse field at the plate is described by:

$$I_{\text{inc}} = \frac{E\{p^2\}}{4\rho_0 c_0}. \tag{2.32}$$

On the output side, the test specimen's surface needs to be *scanned* to determine the average radiated intensity over the surface. This is done by using an intensity probe fix to a traverse that measures the radiated intensity in a grid of multiple points in front of the surface of interest.

[7] Preferably microphones on rotating arms to obtain a better average of the acoustic pressure in the room

To only measure the intensity that is radiated from the plate (and not towards it), ideally the receiver room should be an *anechoic chamber*, a room which walls, floor and ceiling that do not reflect the incident sound waves. Now both incidence and radiated intensity can be determined and used to calculate the transmission loss using equation 2.1.

2.4 Conclusions

The sound transmission loss is the most important acoustic property of a surface between source and receiver. Standard procedures exist to be able to compare results of different materials, measurements and locations. Analytical formulas can predict the transmission loss, but they depend on assumptions and sometimes neglect aspects that can be important for the result.

To increase the energy loss of a sound wave that travels through a material, we can generally say: "The more mass, the better." This rule is not automatically the best solution for automotive and aeronautical engineers that have to solve noise problems: they have to cope with weight restriction because more mass means more fuel consumption. A possible solution, especially for the difficult to damp low frequency noise, might be the use of *active noise control*. This will be discussed in the next chapter.

Chapter 3

Active Noise Control

3.1 Introduction

Active noise control (ANC) is based upon the *intentional superposition of acoustic waves to result in destructive interference* (Tokhi [53]). By introducing one or more secondary sources the acoustic energy in the medium is redistributed: the noise is reduced in some areas and increased in other regions of the medium. In some cases, the sound field of the secondary source influences the primary source's radiation impedance in such a way that it radiates less acoustic energy.

Computer algorithms play a key role in the practical implementation of active noise control. All processing between detection of the noise signal and the output of a control signal is done digitally. Besides acoustic rules, also (real-time) signal processing needs to be understood well before creating or changing such algorithms.

Although it is generally more convenient describing waves and acoustic propagation in the Fourier domain, a time-domain approach is chosen for the ANC processing in this thesis. All signals and systems are considered to be *causal*. For a signal this means that it is zero when the time is negative and for a system it means that if the input signal is causal, the output signal will be causal too. This causality principle corresponds to all physical time-depending systems (Papoulis [46]).

Before investigating the algorithms of single-channel and multi-channel active noise control, a brief introduction into analogue-digital signal conversion and discrete signal processing is given. An ANC controller processes data in real-time[1], and this adds some extra calculation steps that will be discussed as well. After that, the process of system identification is discussed. This identification is an important step before starting ANC and allows the controller to estimate what the impact of its output signals at the region of interest will be.

[1] *Real-time* does not mean that the time variable is *real*, but that the operations of the process are executed on the current input and before the next input appears.

In this chapter effort is made to write important equations as vector or matrix multiplications. Besides general preference, this will be convenient for the future implementation of algorithms into Matlab [39], the commercial numerical software mainly used in this thesis and specialised in matrix handling.

3.2 Discrete-Time Processing

The introduction of digital computers to record and process signals opened a new book in signal analysis. Instead of a *continuous* signal, as it appears in nature and defined for every time t, its *sampled* version with discrete time n is taken and used for further processing. This sampled, digital or discrete version can be seen as a sequence of measurement points with which the real signal can be approximately reconstructed.

3.2.1 Discrete signals and systems

We consider the time-dependent pressure $p_{\mathrm{A}}(t)$ at a certain point in space called A as being a real and continuous signal (see Fig. 3.1). Its discrete version, $p_{\mathrm{A}}[n\Delta t]$, is a sampled function depending on the integer n and the sampling interval Δt and is formed using Eq. 3.1 (Beranek [8]):

$$p_{\mathrm{A}}[n\Delta t] = \sum_{k=-\infty}^{+\infty} p_{\mathrm{A}}(n\Delta t)\delta[(n-k)\Delta t], \tag{3.1}$$

with $\delta[n\Delta t]$ being the *discrete-time impulse* or *Kronecker delta* function[2]:

$$\delta[n\Delta t] = \begin{cases} 1, & n = 0 \\ 0, & n \neq 0. \end{cases} \tag{3.2}$$

Anti-aliasing

The *sample rate* f_{s}, the number of samples per second in p_{A} and equal to $(\Delta t)^{-1}$, should be chosen with care, taking into account the highest frequency component present in the original signal. The Nyquist frequency f_{Nyquist}, the highest frequency that can be described by a discrete signal with sample rate f_{s}, is defined by $f_{\mathrm{Nyquist}} = \frac{1}{2} f_{\mathrm{s}}$. This means that the sample rate should be at least twice the highest frequency component in signal $p_{\mathrm{A}}(t)$, and the higher f_{s}, the better it approaches this signal (see also Fig. 3.5).

Should signal $p_{\mathrm{A}}(t)$ contain a component with a frequency higher than the Nyquist frequency, *aliasing* appears: the component is mistakenly seen for a component with a frequency

[2] Not to be confused with the *continuous-time impulse* or *Dirac delta* function $\delta(t)$, which is undefined for $t = 0$.

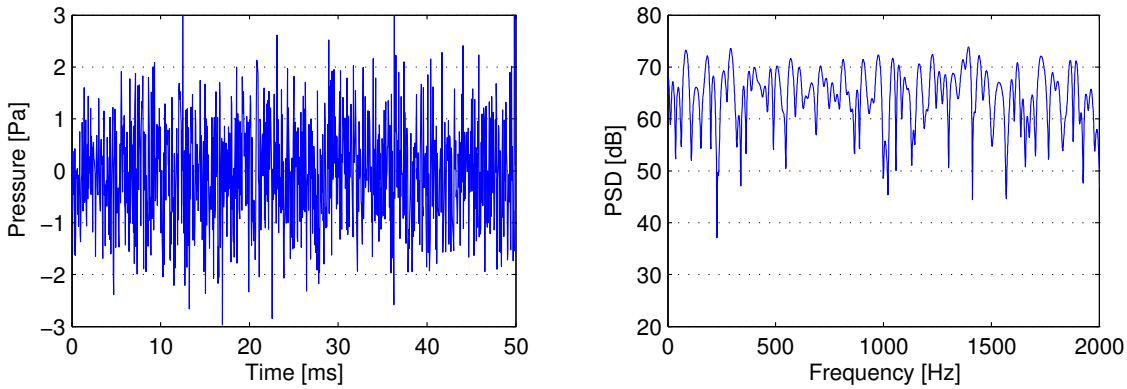

Figure 3.1: Pressure signal $p_{\mathrm{A}}(t)$ in time domain (left) and frequency domain (right) (See Paragraph 3.2.3 for the Power Spectral Density PSD).

lower than the Nyquist frequency. To reduce this unwanted aliasing effect the true signal should always be filtered in such a way that the frequencies above the Nyquist frequency are damped.

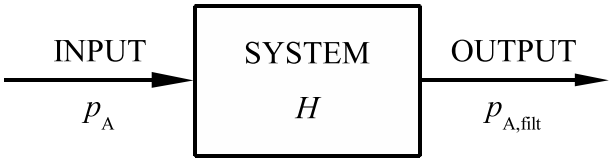

Figure 3.2: A system accepts an input, processes it and produces an output.

We define a system H with *impulse response* $h(t)$, meaning that the system's output is $h(t)$ if its input is the Dirac delta function $\delta(t)$. In our case, the input signal is $p_{\mathrm{A}}(t)$ and the output after applying filter H will be $p_{\mathrm{A,filt}}(t)$ (see Fig. 3.2). The following equation describes this system mathematically by means of convolution:

$$p_{\mathrm{A,filt}}(t) = p_{\mathrm{A}}(t) * h(t) = \int_{-\infty}^{+\infty} p_{\mathrm{A}}(\tau) h(t-\tau) \mathrm{d}\tau. \tag{3.3}$$

As it can be seen, it is a *commutative* process (Papoulis [46]), the two parts in the convolution can be interchanged:

$$p_{\mathrm{A,filt}}(t) = p_{\mathrm{A}}(t) * h(t) = h(t) * p_{\mathrm{A}}(t). \tag{3.4}$$

The time domain and frequency domain characteristics of filter h_{filt} are shown in Fig. 3.3. The time response of this filter shows that applying this filter on the input signal inevitably leads to an extra delay of the signal: its peak is around $t = 1.8$ ms. The frequency response shows that it reduces the high frequency amplitudes in the original signal with approx.

30 dB. For example, a frequency component of 2 kHz will have a $10^{30/10} = 1000$ times lower amplitude after filtering. Components with frequency below the cutoff frequency of $f_{\text{cutoff}} = 1$ kHz remain more or less unchanged.

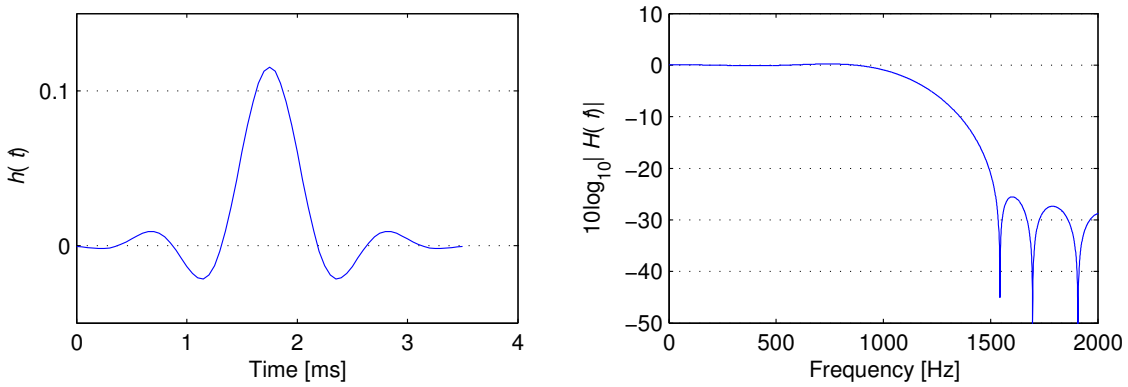

Figure 3.3: Typical lowpass filter (1000 Hz) in time (left) and frequency response (right).

Using Eq. 3.3, the above mentioned low-pass filter h_{filt} is used as an anti-aliasing filter for signal p_{A} in Fig. 3.1. The resulting signal, $p_{\text{A,filt}}$, can be found in Fig. 3.4. As expected, the time signal shows less high and narrow peaks, the peaks, which usually contain high-frequency energy, are damped. The spectrum confirms that components with frequency above the $f_{\text{cutoff}} = 1$ kHz are damped.

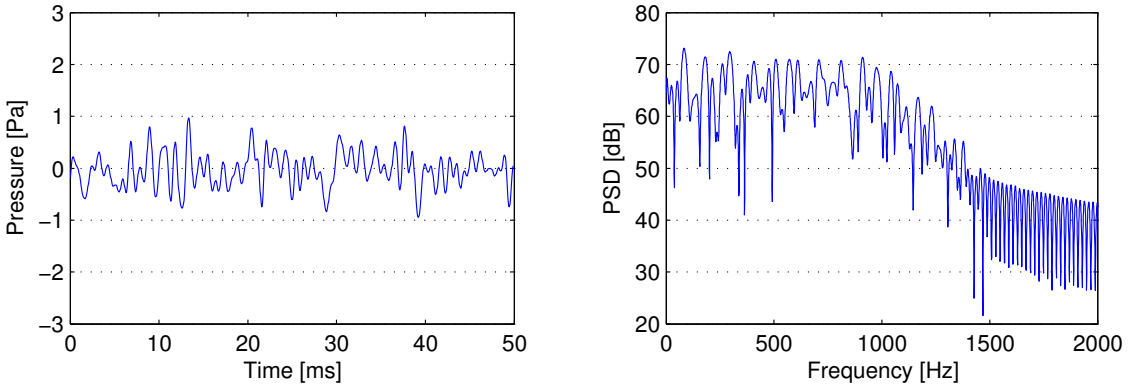

Figure 3.4: Time domain (left) and frequency domain (right) of $p_{\text{A,filt}}(t)$. It is created by applying the filter from Fig. 3.3 on the signal $p_{\text{A}}(t)$ from Fig. 3.1.

Sample rate

As mentioned previously in this paragraph, the sample rate f_{s} of the discrete version of the signal should be chosen with care. Although theoretically we could describe all signals in $p_{\text{A,filt}}(t)$ below 1 kHz using a discrete signal with $f_{\text{s}} = 2$ kHz, there is a high risk of irreversibly losing important information. Therefore, for more precise description

of the original signal, *oversampling* is advisable: a sample rate should be chosen in such a way that its Nyquist frequency is (a few times) bigger than the filter cutoff frequency (see Fig. 3.5). Because a higher sample rate requires faster processing and more digital storage, hardware specifications should determine the upper limit of the sample rate.

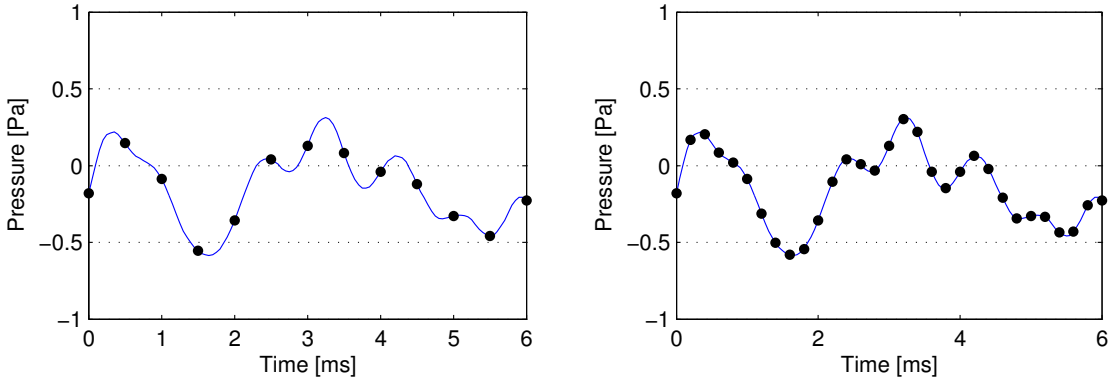

Figure 3.5: Continuous $p_{\mathrm{A,filt}}(t)$ (line) and discrete versions $p_{\mathrm{A,filt}}[n]$ (dots) with $f_{\mathrm{s}} = 2$ kHz (left) and $f_{\mathrm{s}} = 5$ kHz (right). In the left figure we can clearly see that with a too low sample rate the discrete signal has lost important information.

Discrete convolution

Having explained the process of digitizing and convolution for real signals above, we can now come to an equation that describes the convolution process for two discrete signals. Important, because time-domain processing for active noise control inevitably involves discrete convolution. For convenience, from now on we will omit the factor Δt in the expressions for discrete signals:

$$x[n\Delta t] \quad \rightarrow \quad x[n].$$

The convolution of signal $p_{\mathrm{A}}[n]$ with signal $h[n]$ is (Oppenheim [43]):

$$p_{\mathrm{A,filt}}[n] = p_{\mathrm{A}}[n] * h[n] = \sum_{k=-\infty}^{+\infty} p_{\mathrm{A}}[k]h[n-k]. \tag{3.5}$$

3.2.2 Real-time filtering of discrete signals

The discrete convolution process of Eq. 3.5 requires infinite signals, but during real-time signal processing at time n we have, of course, no signal information for time $n+1$ and only have a finite signal history. Computer algorithms generally use such finite signal histories called *buffers* and its length L can be set[3]. After a new time-step, a new sample will be added on top of the buffer at position 1 (time $n\Delta t$), the existing buffer contents

[3]For later convenience the buffer length L will be chosen *even* throughout this thesis.

shifts one position down and the last one in line at position N (time $(n-L+1)\Delta t$) falls out. Fig. 3.6 and Table 3.1 show an example of the signal $p_{\mathrm{A,filt}}[n]$ with its buffer.

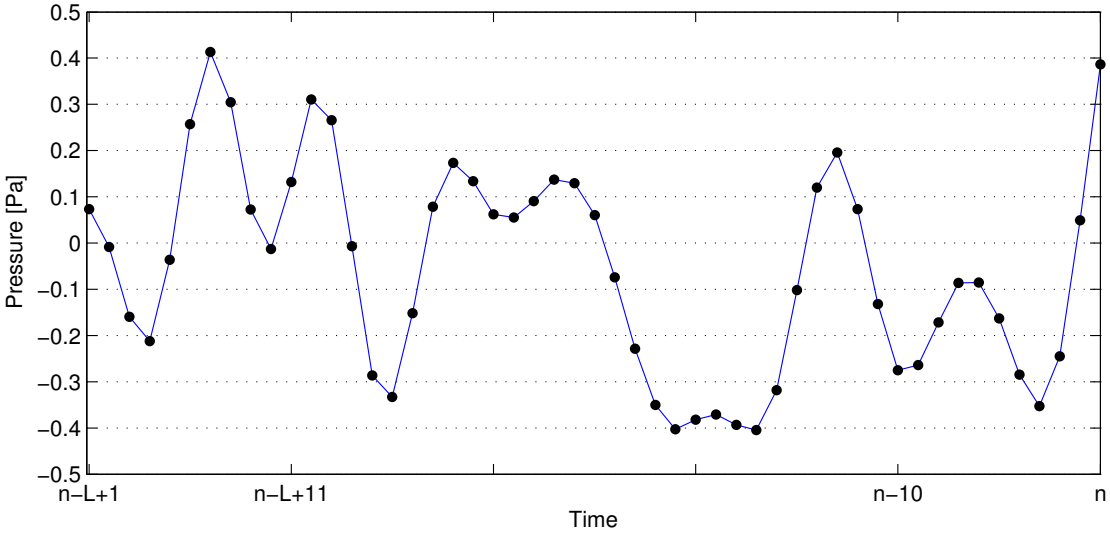

Figure 3.6: Discrete pressure signal $p_{\mathrm{A,filt}}$ from time $(n-N+1)$ to time n. For a clearer view of the evaluation of the signal, the discrete samples are connected with straight lines, not to be mistaken with a continuous signal.

Buffer position	Time/Δt	Pressure [Pa]
1	n	0.387
2	$n-1$	0.049
3	$n-2$	-0.245
⋮	⋮	⋮
$L-1$	$n-L+2$	-0.009
L	$n-L+1$	0.073

Table 3.1: Buffer data of the signal seen in Fig. 3.6 and the position of the values in the buffer.

The filter system H from Fig. 3.2 in the previous paragraph is now assumed to have a discrete filter signal $h[n]$, truncated after I samples. For convenience we write $h[n]$ as a vector $\boldsymbol{h}$ with coefficients h_i. Also to be clear whether speaking about the *sequence* $p_{\mathrm{A}}[n]$ or the n^{th} *sample* $p_{\mathrm{A}}[n]$, from now on we will use the bold vector notation for the sequence $\boldsymbol{p}_{\mathrm{A}}[n]$:

$$\boldsymbol{h} = \begin{bmatrix} h_0 \\ h_1 \\ \vdots \\ h_i \\ \vdots \\ h_{I-2} \\ h_{I-1} \end{bmatrix}, \qquad \boldsymbol{p}_{\mathrm{A}}[n] = \begin{bmatrix} p_{\mathrm{A}}[n] \\ p_{\mathrm{A}}[n-1] \\ \vdots \\ p_{\mathrm{A}}[n-\ell] \\ \vdots \\ p_{\mathrm{A}}[n-L+2] \\ p_{\mathrm{A}}[n-L+1] \end{bmatrix}.$$

Transforming the discrete convolution in Eq. 3.5 into the real-time situation with filter $\boldsymbol{h}$ and signal $\boldsymbol{p}_{\mathrm{A}}[n]$ with a chosen buffer length of L samples ($L \geq I$), the sample of the filtered pressure at time n will be:

$$p_{\mathrm{A,filt}}[n] = \boldsymbol{h}^{\mathrm{T}} \boldsymbol{p}_{\mathrm{A}}[n] = \sum_{i=0}^{I-1} h_i p_{\mathrm{A}}[n-i]. \tag{3.6}$$

Eq. 3.6 supposes that the digital filter can act *instantaneously*: the output $p_{\mathrm{A,filt}}[n]$ is calculated using measurement points up to $p_{\mathrm{A}}[n]$. Because the multiplication needs a finite computation time, this is not realistic. It is thus common to assume a one-sample delay (Elliott [19]). Eq. 3.6 then becomes:

$$p_{\mathrm{A,filt}}[n] = \boldsymbol{h}^{\mathrm{T}} \boldsymbol{p}_{\mathrm{A}}[n] = \sum_{i=1}^{I} h_i p_{\mathrm{A}}[n-i], \tag{3.7}$$

with for the coefficients in $\boldsymbol{h}$:

$$\boldsymbol{h} = \begin{bmatrix} h_1 & h_2 & \cdots & h_i & \cdots & h_{I-1} & h_I \end{bmatrix}^{\mathrm{T}}.$$

3.2.3 Spectral Post-Processing

A powerful tool to investigate the characteristics of a signal is the transform to a frequency dependent representation. A distribution of the signal energy over the frequency span allows us to immediately see which frequency components contribute most and different measurements can be compared easily. This paragraph will explain two tools, the *discrete Fourier transform* and the *Power Spectral Density*, and adapts them to our needs.

The Discrete Fourier Transform

The discrete Fourier transform (DFT) of $\boldsymbol{x}$, a finite discrete-time sequence with length L, is called $\tilde{\boldsymbol{X}}$ and an element $\tilde{X}[k]$ inside it is defined as follows (Oppenheim [43]):

$$\tilde{X}[k] = \frac{1}{\sqrt{L}} \sum_{n=0}^{L-1} x[n] e^{-\mathrm{j}2\pi kn/L}, \quad k = 0, 1, \ldots, L-1 \tag{3.8}$$

where L is the buffer length, $1/\sqrt{L}$ the normalisation factor[4] and k is a discrete frequency. It can be shown that Eq. 3.8 fulfils Parceval's theorem for energy conservation (Papoulis [46]):

$$\sum_{n=0}^{L-1} |x[n]|^2 = \sum_{k=0}^{L-1} \left| \tilde{X}[k] \right|^2. \tag{3.9}$$

[4] In most numerical programs this normalisation factor is chosen unity for transforming from the time-domain into the frequency domain.

The Power Spectral Density

The *Power Spectral Density* (PSD) describes how the power is distributed over the frequencies of a stationary time-series in Watts per Hertz (Oppenheim [44]). For a finite sequence $\boldsymbol{x}[n]$ it can be calculated[5] by using the normalised DFT and the total number of frequency points L:

$$\boldsymbol{\Phi}[k] = \frac{\left|\tilde{\boldsymbol{X}}[k]\right|^2}{L}, \tag{3.10}$$

where the square is taken element-wise.

Using the (normalised) DFT for calculating the PSD we have to consider the following things:

- The DFT's discrete frequency vector $\boldsymbol{k}$ contains real positive and negative frequencies[6].
- To evaluate a (real, causal) signal we only need to look at positive frequencies.
- In the original DFT each frequency k has a negative pair, except $k = 0$ and $k = L/2$.
- For calculating the PSD we only need the absolute values of the DFT.
- The absolute values of the DFT of a real, causal signal are symmetric around 0 Hz (Oppenheim [44]).
- Parceval's theorem has to be fulfilled for the Fourier transforms.

Taking into account these points, we can write for the absolute values of the positive frequencies of the DFT:

$$\left|\tilde{X}[k]\right|^2 = \frac{\alpha_k}{L}\left|\sum_{n=0}^{L-1} x[n]e^{-\mathrm{j}2\pi kn/L}\right|^2, \qquad k = 0, 1, \ldots, \frac{1}{2}L, \tag{3.11}$$

with

$$\alpha_k = \begin{cases} 1, & k = 0 \\ 2, & k = 1, \ldots, \frac{L}{2} - 1 \\ 1, & k = \frac{L}{2}, \end{cases}$$

and so, for positive frequencies only, Eq. 3.10 becomes:

$$\boldsymbol{\Phi}[k] = \frac{\alpha_k}{L^2}\left|\sum_{n=0}^{L-1} x[n]e^{-\mathrm{j}2\pi kn/L}\right|^2, \qquad k = 0, 1, \ldots, \frac{1}{2}L, \tag{3.12}$$

[5] Mathematically this is only an estimation of the PSD; the true PSD can only be taken of an infinite signal with finite energy (Priestley [48]).

[6] The real frequencies $\boldsymbol{f}_\mathrm{k}$ that correspond with the normalised frequency $\boldsymbol{k}$ are $f_\mathrm{k} = k\Delta f$ for $k = 0, 1, \ldots, L/2$ and $f_\mathrm{k} = (k - L)\Delta f$ for $k = L/2 + 1, \ldots, L - 1$. The frequency interval Δf equals f_s/L.

where the number of frequency lines is reduced from L to $\frac{1}{2}L + 1$.

PSD by matrix multiplication

In our case, we use a buffer with pressure[7] elements $p_{\mathrm{A}}[n]$ to $p_{\mathrm{A}}[n - L + 1]$ and frequency vector $\boldsymbol{f}_{\mathrm{k}}$ in Hertz. Rewriting the summation of Eq. 3.12 as a *Vandermonde* matrix (Berkhout [10]), the PSD now becomes:

$$\begin{bmatrix} \Phi_{\mathrm{A}}[f_0] \\ \vdots \\ \Phi_{\mathrm{A}}[f_k] \\ \vdots \\ \Phi_{\mathrm{A}}[f_{L/2}] \end{bmatrix} = \left| \frac{1}{L} \begin{bmatrix} 1.\mathrm{a}^{0\cdot 0} & \cdots & 1.\mathrm{a}^{0\cdot \ell} & \cdots & 1.\mathrm{a}^{0\cdot (L-1)} \\ \vdots & \ddots & & & \\ 2.\mathrm{a}^{k\cdot 0} & & 2.\mathrm{a}^{k\cdot \ell} & & \vdots \\ \vdots & & & \ddots & \\ 1.\mathrm{a}^{\frac{L}{2}\cdot 0} & & \cdots & & 1.\mathrm{a}^{\frac{L}{2}\cdot (L-1)} \end{bmatrix} \begin{bmatrix} p_{\mathrm{A}}[n] \\ \vdots \\ p_{\mathrm{A}}[n-\ell] \\ \vdots \\ p_{\mathrm{A}}[n-L+1] \end{bmatrix} \right|^2 \tag{3.13}$$

where

$$\mathrm{a} = \mathrm{e}^{-\mathrm{j}2\pi/L}$$

and $\boldsymbol{f}_k$ goes from $f_0 = 0$ Hz to $f_{L/2} = f_{\mathrm{Nyquist}}$ with interval $\Delta f = f_{\mathrm{s}}/L$. Note that the matrix is not square but has size $(\frac{1}{2}L + 1)$ x L. Simplified, this equation is written as:

$$\boldsymbol{\Phi}_{\mathrm{A}} = |\mathbf{F}\boldsymbol{p}_{\mathrm{A}}|^2 \tag{3.14}$$

which is our final equation for analysing and plotting the spectrum of time signal segments.

PSD variance reduction using Welch's method

A way to improve the accuracy of the PSD estimation is recording a longer time signal. This time signal has to be divided into M segments, smoothing the edges of these segments using an (energy neutral) windowing function and calculating and averaging their PSDs (Kammeyer [36]):

$$\boldsymbol{\Phi}_{\mathrm{A}} = \frac{1}{M} \sum_m \Phi_{\mathrm{A}}^{(m)} = \frac{1}{M} \sum_m \left| \mathbf{F}\boldsymbol{p}_{\mathrm{A}}^{(m)} \right|^2 . \tag{3.15}$$

3.3 System Identification

Before going into the algorithms of active noise control, we will first take a closer look at the identification of a system. For the ANC's secondary source in a control system to work, we need to know the impulse response $\boldsymbol{g}$ from this secondary source to the receiver sensor (similar to the system of Fig. 3.2). Although it is unknown, it is possible to get a good *estimation* $\hat{\boldsymbol{g}}$ using only the input signal $\boldsymbol{y}[n]$ and output signal $\boldsymbol{d}[n]$ of the system.

[7] In acoustics the PSD is typically calculated using the normalised pressure, meaning scaled to the reference pressure $p_0 = 20$ μPa and plotted it in *decibel*: $10\log(\Phi)$. Although dB is not a unit, for convenience we will write "PSD [dB]" on the plot's vertical axis.

Thereby it is important to realise that its filter coefficients g_i are independent of the type of input signal.

Already mentioned, the impulse response is defined as being the system's output when the input is the Kronecker delta function. If we want to estimate the coefficients in $\boldsymbol{g}$, we only need to insert this function and record the output. Unfortunately, in the physical world including acoustics where the input signal is a pressure, it is very difficult or impossible to create such a delta pulse signal. The alternative is using a broadband noise signal over a certain time length.

For a system to be estimated for a spectrum of, say, 0 to 1 kHz, the input signal has to contain *at least* this bandwidth. In the ideal situation of a delta function input this requirement is fulfilled: it can be shown using Fourier analysis that the delta function contains all frequencies (Papoulis [46]). Alternatives that still have the correct bandwidth could be random noise or a *sweep signal*[8]. The noise signal should be low-pass filtered with our anti-aliasing filter (as in paragraph 3.2) and for a sweep function the upper frequency limit has to be set. In this thesis' impulse response estimation we will use the delta function for the simulations and random noise for the measurements (see also Chapter 5).

In the previous paragraph real-time signal processing is discussed using buffers with finite signal history. Also during active noise control and system identification we want to update the estimation *on-line*, neither wanting to wait a certain number of samples before an estimation can take place nor having to store the entire signal history for processing. Again, we will make use of such buffer techniques and optimise our estimated system *recursively*, meaning that our estimated coefficients are constantly updated using only the estimated coefficients of the previous time-step and the current measurement values (Isermann [33]). Goal is to minimise a *cost function* we call J.

3.3.1 The Least Mean Square (LMS) method

Suppose we have a system with response $\boldsymbol{g}$, input signal $\boldsymbol{y}[n]$ and output signal $\boldsymbol{d}[n]$. The estimation of $\boldsymbol{g}$ is called $\hat{\boldsymbol{g}}$ and the response to $\boldsymbol{y}[n]$ for this estimated system is $\hat{\boldsymbol{d}}[n]$ (obtained by discrete convolution, see Eq. 3.5). Because we do not know the original coefficients of $\boldsymbol{g}$, we can estimate them by comparing the two outputs $\boldsymbol{d}[n]$ and $\hat{\boldsymbol{d}}[n]$. The error signal $\boldsymbol{e}[n]$ is the difference between the two outputs (see Fig. 3.7). Using the real-time convolution of Eq. 3.7, we get for the error at time n:

$$e[n] = d[n] - \hat{d}[n] = d[n] - \hat{\boldsymbol{g}}_n^{\mathrm{T}} \boldsymbol{y}[n], \tag{3.16}$$

where $\hat{\boldsymbol{g}}_n$ is the estimated system response at time n (not to confuse with coefficient $\hat{g}_n$).

[8] The sweep signal is explained in Paragraph 5.2.4.

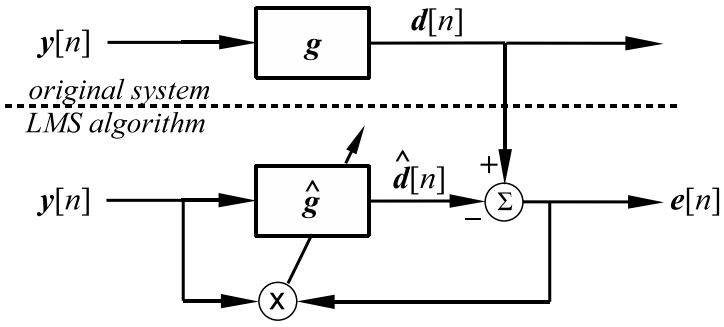

Figure 3.7: The original system with impulse response $\boldsymbol{g}$ and the LMS scheme to estimate it. Input $\boldsymbol{y}[n]$ is used for both systems. The original output $\boldsymbol{d}[n]$ is fed into the LMS algorithm. The difference between $\boldsymbol{d}[n]$ and $\hat{\boldsymbol{d}}[n]$ determines the error size $\hat{\boldsymbol{e}}[n]$ and this influences the coefficients of $\hat{\boldsymbol{g}}$.

Goal is to minimize the error, or more precise, the expectation of the squared error signal, which will be our cost function J:

$$J = E\{e^2[n]\}. \tag{3.17}$$

In case of an improving estimation, J reduces towards zero and our estimation $\hat{\boldsymbol{g}}$ approaches the original system's impulse response[9]. The disadvantage of this cost function is, that, in order to calculate the mean of the error, we need to time-average over a large history of data. For a faster model, therefore, we will not use a signal history but the *instant* error sample $e[n]$ in our cost function instead (Elliott [19]). The new cost function becomes:

$$J = e^2[n]. \tag{3.18}$$

3.3.2 Steepest-descent minimisation

The idea behind the LMS algorithm is that the cost function J, given in Eq. 3.18, is minimised using the *steepest descent* method. After every time-step the coefficients $\hat{\boldsymbol{g}}_i$ are changed by a small amount in the direction of the *negative gradient* of J:

$$\hat{\boldsymbol{g}}_{n+1} = \hat{\boldsymbol{g}}_n - \mu \frac{\partial J_n}{\partial \hat{\boldsymbol{g}}}, \tag{3.19}$$

with μ being a free-to-chose convergence factor that determines the step-size towards the minimum. The gradient $\partial J_n / \partial \hat{\boldsymbol{g}}$, the partial derivative of J to all coefficients $\hat{g}_i$, is at

[9] For two systems with equal *impulse response* it does not automatically imply the *systems* are equal. Because we are only interested in the system's response, reducing the difference between output $\boldsymbol{d}[n]$ and estimated output $\hat{\boldsymbol{d}}[n]$ satisfies us.

time n, using Eq. 3.16 and Eq. 3.18:

$$\frac{\partial J_n}{\partial \hat{\boldsymbol{g}}} = 2e[n]\frac{\partial e[n]}{\partial \hat{\boldsymbol{g}}} = -2e[n]\boldsymbol{y}[n] \tag{3.20}$$

and the updating equation 3.19 becomes:

$$\hat{\boldsymbol{g}}_{n+1} = \hat{\boldsymbol{g}}_n + 2\mu\boldsymbol{y}[n]e[n]. \tag{3.21}$$

3.3.3 Convergence

From the gradient derived in the previous paragraph we see that the step-size depends on the present error $e[n]$ and the convergence factor μ. The error signal dependency means that the step-size reduces if J approaches a minimum, which allows the algorithm to better 'focus' on that minimum. However, if the step-size is too big, it could overshoot the minimum, update the estimated system with large coefficients which results in an even bigger error signal with even bigger step-size: the algorithm becomes unstable. More precise, the estimated coefficients in $\hat{\boldsymbol{g}}$ and therefore output $\hat{\boldsymbol{d}}$ incline to infinity. Without doubt a very unwanted situation, but it can be prevented using the convergence factor μ.

A proper value for μ is difficult to give, usually there has to be a consensus between stability and convergence speed. Elliott [19] estimates the *maximum* value for μ being

$$\mu_{\max} = \frac{1}{\{y^2\}L}, \tag{3.22}$$

where L is both the number of coefficients of $\hat{\boldsymbol{g}}$ and the buffer-length of $\boldsymbol{x}[n]$, and $\{y^2\}$ is the mean-square value of input signal $\boldsymbol{y}[n]$, but states himself that it is wise to choose a more conservative value. The factor $\mu_{\max}$ is, however, a good scaling value and we will introduce a free to choose factor μ_0 for which the convergence factor μ will be:

$$\mu = \mu_0\mu_{\max} = \frac{\mu_0}{\{y^2\}L} \approx \frac{\mu_0}{\boldsymbol{y}^{\mathrm{T}}[n]\boldsymbol{y}[n]}, \qquad \mu_0 \leq 1, \tag{3.23}$$

where the mean-square of the input signal times the buffer length, $\{y^2\}L$, is replaced by the inner product of the input signal buffer, $\boldsymbol{y}^{\mathrm{T}}[n]\boldsymbol{y}[n]$.

3.4 Active Noise Control

The most effective way to cancel the noise field coming from a primary source is by adding a secondary source at the exact same location, with the exact same amplitude and directivity pattern and in exact opposite phase; the result would be silence.

Unfortunately, dealing with the real world, we automatically have a finite distance between the two sources and usually do not know the exact source signal and characteristics. But

even then it is possible to create such a signal for the secondary source that, by destructive interference, the noise level in a certain area can be reduced. The closer the two sources are together, the larger the area of controlled low noise could be, but a short distance between the sources implies little time for a controller to react: unpredictable changes in the primary noise field can not be processed in time and the reduction results are not good enough.

Having explained the basics of LMS system identification in the previous paragraph, it is only a small step to adapt this algorithm to the situation where the goal is reducing the sound power at the error sensor location. Again, a time-domain causal filter is estimated and adapted in such a way that a cost function is minimised. This straightforward and robust ANC technique is called *adaptive Finite Impulse Response (FIR)* (Elliott [19]).

In applications with high acoustic resonances it might occur that the necessary ANC filter lengths exceed the maximum limits determined by hardware and/or software. In such a case *infinite impulse response (IIR)* filters could be used instead. An IIR filter is different from a FIR filter in the way that the output is not simply the convolution of input and filter coefficients, but also the output signal history plays a role (Matlab [39]). Advantage generally is that less filter coefficients are needed to describe the impulse responses and the adaptive filter, disadvantage can be a less stable control system.

In this dissertation the system or *plant* is a plate in air, the sensors are microphones and the actuators are piezo-electric transducers. This chapter will discuss the ANC algorithms in a general way, leaving open the possibility to apply it on other situations. A control algorithm in the frequency domain can be wise if working mainly with tonal noise [19]. Because this technique would limit the future implementation of ANC in time-dependent simulations, it will not be discussed in this thesis.

3.4.1 Feedforward control

For an adaptive FIR controller we can distinct two set-ups: *feedback* and *feedforward control*. In the feedback situation only error sensors are used to adapt. This is sometimes convenient in situations where it is not possible or attractive to have a reference signal close to the source. The disadvantage is that this set-up only works well for situations with noise of high predictability, like tonal noise.

The feedforward situation, used in this thesis, not only uses error sensors, but one or more reference sensors as well. Using them the system can better predict what the signal at the error region will be, and anticipate on it. With a sensor close to the source important information of the noise that enters the system is detected

The error sensors are used to check how effective the controller is and whether adaption is needed to improve the result. Conform the previous paragraph, these error sensors are

used for the cost function that needs to be minimised. A control algorithm that uses reference and error in such a way is the *Filtered-Reference LMS Algorithm*. It is the most used ANC algorithm, and will be explained below.

The Filtered-Reference LMS Algorithm

Being a feedforward control system, the Filtered-Reference LMS algorithm, or in short the *FxLMS* algorithm, processes a reference signal $\boldsymbol{x}[n]$ in such a way that the output $\boldsymbol{y}[n]$ at the secondary source will cancel the original noise signal $\boldsymbol{d}[n]$ at the error position (see Fig. 3.8). The differences with the LMS system identification diagram seen previously are that a filter $\boldsymbol{g}$ is added, representing the impulse response from secondary source output to the error sensor[10] and that the output of the algorithm is added to $\hat{\boldsymbol{d}}[n]$ instead of subtracted.

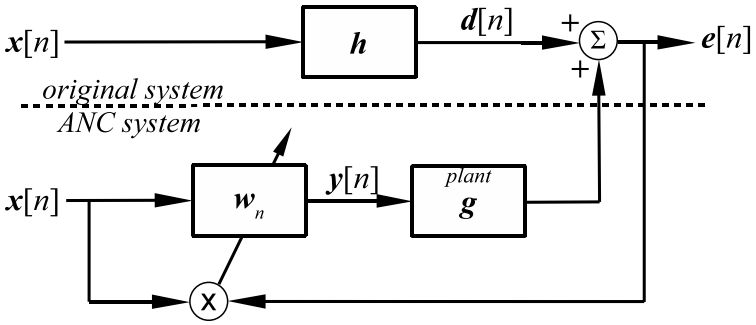

Figure 3.8: The original system with impulse response $\boldsymbol{h}$ and the feedforward ANC scheme to cancel its output $\boldsymbol{d}[n]$. Like in Fig. 3.7, the input or *reference signal* $\boldsymbol{x}[n]$ of the original system is used together with the error signal $\boldsymbol{e}[n]$ to adapt filter $\boldsymbol{w}_n$. The output of the filter $\boldsymbol{w}_n$ is the secondary source signal $\boldsymbol{y}[n]$. It travels through the *plant* with impulse response $\boldsymbol{g}$, interferes with signal $\boldsymbol{d}[n]$ and the resulting signal is error $\boldsymbol{e}[n]$.

The controller's output signal $\boldsymbol{y}[n]$ is the convolution of reference signal $\boldsymbol{x}[n]$ with the vector $\boldsymbol{w}$ and this vector is updated every time-step. At time n this means that the output is

$$y[n] = \boldsymbol{w}_n^{\mathrm{T}} \boldsymbol{x}[n], \tag{3.24}$$

with for $\boldsymbol{w}_n$:

$$\boldsymbol{w}_n = [w_1 \quad w_2 \quad \cdots \quad w_i \quad \cdots \quad w_{I-1} \quad w_I]^{\mathrm{T}},$$

and the error signal $\boldsymbol{e}[n]$ is at time n:

$$e[n] = d[n] + \boldsymbol{g}^{\mathrm{T}} \boldsymbol{y}[n]. \tag{3.25}$$

Before starting active noise control, the plant's response $\boldsymbol{g}$ is estimated in a similar way

[10] Note that this impulse response not only includes the travelling of signal $\boldsymbol{y}[n]$ through e.g. air, but also all amplitude and phase changes by filters, amplifiers, transducers characteristics etc. between the output filter $\boldsymbol{w}$ and the input of the error signal $\boldsymbol{e}[n]$.

as the system identification of the previous paragraph. Preferably, this is done with the primary source turned off ($\boldsymbol{x}[n] = 0$). A broadband signal is sent to to the secondary source $\boldsymbol{y}[n]$ and the error signal is used as the plant response. The estimated plant will be called $\hat{\boldsymbol{g}}$.

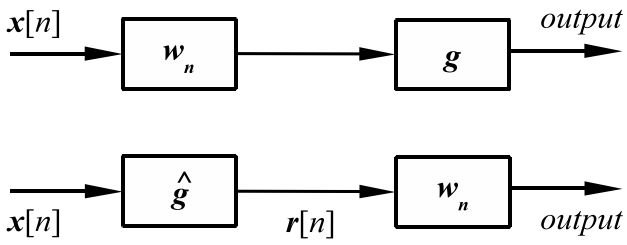

Figure 3.9: For the case that filter $\boldsymbol{w}_n$ is constant in time and $\hat{\boldsymbol{g}} = \boldsymbol{g}$, we can say that the two filters are *commutative*, which means that the impulse response of the system does not depend on the order in which the filters appear.

By assuming that during adaptation the coefficients in $\boldsymbol{w}$ will only slowly change in time relative to the buffer-length L, we can make use of the *commutative* properties of convolution (see also Fig. 3.9 and Eq. 3.4):

$$(\boldsymbol{x} * \boldsymbol{w}_n) * \boldsymbol{g} \approx (\boldsymbol{x} * \boldsymbol{g}) * \boldsymbol{w}_n \quad \text{for} \quad \boldsymbol{w}_n \approx \boldsymbol{w}_{n-1}, \tag{3.26}$$

and now we can replace Eq. 3.25 with:

$$e[n] = d[n] + \boldsymbol{w}_n^{\mathrm{T}} \boldsymbol{r}[n], \tag{3.27}$$

with $\boldsymbol{r}[n]$ being the *filtered-reference signal* (see Fig. 3.9 and 3.10):

$$\boldsymbol{r}[n] = \boldsymbol{x}[n] * \hat{\boldsymbol{g}}. \tag{3.28}$$

Parallel to the system identification equations 3.17 to 3.21, the updating step of our adaptive filter $\boldsymbol{w}_n$ is described as follows:

$$\boldsymbol{w}_{n+1} = \boldsymbol{w}_n - \mu \frac{\partial J_n}{\partial \boldsymbol{w}}, \tag{3.29}$$

with for the (instant) cost-function again:

$$J_n = e^2[n]. \tag{3.30}$$

Using Eq. 3.27, we can now say for the gradient:

$$\frac{\partial J_n}{\partial \boldsymbol{w}} = 2e[n] \frac{\partial e[n]}{\partial \boldsymbol{w}} = 2e[n]\boldsymbol{r}[n] \tag{3.31}$$

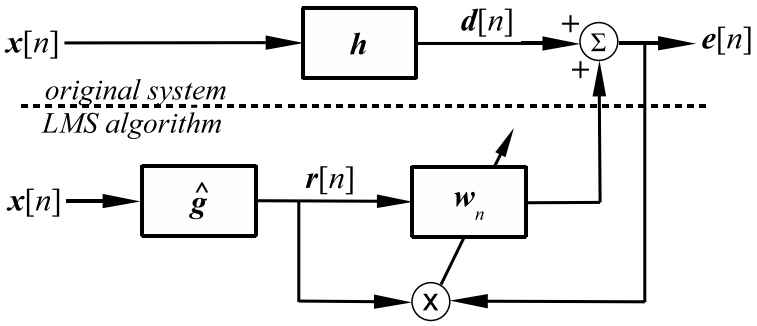

Figure 3.10: Same situation as Fig. 3.8 but the general feedforward system now is a filtered-reference algorithm: the coefficients in controller filter $\boldsymbol{w}$ are determined by the error $\boldsymbol{e}[n]$ and $\boldsymbol{r}[n]$, where the last one is called the *filtered reference* signal, obtained by convolution of the input signal $\boldsymbol{x}[n]$ and the estimation for the plant $\hat{\boldsymbol{g}}$.

and Eq. 3.29 becomes:

$$\boldsymbol{w}_{n+1} = \boldsymbol{w}_n - 2\mu \boldsymbol{r}[n]e[n]. \tag{3.32}$$

Herein the convergence factor μ is chosen as (Cabell [15]):

$$\mu = \frac{\mu_0}{\boldsymbol{r}[n]^{\mathrm{T}}\boldsymbol{r}[n]}, \qquad 0 < \mu_0 \leq 1. \tag{3.33}$$

Leaky LMS

The goal of minimising the cost function or, in our case, reducing the noise level at the error position should not be achieved by all means. It would not be very efficient to let the secondary source use a large amount of energy and in return only receiving a small noise reduction.

Instead, a better objective could be reducing the error signal and the same time keeping the filter coefficients w_n small. This so called *Leaky LMS algorithm* has a new cost function which contains the inner product of $\boldsymbol{w}_n$ with itself. At time n it is:

$$J_n = e^2[n] + \beta \boldsymbol{w}_n^{\mathrm{T}} \boldsymbol{w}_n, \tag{3.34}$$

with β being a positive coefficient-weighting factor (Elliott [19]).

The gradient and the updating equation now become:

$$\frac{\partial J_n}{\partial \boldsymbol{w}} = 2e[n]\boldsymbol{r}[n] + 2\beta \boldsymbol{w}_n, \tag{3.35}$$

$$\boldsymbol{w}_{n+1} = \boldsymbol{w}_n - \mu \frac{\partial J_n}{\partial \boldsymbol{w}} = (1 - 2\mu\beta)\boldsymbol{w}_n - 2\mu \boldsymbol{r}[n]e[n]. \tag{3.36}$$

Now the output effort can be controlled: the bigger β is, the more the cost function is focusing on keeping the controller coefficients and so its own output small.

3.4.2 Multichannel control (MIMO)

The described control algorithm should of course not be limited to single channel operation. The feedforward scheme that will be discussed in this paragraph is able to deal with more than one reference, error and output channels and this multichannel control is called *MIMO* (Multiple Input Multiple Output).

When not dealing with one-dimensional acoustic problems like ventilation ducts but with three-dimensional cases like engine noise in the free-field, it is wise to use more than one secondary source actuator and sensor. When the goal is obtaining a three-dimensional region of silence, error sensors should be distributed over this region to prevent the controller from focusing its efforts only on one point in space.

System identification

For a MIMO feedforward controller system with J reference sensors, K secondary output transducers and M error sensors (see Fig. 3.11), there will be $J \times K$ control filters with length I and $K \times M$ estimated plant responses with length L (from each secondary source to every error sensor).

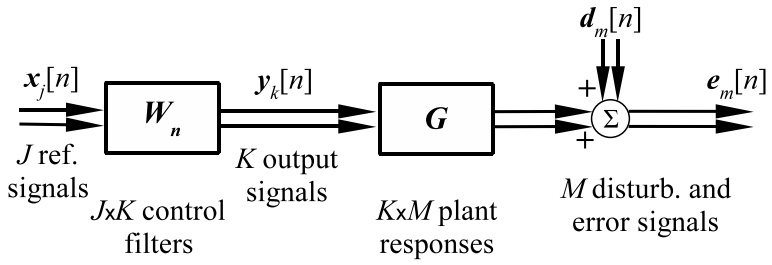

Figure 3.11: General feedforward scheme for a MIMO controller with dimension $J \times K \times M$: J reference channels, K controller output channels and M error channels.

For error sensor m at time n during system identification we can say, similar to Eq.3.16:

$$e_m[n] = d_m[n] - \hat{d}_m[n] = d_m[n] - \sum_{k=1}^{K} \hat{\boldsymbol{g}}_{km}^{\mathrm{T}} \boldsymbol{y}_k[n], \tag{3.37}$$

where $\hat{\boldsymbol{g}}_{km}$ is the estimated impulse response from secondary source k to error sensor m and has length L. We can not estimate all $K \times M$ plant responses simultaneously, but have to do it for each secondary source separately. The update equation 3.21 for an estimated

impulse response from source k to error sensor m now becomes:

$$\hat{\boldsymbol{g}}_{km,n+1} = \hat{\boldsymbol{g}}_{km,n} + 2\mu \boldsymbol{y}_k[n] e_m[n]. \tag{3.38}$$

Using matrix calculation we can execute Eq. 3.38 in one time instead of calculating it M times for every error sensor. The matrix version would look as follows:

$$\hat{\boldsymbol{G}}_{k,n+1} = \hat{\boldsymbol{G}}_{k,n} + 2\mu \boldsymbol{y}_k[n] \boldsymbol{E}[n] \tag{3.39}$$

where $\boldsymbol{E}[n]$ is a row vector with all latest error samples:

$$\boldsymbol{E}[n] = \begin{bmatrix} e_1[n] & \dots & e_m[n] & \dots & e_M[n] \end{bmatrix} \tag{3.40}$$

and consequently $\hat{\boldsymbol{G}}_k$, the set of estimated impulse responses from secondary source k to all error sensors, will be as follows:

$$\hat{\boldsymbol{G}}_k = \begin{bmatrix} \hat{\boldsymbol{g}}_{k1}^{\mathrm{T}} \\ \vdots \\ \hat{\boldsymbol{g}}_{km}^{\mathrm{T}} \\ \vdots \\ \hat{\boldsymbol{g}}_{kM}^{\mathrm{T}} \end{bmatrix} = \begin{bmatrix} \hat{g}_{k1,1} & \hat{g}_{k1,2} & \cdots & \hat{g}_{k1,L} \\ \vdots & \vdots & & \vdots \\ \hat{g}_{km,1} & \hat{g}_{km,2} & \cdots & \hat{g}_{1m,L} \\ \vdots & \vdots & & \vdots \\ \hat{g}_{kM,1} & \hat{g}_{kM,2} & \cdots & \hat{g}_{1M,L} \end{bmatrix}.$$

For convenience, a single value for the convergence factor μ is chosen, consisting out of μ_0 and a scaling factor. Similar to the single channel case (see Eq. 3.23), the maximum of μ is set by the scaling factor, which makes sure the convergence factor will not get too high. We will introduce the maximum of all k inner products $\boldsymbol{y}_k[n]$ in the equation for μ to set the upper limit:

$$\mu = \frac{\mu_0}{\max_k(\boldsymbol{y}_k^{\mathrm{T}} \boldsymbol{y}_k)}, \quad 0 < \mu_0 \leq 1. \tag{3.41}$$

Filtered-reference control

Changing from system identification to the active noise control situation, we now have one or more external unknown noise sources. These sources are responsible for a signal $\boldsymbol{d}_m[n]$ on error sensor m if the secondary ANC sources are off. We can say that the actual signal on this error sensor during active noise control consists of $\boldsymbol{d}_m[n]$ plus the sum of all outputs $\boldsymbol{y}_k[n]$ convolved with the appropriate plant responses $\boldsymbol{g}_{km}$:

$$\boldsymbol{e}_m[n] = \boldsymbol{d}_m[n] + \sum_{k=1}^{K} \boldsymbol{g}_{km} * \boldsymbol{y}_k[n]. \tag{3.42}$$

Using vector multiplication, we can write for error signal $\boldsymbol{e}_m$ at time n:

$$e_m[n] = d_m[n] + \sum_{k=1}^{K} \boldsymbol{g}_{km}^{\mathrm{T}} \boldsymbol{y}_k[n]. \tag{3.43}$$

The output signal at secondary source k can be written as the convolution of all reference signals $\boldsymbol{x}_j[n]$ with the appropriate control filters $\boldsymbol{w}_{jk}$. At time n it is:

$$y_k[n] = \sum_{j=1}^{J} \boldsymbol{w}_{jk,n}^{\mathrm{T}} \boldsymbol{x}_k[n]. \tag{3.44}$$

Having J reference signals and $K \times M$ estimated impulse responses, we come to $J \times K \times M$ filtered-reference signals. At time n they are:

$$r_{jkm}[n] = \hat{\boldsymbol{g}}_{km}^{\mathrm{T}} \boldsymbol{x}_j[n]. \tag{3.45}$$

Similar to Eq. 3.27, we can express the error sample in Eq. 3.43 in terms of the filtered-reference signal:

$$e_m[n] = d_m[n] + \sum_{j=1}^{J} \sum_{k=1}^{K} \boldsymbol{w}_{jk,n}^{\mathrm{T}} \boldsymbol{r}_{jkm}[n], \tag{3.46}$$

and similar to Eq. 3.34, the cost function J_n at time n for a MIMO system with leakage now becomes:

$$J_n = \sum_{m=1}^{M} e_m^2[n] + \beta \sum_{j=1}^{J} \sum_{k=1}^{K} \boldsymbol{w}_{jk,n}^{\mathrm{T}} \boldsymbol{w}_{jk,n}, \qquad \beta \geq 0. \tag{3.47}$$

Combining Eq. 3.46 and Eq. 3.47 we obtain JK gradients for the cost function:

$$\frac{\partial J_n}{\partial \boldsymbol{w}_{jk}} = 2 \sum_{m=1}^{M} e_m[n] \boldsymbol{r}_{jkm}[n] + 2\beta \boldsymbol{w}_{jk,n} \tag{3.48}$$

and the update equation for $\boldsymbol{w}_{jk,n}$ will be:

$$\boldsymbol{w}_{jk,n+1} = \boldsymbol{w}_{jk,n} - \mu \frac{\partial J_n}{\partial \boldsymbol{w}_{jk}} = (1 - 2\mu\beta) \boldsymbol{w}_{jk,n} - 2\mu \sum_{m=1}^{M} \boldsymbol{r}_{jkm}[n] e_m[n]. \tag{3.49}$$

When all filtered-reference buffers $\boldsymbol{r}_{jkm}[n]$ are updated using Eq. 3.45 and all new vectors $\boldsymbol{w}_{jk,n+1}$ are determined with the last equation above, we can calculate the new output values $y_k[n+1]$ for all k secondary sources using Eq. 3.44.

Again, a single value for the convergence factor μ and also for the leak factor β are chosen. As in Eq. 3.41, to be on the safe side we choose the maximum value of all inner products, this time the inner product of the filtered-reference signal $\boldsymbol{r}_{klm}[n]$ (see also Eq. 3.33):

$$\mu = \frac{\mu_0}{\max_{jkm}(\boldsymbol{r}_{jkm}^{\mathrm{T}}\boldsymbol{r}_{jkm})}, \quad 0 < \mu_0 \leq 1. \tag{3.50}$$

In case of a system with relatively constant noise level, this convergence factor μ can be determined before turning on active noise control, saving calculating time during operation.

Matrix multiplications for MIMO control

The signals in the previous paragraph all are written out separately for every reference, error and secondary source channel. It would be convenient to write the previous sets of MIMO vector operations in terms of single matrix multiplications. Unfortunately, this conversion can only be applied for a few of the MIMO step.

We will start by calculating the new filtered-reference values for time n by using a matrix buffer $\boldsymbol{X}[n]$ with all reference signals and a matrix $\hat{\boldsymbol{G}}$ with all estimated impulse responses:

$$\boldsymbol{R}_n = \hat{\boldsymbol{G}}\boldsymbol{X}[n], \tag{3.51}$$

where reference signal buffer $\boldsymbol{X}[n]$ has the following column structure:

$$\boldsymbol{X}[n] = \begin{bmatrix} \boldsymbol{x}_1[n] & \cdots & \boldsymbol{x}_J[n] \end{bmatrix} = \begin{bmatrix} x_1[n] & \cdots & x_J[n] \\ x_1[n-1] & \cdots & x_J[n-1] \\ \vdots & & \vdots \\ x_1[n-\ell] & \cdots & x_J[n-\ell] \\ \vdots & & \vdots \\ x_1[n-L+1] & \cdots & x_J[n-L+1] \end{bmatrix}$$

and $\hat{\boldsymbol{G}}$ is formed as follows, with the responses in rows:

$$\hat{\boldsymbol{G}} = \begin{bmatrix} \hat{\boldsymbol{g}}_{11}^{\mathrm{T}} \\ \vdots \\ \hat{\boldsymbol{g}}_{1M}^{\mathrm{T}} \\ \hat{\boldsymbol{g}}_{21}^{\mathrm{T}} \\ \vdots \\ \hat{\boldsymbol{g}}_{KM}^{\mathrm{T}} \end{bmatrix} = \begin{bmatrix} \hat{g}_{11,1} & \hat{g}_{11,2} & \cdots & \hat{g}_{11,L} \\ \vdots & \vdots & & \vdots \\ \hat{g}_{1M,1} & \hat{g}_{1M,2} & \cdots & \hat{g}_{1M,L} \\ \hat{g}_{21,1} & \hat{g}_{21,2} & \cdots & \hat{g}_{21,L} \\ \vdots & \vdots & & \vdots \\ \hat{g}_{KM,1} & \hat{g}_{KM,2} & \cdots & \hat{g}_{KM,L} \end{bmatrix}.$$

After multiplication ,this leads to an $\boldsymbol{R}_n$ that contains all filtered-reference samples for the new time-step n and looks like:

$$\boldsymbol{R}_n = \begin{bmatrix} r_{111}[n] & \cdots & r_{j11}[n] & \cdots & r_{J11}[n] \\ \vdots & & \vdots & & \vdots \\ r_{1K1}[n] & \cdots & r_{jK1}[n] & \cdots & r_{JK1}[n] \\ r_{112}[n] & \cdots & r_{j12}[n] & \cdots & r_{J12}[n] \\ \vdots & & \vdots & & \vdots \\ r_{1KM}[n] & \cdots & r_{jKM}[n] & \cdots & r_{JKM}[n] \end{bmatrix}.$$

To rewrite the update equation 3.49 in matrix form, we need to have the dimension of $\boldsymbol{R}[n]$ such that, multiplying with a vector of M error values e_m, the result has the dimension of a matrix $\boldsymbol{W}$, a set of $J \times K$ vectors $\boldsymbol{w}_{jk}$ with length I. To make it even more complex, this resulting matrix $\boldsymbol{W}_n$ is needed in the matrix multiplication version of equation 3.44, where it needs to be multiplied with our matrix buffer $\boldsymbol{X}[n]$ which has J columns to receive K elements $y_k[n]$.

It is obvious that these multiplications can not be fulfilled using one and the same structure for $\boldsymbol{X}[n]$, $\boldsymbol{W}_n$ and $\boldsymbol{R}[n]$. Using different versions of those matrices for the two equations mentioned by reordering does not bring a calculation advantage. Therefore, instead of matrix multiplication, $J \times K \times M$ different vectors $\boldsymbol{r}_{jkm}$ are used and updated with the appropriate values from $\boldsymbol{R}_n$ given above. Of course, all those filtered-reference vectors can be stored in a single buffer matrix $\boldsymbol{R}$ (see Eq. 3.52) to make the updating procedure more easy. The vectors are used together with the M error values e_m to update $J \times K$ adaptive filter vectors $\boldsymbol{w}_{jk}$ following Eq. 3.49. Finally, with those vectors we will calculate K output values y_k by using Eq. 3.44, which are the output samples that will be sent to the actuators.

$$\boldsymbol{R}[n] = \Big[\boldsymbol{r}_{111}[n] \cdots \boldsymbol{r}_{JKM}[n]\Big] = \begin{bmatrix} r_{111}[n] & \cdots & r_{JKM}[n] \\ r_{111}[n-1] & \cdots & r_{JKM}[n-1] \\ \vdots & & \vdots \\ r_{111}[n-i] & \cdots & r_{JKM}[n-i] \\ \vdots & & \vdots \\ r_{111}[n-I+1] & \cdots & r_{JKM}[n-I+1] \end{bmatrix} \tag{3.52}$$

3.4.3 Noise signal dependency

In the process of active noise control three different aspects can be distinguished that cause time delay and have a negative effect on the performance.

- The analogue signals going into and coming out of the controller need to be processed[11] which leads to time delays.

[11] The analogue microphone signal will be filtered with an anti-aliasing filter and then sampled (A/D

- The controller algorithm itself needs a minimum of 1 sample delay for processing.
- The propagating time of a signal from secondary source to error sensor should be taken into account (see Fig. 3.12).

If the sum of all these delays is bigger than the time the noise needs for travelling from reference sensor to error sensor, the controller can not generate an anti-signal in time to cancel the original signal.

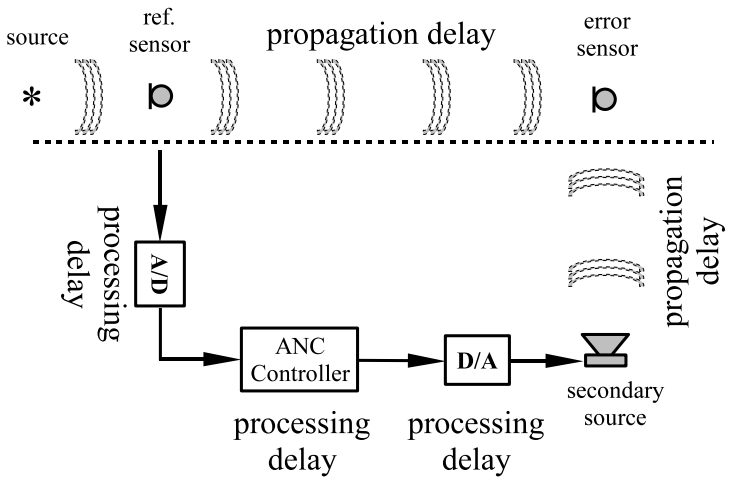

Figure 3.12: General scheme of a system with active noise control. Ideally, the sum of delays in the controller path is smaller than the propagation delay of the noise from the reference to the error sensor. The dashed line again represents the separation between the original system and the ANC system.

However, the *predictability* of a signal plays an important role here. For a pure sine signal we exactly know its future behaviour and an ANC system can perform well. The more unpredictable or *stochastic* a source signal, the less can be said about the signals future when only the current status and the signal history is known. For a pure stochastic noise signal its future is completely unknown.

Implementing an active noise control system, a few, more or less common rules should be taken into account that can improve ANC performance:

- The more tonal the noise, the better the performance.
- The shorter the distance from secondary source to error sensor, the better the performance.
- The bigger the distance between reference sensor and secondary sources, the better the performance.

conversion). After ANC algorithm processing, the discrete output signal will be filtered again to send out an analogue signal to the amplifier or loudspeaker (D/A conversion) (see also paragraph 3.2.1).

- The closer the reference sensor to the source and the better the reference signal approaches the true source signal, the better the performance.
- The flatter the response spectrum of the secondary source to the error sensors, the better the overall performance.

3.5 Conclusions

To understand, create or change computer algorithms for active noise control applications a great deal of (real-time) signal processing has to be applied. The ANC results partly depend on the controller's calculation speed, which can be improved by efficient calculation and data handling. But a good working controller is not enough. Also the position of the sensors and actuators, decisions made by the user, play a role.

If the distance between the active structure and the error sensors is relatively large, the performance can reduce a lot due to the delay between actuator and sensor (Berkhoff [9]). On the other hand, using for example accelerometers mounted on the plate as error sensors may lead to disappointing reduction results in the far-field (Fuller [24]). Chapter 5 will discuss the sensor positions chosen for our purpose.

This chapter discussed an important ANC algorithm called the *filtered-reference* algorithm and it can be written for single and multiple channel (MIMO) cases. In this thesis we will use the MIMO version for all following situation. The single channel algorithm will be seen as special case of the MIMO algorithm where all the matrices have only one row or column.

Next chapter will discuss another major field in engineering called *Finite Element Simulation* (FEM). As with ANC, also this numerical application can be used in frequency or in time domain. Choosing time domain simulations we can apply the knowledge of the present chapter in acoustic finite element investigations. If succeeding, the behaviour of ANC situations can be predicted and improved accordingly in applications that are simulated and not yet constructed.

Chapter 4

Finite Element Simulation

4.1 Introduction

Acoustical research these days often includes investigations on active noise control. To predict what the noise reduction would be in case of applying ANC, an analytical or finite element model of the set-up is made and the maximum possible reduction is calculated. The question whether this optimum can be found and whether it will be reached by the adaptive controller remains unanswered until real experiments are executed. As an example, in [26] Henrioulle made an analytical model of plate and actuator and calculated the maximum possible transmission loss. The experimental side of these investigations, presented by Dehandschutter in [18], show that those results by far were not reached.

Another thing that should be noted from [26] is that the analytical model was only possible because the actuator was a PVDF piezoelectric layer over the complete plate. A model for which the analytical equation of motion is known in literature and verified. Should the plate have different actuators or a non-rectangular flat shape, this equation would be extremely difficult if not impossible to derive. For that purpose the finite element method would be ideal, which divides a structure into many small parts called elements for which the behaviour is known.

This chapter discusses the finite element method used to simulate our thin plate. As element type a so called *Shell*-element is used, which is thin and has linear shape functions, corresponding to Kirchhoff's theory for plates (see also Ansys [4] and Hechenblaikner [25]). Having obtained the model matrices, the transient simulations are executed using the Newmark-β method (MacNeal [38]). The equations will be adapted so they can be of better use for the radiation calculation method proposed, which is a discrete and time-dependent version of the well-known Huygens-Rayleigh integral for acoustic radiation.

4.2 Finite Element Theory

4.2.1 The equation of motion

Let us consider a spring-mass system with spring constant k, damping b and mass m (see Fig. 4.1). The sum of time-dependent forces $f_{\text{tot}}(t)$ acting on the mass is

$$f_{\text{tot}}(t) = f_{\text{spring}}(t) + f_{\text{damp}}(t) + f_{\text{ext}}(t) = -ku(t) - b\dot{u}(t) + f_{\text{ext}}(t), \tag{4.1}$$

where $f_{\text{spring}}(t)$ is the spring's restoring force depending on the displacement from the static equilibrium $u(t)$. The damping force f_{damp} depends on the velocity $\dot{u}$ and f_{ext} is the sum of external forces working upon the system. Omitting the time dependent notation (t) and combining Eq. 4.1 with Newton's second law,

$$f_{\text{tot}} = m\ddot{u}, \tag{4.2}$$

we get the well known equation of motion, which is a second order differential equation:

$$m\ddot{u} + b\dot{u} + ku = f_{\text{ext}}. \tag{4.3}$$

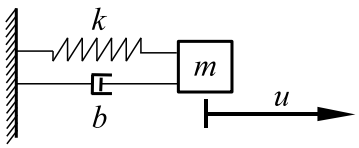

Figure 4.1: One-dimensional spring-mass-damper system. The damping constant is called b, spring constant is k and the displacement of the mass m is u.

Modal analysis

To determine the resonance frequency f_0 of the previously mentioned system, it will be analysed without damping, meaning that parameter b is zero and the vibration describes an (undamped) sine-like displacement:

$$u(t) = u_0 \sin(\omega_0 t + \psi), \tag{4.4}$$

where u_0 is the amplitude of the vibration, ω is the angular frequency $(= 2\pi f)$ and ψ is the phase at time $t = 0$. For the double time derivative of u we can say:

$$\ddot{u}(t) = -\omega_0^2 u(t). \tag{4.5}$$

The undamped equation of motion without external forces now becomes:

$$-m\omega_0^2 u(t) + ku(t) = 0 \tag{4.6}$$

and for the (positive) resonance frequency f_0 this results in:

$$f_0 = \frac{\omega_0}{2\pi} = \frac{1}{2\pi}\sqrt{\frac{k}{m}}.$$

4.2.2 The plate element

Similar to the mass-spring-damping situation above, we can describe the elastic deformation of a stiff and thin isotropic plate for which we say the thickness is h. To simulate the behaviour of the plate, we can create a modular model or *mesh* which contains many small two-dimensional plate elements. The thickness can be entered as a variable parameter over the surface. Depending on the approach, the model of the plate can be seen as a grid of small masses, each one interacting with its neighbours through springs and dampers.

Degrees of freedom

We consider a thin rectangular 2-dimensional element, its midsurface located on the (x, y)-plane and with a node on every corner (see Fig. 4.2). We can say that every node has six *degrees of freedom* (DOFs): three translational (u_x, u_y and u_z) and three rotational ones (θ_x, θ_y and θ_z). However, because in our application the amplitudes are relatively small and there is no rotation around the normal of the plane, we neglect u_x, u_y and θ_z at the node locations[1], thus leaving over three DOFs per node. We will write the nodal vectors for a certain node m as follows:

$$\boldsymbol{u}^{(\mathrm{m})} = \begin{bmatrix} u_z^{(\mathrm{m})} \\ \theta_{\mathrm{x}}^{(\mathrm{m})} \\ \theta_{\mathrm{y}}^{(\mathrm{m})} \end{bmatrix} \qquad \dot{\boldsymbol{u}}^{(\mathrm{m})} = \begin{bmatrix} \dot{u}_z^{(\mathrm{m})} \\ \dot{\theta}_{\mathrm{x}}^{(\mathrm{m})} \\ \dot{\theta}_{\mathrm{y}}^{(\mathrm{m})} \end{bmatrix} \qquad \ddot{\boldsymbol{u}}^{(\mathrm{m})} = \begin{bmatrix} \ddot{u}_z^{(\mathrm{m})} \\ \ddot{\theta}_{\mathrm{x}}^{(\mathrm{m})} \\ \ddot{\theta}_{\mathrm{y}}^{(\mathrm{m})} \end{bmatrix} \tag{4.7}$$

and for the entire element the *nodal displacement vectors* will be:

$$\boldsymbol{u} = \begin{bmatrix} \boldsymbol{u}^{(1)} \\ \boldsymbol{u}^{(2)} \\ \boldsymbol{u}^{(3)} \\ \boldsymbol{u}^{(4)} \end{bmatrix} \qquad \dot{\boldsymbol{u}} = \begin{bmatrix} \dot{\boldsymbol{u}}^{(1)} \\ \dot{\boldsymbol{u}}^{(2)} \\ \dot{\boldsymbol{u}}^{(3)} \\ \dot{\boldsymbol{u}}^{(4)} \end{bmatrix} \qquad \ddot{\boldsymbol{u}} = \begin{bmatrix} \ddot{\boldsymbol{u}}^{(1)} \\ \ddot{\boldsymbol{u}}^{(2)} \\ \ddot{\boldsymbol{u}}^{(3)} \\ \ddot{\boldsymbol{u}}^{(4)} \end{bmatrix}. \tag{4.8}$$

[1] The displacements u_x and u_y are neglected for the nodes but do exist *inside* the element (see appendix B).

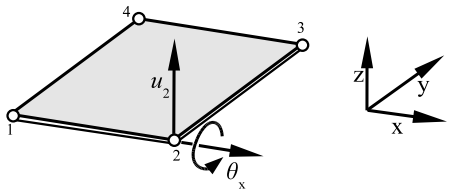

Figure 4.2: Plate element with four nodes. The image shows the displacement u_z and the x-rotation θ_x of node 2.

Force vector

Similar to the nodal displacement vector $\boldsymbol{u}^{(m)}$ and the overall displacement vector $\boldsymbol{u}$ of Eq. 4.7 and Eq. 4.8, we can also write the external load f_{ext} in vector notation. The load vectors for node m and for the entire element become respectively:

$$\boldsymbol{f}^{(m)} = \begin{bmatrix} f_z^{(m)} \\ q_x^{(m)} \\ q_y^{(m)} \end{bmatrix} \qquad \boldsymbol{f} = \begin{bmatrix} \boldsymbol{f}^{(1)} \\ \boldsymbol{f}^{(2)} \\ \boldsymbol{f}^{(3)} \\ \boldsymbol{f}^{(4)} \end{bmatrix} \tag{4.9}$$

with for $q_x^{(m)}$ the *moment* or *torque* at node m with direction x, just like the rotation.

Mass matrix

Instead of the single mass in paragraph 4.2.1, in the plate's finite element model the mass is divided into smaller masses that interact with each other. The *mass matrix* is calculated using the elements' *shape functions* (see appendix B). For thin plates with a fine mesh, this matrix can be diagonalised into a *lumped* mass matrix (MacNeal [38]) where the mass-coupling between elements is neglected. It can be interpreted as dividing the element's mass over its surrounding nodes.

The lumped mass matrix can have the calculational advantage that it can be processed more quickly. For a single element it looks as in Eq. 4.10. In that matrix $V^{(e)}$ is the element volume. Looking at the diagonal of $\boldsymbol{M}^{(e)}$ we see that the mass of the element is evenly divided over the four nodes and, together with the acceleration vector in Eq. 4.8 and the load vector of Eq. 4.9, it can be seen that Newton's second law is obeyed. The zeros in the matrix' diagonal confirm that no force is needed to give a (lumped) point mass a rotational acceleration.

$$\boldsymbol{M}^{(\mathrm{e})} = \frac{1}{4}\rho V^{(\mathrm{e})} \begin{bmatrix} 1 & & & & & & & & \cdots & & & & & & 0 \\ & 0 & & & & & & & & & & & & & \\ & & 0 & & & & & & & & & & & & \\ & & & 1 & & & & & & & & & & & \\ & & & & 0 & & & & & & & & & & \\ & & & & & 0 & & & & & & & & & \\ \vdots & & & & & & 1 & & & & & & & & \vdots \\ & & & & & & & 0 & & & & & & & \\ & & & & & & & & 0 & & & & & & \\ & & & & & & & & & 1 & & & & & \\ & & & & & & & & & & 0 & & & & \\ 0 & & & & & & & & \cdots & & & & & & 0 \end{bmatrix} \tag{4.10}$$

For a model with multiple elements, the global matrix $\boldsymbol{M}$ is formed by combining all element mass matrices $\boldsymbol{M}^{(\mathrm{e})}$. For nodes that are part of more then one element the masses assigned to them have to be summed.

Stiffness matrix

The stiffness matrix $\boldsymbol{K}$ is created in a more complicated way and again the shape functions of appendix B are used. It depends on the *strain*, the relative length change to the length of the element, and the *stress*, the force per unit surface inside the element.

The strain ϵ inside the element can be written in terms of the DOFs vector $\boldsymbol{u}$ and a *strain-displacement matrix* called $\boldsymbol{T}$ (see appendix C):

$$\boldsymbol{\epsilon} = \boldsymbol{T}\boldsymbol{u} \tag{4.11}$$

where the vector $\boldsymbol{\epsilon}$ contains the strains for the different directions:

$$\boldsymbol{\epsilon} \quad = \quad \begin{bmatrix} \epsilon_x & \epsilon_y & \epsilon_{xy} & \epsilon_{yz} & \epsilon_{xz} \end{bmatrix}^{\mathrm{T}}. \tag{4.12}$$

As an example, two of the strain elements from the strain vector are given:

$$\epsilon_x = \frac{\partial u_x}{\partial x} \qquad\qquad \epsilon_{xy} = \frac{\partial u_x}{\partial y} + \frac{\partial u_y}{\partial x}.$$

The normal strain in the z-direction, ϵ_z, is neglected for our thin plate element and therefore left out (Beer [6]).

The stress σ is related to the strain following Hooke's law:

$$\begin{aligned} \boldsymbol{\sigma} &= \boldsymbol{D}\boldsymbol{\epsilon}, \\ \boldsymbol{\epsilon} &= \boldsymbol{D}^{-1}\boldsymbol{\sigma} \end{aligned} \tag{4.13}$$

where $\boldsymbol{D}$ is the *elasticity matrix* and $\boldsymbol{D}^{-1}$ its inverse, often called *flexibility* or *compliance* matrix (see appendix D). The stress vector is built up similar to the strain vector:

$$\boldsymbol{\sigma} = [\sigma_x \quad \sigma_y \quad \sigma_{xy} \quad \sigma_{yz} \quad \sigma_{xz}\ ]^{\mathrm{T}}. \tag{4.14}$$

As an example, the strains ϵ_x and ϵ_{xy} can be expressed in terms of the different stresses (Soedel [51]):

$$\begin{aligned} \epsilon_x &= (\sigma_x - \nu\sigma_y)/E \\ \epsilon_{xy} &= \sigma_{xy}/G \end{aligned} \tag{4.15}$$

with for E the Young's modulus, for ν the Poisson's ratio and G is the *shear modulus*, which is for isotropic materials:

$$G = \frac{E}{2(1+\nu)}.$$

Having determined both matrix $\boldsymbol{T}$ and $\boldsymbol{D}$, the element's stiffness matrix $\boldsymbol{K}^{(\mathrm{e})}$ is calculated by executing the following integration over the volume V of the element (Beer at al.[6]):

$$\boldsymbol{K}^{(\mathrm{e})} = \int_V \boldsymbol{T}^{\mathrm{T}}\boldsymbol{D}\boldsymbol{T}\mathrm{d}V. \tag{4.16}$$

and FE computer algorithms use numerical integration techniques to approximate this solution. To global stiffness matrix $\boldsymbol{K}$ for the complete model is again formed by combining multiple element stiffness matrices.

Damping matrix

As in the mass-spring-damper example, the damping used in our finite element simulations is *viscous* or velocity dependent. Often the damping in finite element simulations is introduced by a *modal damping ratio*, where each resonance has a certain damping value. The plate's transient response simulated in this thesis, however, is not calculated using modal superposition but in a direct way and therefore a different kind of damping technique called *Rayleigh damping* is used. In this approach, the damping depends on the mass and the stiffness of the structure and the damping matrix $\boldsymbol{B}$ is formed proportional to them (Ansys [4] and Prakash [47])[2]:

[2]It should be noted that the Rayleigh damping as such does not appear in reality, it is an approach to be able to describe all real damping effects in a single term.

$$\boldsymbol{B} = \alpha_1 \boldsymbol{M} + \alpha_2 \boldsymbol{K}. \tag{4.17}$$

In this equation the two unknown factors α_1 and α_2 should be determined from two or more damping ratios at unequal frequencies of vibration (Bathe [5]), which can be obtained from an experimental modal analysis. Practically, this means that, using the Rayleigh damping method, the conventional damping ratio η becomes frequency dependent and can be seen as an interpolation between the discrete modal damping factors. It can be written in terms of α_1 and α_2:

$$\eta(\omega) = \frac{1}{2}\alpha_1 \omega^{-1} + \frac{1}{2}\alpha_2 \omega. \tag{4.18}$$

Boundary conditions

As we have seen in the previous paragraph, some degrees of freedom play no part in the simulations. For example, the nodal displacements u_x and u_y, are very small and will therefore be left out of the displacement vector $\boldsymbol{u}$. Matrices $\boldsymbol{M}$, $\boldsymbol{B}$ and $\boldsymbol{K}$ can thus be reduced as well.

The boundary conditions of a plate describe the way it is (or is not) attached to its surroundings. For a plate, three important boundary conditions should be named: *free end*, *simply supported* and *clamped*. The boundary nodes of a free end have the full set of DOFs , just like the nodes inside the plate. In the simply supported case the displacement is zero, meaning only a rotational degree of freedom is present. For the clamped situation all degrees of freedom are zero.

4.2.3 The plate model

Having described the matrices and equations for a single plate element, the step to an FE model for the entire plate is not so big anymore. Each element's node, except the corners of the plate, will be the connection between two or more elements and so displacements and rotations are spread out over the surface. The equation of motion expands from a 1-dimensional equation (Eq. 4.3) to a matrix multiplication:

$$\boldsymbol{M}\ddot{\boldsymbol{u}} + \boldsymbol{B}\dot{\boldsymbol{u}} + \boldsymbol{K}\boldsymbol{u} = \boldsymbol{f}_{\text{ext}} \tag{4.19}$$

where the number of rows and columns in the mass, damping and stiffness matrices ($\boldsymbol{M}$, $\boldsymbol{B}$ and $\boldsymbol{K}$ respectively) equal the total number of degrees of freedom of the modal.

Modal behaviour

Similar to the 1-dimensional case, we can determine the resonance frequencies by solving the equation of motion, now containing (square) matrices with length and height equal

to the degrees of freedom of the model. Typically, these modes are calculated without damping and, in our case, load-free.

The equation of motion for this damp- and load-free model is extracted from Eq. 4.19:

$$\boldsymbol{M}\ddot{\boldsymbol{u}} + \boldsymbol{K}\boldsymbol{u} = 0 \tag{4.20}$$

and, using the properties of the harmonic vibration (see Eq. 4.5), this becomes:

$$-\omega^2\boldsymbol{M}\boldsymbol{u} + \boldsymbol{K}\boldsymbol{u} = 0. \tag{4.21}$$

Removing the displacement from the equation results in an *eigenvalue problem* with the eigenvalue(s) ω^2 and the corresponding eigenvector(s) or *mode shape(s)* ϕ:

$$\boldsymbol{M}^{-1}\boldsymbol{K}\boldsymbol{\phi} = \omega^2\boldsymbol{\phi} \tag{4.22}$$

with for $\boldsymbol{M}^{-1}$ the inverse of the mass matrix, which can be calculated quickly if $\boldsymbol{M}$ is lumped. The mode shape vector $\boldsymbol{\phi}$, also seen in the analytical situation of Paragraph 2.2.2, denotes the condition of all degrees of freedom of the model for the calculated resonance frequency.

4.3 Transient simulation

Because our goal is implementing a time-dependent active noise control algorithm into the finite element model, we need to simulate the plate behaviour in the time domain. Again, we have a discrete time with step size Δt.

4.3.1 Equations of motion

Following the equation of motion in paragraph 4.2.3 and the structural matrices in paragraph 4.2.2, the equations of motion for a structure at two points in time, n and $n+1$, are:

$$\begin{array}{ccccccc} \boldsymbol{M}\ddot{\boldsymbol{u}}_n & + & \boldsymbol{B}\dot{\boldsymbol{u}}_n & + & \boldsymbol{K}\boldsymbol{u}_n & = & \boldsymbol{f}_{\text{ext,n}} \\ \boldsymbol{M}\ddot{\boldsymbol{u}}_{n+1} & + & \boldsymbol{B}\dot{\boldsymbol{u}}_{n+1} & + & \boldsymbol{K}\boldsymbol{u}_{n+1} & = & \boldsymbol{f}_{\text{ext},n+1} \end{array} \tag{4.23}$$

In the following paragraph we will see that if we know the situation at time n and the load $\boldsymbol{f}$ at time $n+1$, we can estimate the motion at this next point in time.

4.3.2 Newmark

The Newmark-β method is a numerical integration method and says that the change in velocity during time interval Δt (for example between time n and time $n+1$) can be estimated using the average acceleration during this time interval. This acceleration is

interpolated between the values of time n and time $n+1$ using a factor β (Newmark [41] and MacNeal [38]):

$$\dot{\boldsymbol{u}}_{n+1} - \dot{\boldsymbol{u}}_n = \big((1-\beta)\ddot{\boldsymbol{u}}_n + \beta\ddot{\boldsymbol{u}}_{n+1}\big)\Delta t. \tag{4.24}$$

The same can be said for the change in displacement from n to $n+1$:

$$\boldsymbol{u}_{n+1} - \boldsymbol{u}_n = \big((1-\beta)\dot{\boldsymbol{u}}_n + \beta\dot{\boldsymbol{u}}_{n+1}\big)\Delta t. \tag{4.25}$$

In this thesis the neutral and most common value for β is used: $\frac{1}{2}$. After some manipulation Eq. 4.24 and 4.25 become:

$$\begin{aligned} \dot{\boldsymbol{u}}_{n+1} &= \dot{\boldsymbol{u}}_n + \tfrac{1}{2}\Delta t\,(\ddot{\boldsymbol{u}}_n + \ddot{\boldsymbol{u}}_{n+1}) \\ \boldsymbol{u}_{n+1} &= \boldsymbol{u}_n + \Delta t\,\dot{\boldsymbol{u}}_n + \tfrac{1}{4}\,(\Delta t)^2\,(\ddot{\boldsymbol{u}}_n + \ddot{\boldsymbol{u}}_{n+1})\,. \end{aligned} \tag{4.26}$$

Here the displacement $\boldsymbol{u}_{n+1}$ and the velocity $\dot{\boldsymbol{u}}_{n+1}$ have been written out to be eliminated after insertion in the equation of motion, but also other approaches are possible.

Inserting the previous two equations in Eq. 4.23 for time $n+1$ we obtain:

$$\begin{aligned} \boldsymbol{M}\ddot{\boldsymbol{u}}_{n+1} \;+\; & \boldsymbol{B}\big(\dot{\boldsymbol{u}}_n + \tfrac{1}{2}\Delta t\,(\ddot{\boldsymbol{u}}_n + \ddot{\boldsymbol{u}}_{n+1})\big) \;+ \\ & \boldsymbol{K}\big(\boldsymbol{u}_n + \Delta t\,\dot{\boldsymbol{u}}_n + \tfrac{1}{4}\,(\Delta t)^2\,(\ddot{\boldsymbol{u}}_n + \ddot{\boldsymbol{u}}_{n+1})\big) \;=\; \boldsymbol{f}_{\text{ext},n+1} \end{aligned}$$

and rearranged it becomes:

$$\begin{aligned} \big(\boldsymbol{M} + \tfrac{1}{2}\Delta t\boldsymbol{B} + \tfrac{1}{4}\,(\Delta t)^2\,\boldsymbol{K}\big)\ddot{\boldsymbol{u}}_{n+1} &= \\ \boldsymbol{f}_{\text{ext},n+1} - \boldsymbol{K}\boldsymbol{u}_n - & \;\Delta t\boldsymbol{K}\dot{\boldsymbol{u}}_n - \tfrac{1}{4}\Delta t(2\boldsymbol{B} + \Delta t\boldsymbol{K})\ddot{\boldsymbol{u}}_n. \end{aligned} \tag{4.27}$$

For convenience, we use two substitute matrices, $\boldsymbol{\Gamma_1}$ and $\boldsymbol{\Gamma_2}$, and we can write Eq. 4.27 as follows:

$$\boldsymbol{\Gamma}_1\ddot{\boldsymbol{u}}_{n+1} = \boldsymbol{f}_{\text{ext},n+1} - \boldsymbol{K}\,(\boldsymbol{u}_n + \Delta t\dot{\boldsymbol{u}}_n) + \boldsymbol{\Gamma}_2\ddot{\boldsymbol{u}}_n \tag{4.28}$$

with

$$\boldsymbol{\Gamma}_1 \;=\; \boldsymbol{M} + \tfrac{1}{2}\Delta t\boldsymbol{B} + \tfrac{1}{4}\,(\Delta t)^2\,\boldsymbol{K}$$

$$\boldsymbol{\Gamma}_2 \;=\; -\tfrac{1}{4}\Delta t(2\boldsymbol{B} + \Delta t\boldsymbol{K})$$

Finally, matrix $\boldsymbol{\Gamma}_1$ is inverted to leave over the unknown $\ddot{\boldsymbol{u}}_{n+1}$ on the left hand side:

$$\ddot{\boldsymbol{u}}_{n+1} = \boldsymbol{\Gamma}_1^{-1}\Big(\boldsymbol{f}_{\text{ext},n+1} - \boldsymbol{K}\,(\boldsymbol{u}_n + \Delta t\dot{\boldsymbol{u}}_n) + \boldsymbol{\Gamma}_2\ddot{\boldsymbol{u}}_n\Big). \tag{4.29}$$

With Eq. 4.29 we can now estimate the acceleration $\ddot{\boldsymbol{u}}_{n+1}$ using the known situation at time n and the load at time $n+1$. With the new acceleration we can use Eq. 4.26 to calculate $\boldsymbol{u}_{n+1}$ and $\dot{\boldsymbol{u}}_{n+1}$ and finally have all information for this next time-step.

4.4 Acoustic radiation in FEM

We consider a three-dimensional coordinate system (x, y, z) and a plate that is placed in its $(z = 0)$-plain. Point B is located on the plate and we will calculate the pressure in a certain point A away from the plate ($z_\mathrm{A} > 0$) (see Fig. 4.3). The center of the plate and the two mentioned points can be written as:

$$\boldsymbol{x}_0 = \begin{bmatrix} 0 \\ 0 \\ 0 \end{bmatrix}, \qquad \boldsymbol{x}_\mathrm{A} = \begin{bmatrix} x_\mathrm{A} \\ y_\mathrm{A} \\ z_\mathrm{A} \end{bmatrix}, \qquad \boldsymbol{x}_\mathrm{B} = \begin{bmatrix} x_\mathrm{B} \\ y_\mathrm{B} \\ 0 \end{bmatrix}.$$

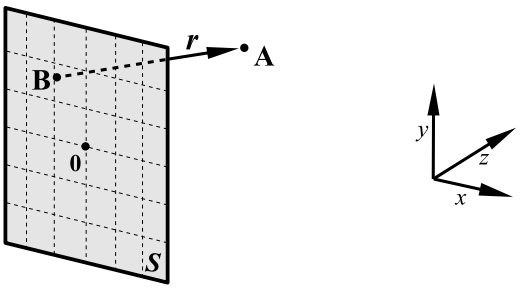

Figure 4.3: Plate S with point B and in front of it point A, r is the distance between A and B.

The distance r between point A and point B is now:

$$r = \sqrt{(x_\mathrm{A} - x_\mathrm{B})^2 + (y_\mathrm{A} - y_\mathrm{B})^2 + (z_\mathrm{A})^2}.$$

The point A at a certain distance from the plate is considered far enough not to be influenced by near-field effects. This means that:

$$kz_\mathrm{A} >> 1, \tag{4.30}$$

with wavenumber k and c_0 is the acoustic propagation velocity in air at room temperature:

$$k = \frac{2\pi f}{c_0}$$

4.4.1 Rayleigh integral of the first kind

The *Rayleigh integral of the first kind* shows us that, in case of weak coupling of structure and surrounding fluid, the frequency domain pressure $\tilde{P}_\mathrm{A}(\boldsymbol{x}_\mathrm{A}, f)$ can be calculated by integrating the plate's normal velocity in the z-direction, $\tilde{U}_z$, times a phase and amplitude factor over the plate surface (Berkhout [10]):

$$\tilde{P}_{\mathrm{A}}(f) = \mathrm{j}\rho_0 f \int_S \frac{1}{r}\, \tilde{\dot{U}}_z(\boldsymbol{x}, f)\, \mathrm{e}^{-\mathrm{j}kr}\ \mathrm{d}S, \tag{4.31}$$

with for ρ_0 the density of air, again at room temperature.

For the finite element simulation case, the plate's normal velocity is not a continuous function, but only known for M discrete nodes on the plate and each node represents a finite surface $S^{(\mathrm{m})}$. The velocity is considered to be constant over each of those surfaces. The previous integral equation transforms into a summation, with for $r^{(\mathrm{m})}$ the distance from node m to point A:

$$\tilde{P}_{\mathrm{A}}(f) = \mathrm{j}\rho_0 f \sum_{m=1}^{M} S^{(\mathrm{m})} \frac{1}{r^{(\mathrm{m})}}\, \tilde{\dot{U}}_z^{(\mathrm{m})}(f)\, \mathrm{e}^{-\mathrm{j}kr^{(\mathrm{m})}}. \tag{4.32}$$

For convenience, the direction z is omitted in the displacement and velocity notations from now on, for we are only interested in the normal direction. Roughly we can say that the mentioned surface per node is constant and equals the surface of the plate, S, through the number of nodes M. Now we get:

$$\tilde{P}_{\mathrm{A}}(f) = \mathrm{j}f \frac{\rho_0 S}{M} \sum_{m=1}^{M} \frac{1}{r^{(\mathrm{m})}} \tilde{\dot{U}}^{(\mathrm{m})}(f)\, \mathrm{e}^{-\mathrm{j}kr^{(\mathrm{m})}}. \tag{4.33}$$

In case we only know the displacement at the nodes and not the velocity (as for the mode shapes discussed in Paragraph 2.2.2 and appendix A), the velocity, being a time-derivative, can be replaced with $\mathrm{j}2\pi f$. The equation now becomes:

$$\tilde{P}_{\mathrm{A}}(f) = -2\pi f^2 \frac{\rho_0 S}{M} \sum_{m=1}^{M} \frac{1}{r^{(\mathrm{m})}} \tilde{U}^{(\mathrm{m})}(f)\, \mathrm{e}^{-\mathrm{j}kr^{(\mathrm{m})}} \tag{4.34}$$

4.4.2 Time domain Rayleigh integration

To obtain the *time-dependent* pressure in A we need the *inverse Fourier transform* (IFT) of Eq. 4.34. It can be obtained by using a few Fourier transform rules (Oppenheim [44]):

$$\begin{aligned}
\tilde{Y}(f) &\xrightarrow{\mathrm{IFT}} y(t), \\
\alpha\tilde{Y}(f) &\xrightarrow{\mathrm{IFT}} \alpha y(t), \\
\tilde{Y}_1(f) + \tilde{Y}_2(f) &\xrightarrow{\mathrm{IFT}} y_1(t) + y_2(t), \\
\mathrm{j}2\pi f\tilde{Y}(f) &\xrightarrow{\mathrm{IFT}} \dot{y}(t), \\
\tilde{Y}(f)\, \mathrm{e}^{-\mathrm{j}kr} &\xrightarrow{\mathrm{IFT}} y\left(t - r/c_0\right).
\end{aligned} \tag{4.35}$$

Obeying these rules, Eq. 4.33 in the time domain becomes:

$$p_{\mathrm{A}}(t) = \frac{\rho_0 S}{2\pi M} \sum_{m=1}^{M} \frac{1}{r^{(\mathrm{m})}} \ddot{u}^{(\mathrm{m})} \left(t - r^{(\mathrm{m})}/c_0 \right) \tag{4.36}$$

This shows that we can calculate the pressure in A using the past acceleration data $\ddot{u}$. The applied time delay $r^{(\mathrm{m})}/c_0$ depends on the location of node m: the closer this node is to point A, the sooner the vibration induced pressure wave arrives there and the shorter the time delay will be.

Discrete time radiation

To estimate the correct pressure in a point in the far field, the time delays for all nodes need to be calculated. Dealing with the discrete time instead of the continuous time of Eq. 4.36 an extra processing step is required.

Using a discrete buffer with acceleration data, the time delay needs to be an integer. When the real delay r_m/c_0 equals, for example, $6.4\Delta t$, we need to interpolate between $\ddot{u}^{(\mathrm{m})}[n-6]$ and $\ddot{u}^{(\mathrm{m})}[n-7]$. In general, the step from continuous to discrete will look like:

$$\ddot{u}\left(t - r/c_0\right) \longrightarrow \gamma_1 \ddot{u}\left[n - \zeta\right] + \gamma_2 \ddot{u}\left[n - \zeta - 1\right], \tag{4.37}$$

with for the *time delay integer* ζ for a certain node m:

$$\zeta^{(\mathrm{m})} = \left\lfloor \frac{r^{(\mathrm{m})}}{c_0 \Delta t} \right\rfloor$$

and $\lfloor \ldots \rfloor$ denotes the *floor function* which rounds towards the lower integer (see also Fig. 4.4). The positive constants γ_1 and γ_2 depend on the M nodes and are calculated as follows:

$$\begin{aligned} \gamma_1^{(\mathrm{m})} &= \tfrac{r^{(\mathrm{m})}}{c_0 \Delta t} - \zeta^{(\mathrm{m})} \\ \gamma_2^{(\mathrm{m})} &= \zeta^{(\mathrm{m})} + 1 - \tfrac{r^{(\mathrm{m})}}{c_0 \Delta t} = 1 - \gamma_1^{(\mathrm{m})}. \end{aligned} \tag{4.38}$$

Applying this interpolation on the radiation formula of Eq. 4.36 and so transforming it to the discrete time, we get:

$$p_{\mathrm{A}}[n] = \frac{\rho_0 S}{2\pi M} \sum_{m=1}^{M} \frac{1}{r^{(\mathrm{m})}} \left(\gamma_1^{(\mathrm{m})} \ddot{u}^{(\mathrm{m})} \left[n - \zeta^{(\mathrm{m})} \right] + \gamma_2^{(\mathrm{m})} \ddot{u}^{(\mathrm{m})} \left[n - \zeta^{(\mathrm{m})} - 1 \right] \right). \tag{4.39}$$

For every node m we first need to calculate the distance r and then time delay ζ. With these two we can determine the factors γ_1 and γ_2 and use the appropriate acceleration values $\ddot{u}\left[n - \zeta\right]$ and $\ddot{u}\left[n - \zeta - 1\right]$.

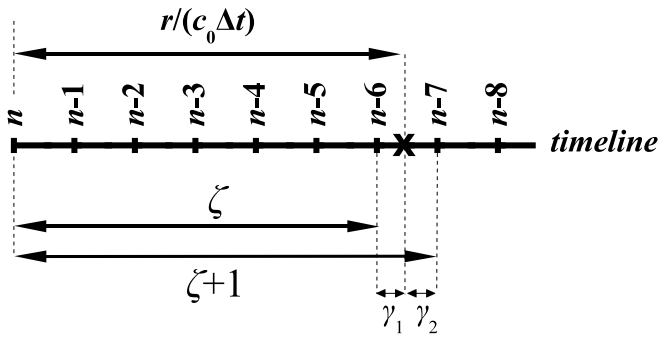

Figure 4.4: Graphical interpretation of the time buffer and the interpolation. The real time delay is $r/(c_0\Delta t) = 6.4$ and the **X** shows it on the time-line, γ_1 (here: 0.4) and γ_2 (here 0.6) represent the distance from this point to $[n-6]$ and $[n-7]$ respectively.

The bigger part of these calculation steps only needs to be done once before the start of the transient simulation. We can store the information in a matrix we call $\boldsymbol{Q}_{\mathrm{A}}$ and can then multiply it with the acceleration buffer matrix $\ddot{\boldsymbol{U}}[n]$. The result will be a matrix too, size $M \times M$ with on the diagonal the contributions of all nodes to the pressure in A. The summation over these diagonal elements, denoted with $\sum^{\mathrm{diag}}$, will give us the appropriate pressure $p_{\mathrm{A}}[n]$:

$$p_{\mathrm{A}}[n] = \sum^{\mathrm{diag}} \left(\boldsymbol{Q}_{\mathrm{A}} \ddot{\boldsymbol{U}}[n] \right). \tag{4.40}$$

In this equation the buffer matrix with the acceleration data is:

$$\ddot{\boldsymbol{U}}[n] = \begin{bmatrix} \ddot{\boldsymbol{u}}_1[n] & \cdots & \ddot{\boldsymbol{u}}_M[n] \end{bmatrix} = \begin{bmatrix} \ddot{u}^{(1)}[n] & \cdots & \ddot{u}^{(\mathrm{M})}[n] \\ \ddot{u}^{(1)}[n-1] & \cdots & \ddot{u}^{(\mathrm{M})}[n-1] \\ \vdots & & \vdots \\ \ddot{u}^{(1)}[n-\ell] & \cdots & \ddot{u}^{(\mathrm{M})}[n-\ell] \\ \vdots & & \vdots \\ \ddot{u}^{(1)}[n-\zeta_{\max}-1] & \cdots & \ddot{u}^{(\mathrm{M})}[n-\zeta_{\max}-1] \end{bmatrix}$$

and $\zeta_{\max}$ equals the maximum $\zeta^{(\mathrm{m})}$ for all M nodes.

The matrix $\boldsymbol{Q}_{\mathrm{A}}$ in Eq. 4.40 will have a structure similar to the following:

$$\boldsymbol{Q}_{\mathrm{A}} = \frac{\rho_0 S}{2\pi M} \begin{bmatrix} 0 & \cdots & 0 & \gamma_1^{(1)}/r^{(1)} & \gamma_2^{(1)}/r^{(1)} & 0 & \cdots & 0 & 0 \\ \vdots & & \vdots & \vdots & \vdots & \vdots & & \vdots & \\ 0 & \cdots & \gamma_1^{(\mathrm{m})}/r^{(\mathrm{m})} & \gamma_2^{(\mathrm{m})}/r^{(\mathrm{m})} & 0 & 0 & \cdots & 0 & 0 \\ \vdots & & \vdots & \vdots & \vdots & \vdots & & \vdots & \vdots \\ 0 & \cdots & 0 & 0 & 0 & 0 & \cdots & \gamma_1^{(\mathrm{M})}/r^{(\mathrm{M})} & \gamma_2^{(\mathrm{M})}/r^{(\mathrm{M})} \end{bmatrix}.$$

For every row in $\boldsymbol{Q}_{\mathrm{A}}$, meaning every node m, the integer $\zeta^{(\mathrm{m})}$ is calculated and the value $\left(\rho_0 S^{(\mathrm{m})}/2\pi M r^{(\mathrm{m})}\right)\gamma_1$ is placed in the $\zeta^{(\mathrm{m})}$-th position of that row. The neighbouring location to the right, position $\zeta^{(\mathrm{m})}+1$, becomes the value $\left(\rho_0 S^{(\mathrm{m})}/2\pi M r^{(\mathrm{m})}\right)\gamma_2$. In matrix element notation we can write for $\boldsymbol{Q}_{\mathrm{A}}$:

$$Q_{\mathrm{A}}\left(m,\zeta^{(\mathrm{m})}\right)=\frac{\rho_0 S\gamma_1^{(\mathrm{m})}}{2\pi M r^{(\mathrm{m})}} \qquad \text{and} \qquad Q_{\mathrm{A}}\left(m,\zeta^{(\mathrm{m})}+1\right)=\frac{\rho_0 S\gamma_2^{(\mathrm{m})}}{2\pi M r^{(\mathrm{m})}}$$

and all other elements in $\boldsymbol{Q}_{\mathrm{A}}$ are zero[3].

4.5 Conclusions

The finite element approach is a powerful tool to numerically estimate a structure's static and dynamic behaviour due to loads. Consisting out of small elements which behave according to well defined rules, the simulated model is a prediction tool for the real structure.

The dynamic behaviour of a finite element model is usually simulated in the frequency domain using modal analysis and modal superposition. A steady state situation is simulated with loads that have amplitude and phase, possibly depending on the frequency.

Although the transmission loss of a panel could be simulated in the frequency domain, the implementation of a (usually) time domain ANC algorithm would then be impossible. For this reason a time-dependent FE simulation is chosen, based on the Newmark-β method.

Air elements could also be integrated in the FE model. This could simulate the acoustic waves travelling towards and from the plate. However, including air elements would increase the size of the modal extensively. For that reason an air-free model has been chosen and radiation is calculated according to the radiation formula of Rayleigh. Also this equation has been transformed and adapted to fulfil our needs.

The last three chapters have been quite theoretical and general, discussing the following themes: transmission loss, active noise control and finite element simulation. The chapters form a steady basis to the next, more practical chapter: it will deal with the set-up of the measurement and the algorithms used for the simulations.

[3]Most calculation software programs offer a technique to reduce the used memory of a matrix like $\boldsymbol{Q}$ immensely by only storing the non-zero matrix elements, leaving out the zeros.

Chapter 5

Set-up of Experiment and Simulation

5.1 Introduction

In between the more general theoretical introductions on the one side and the practical results of the measurements and simulations on the other, an important chapter is presented here. It discusses the way in which the results of our investigations were obtained.

The first part of this chapter deals about the experiments and describes how the transmission loss and active noise control measurements are set-up. For the transmission loss there is not much too much choice: the ISO certification requires requires a rather strict working procedure, room specifications and equipment rules. Even the post-processing and presentation of the data is restricted (see Chapter 2).

The build-up of a functioning model that simulates the transmission loss and the ANC implementation forms the second part of this chapter. After the theoretical investigations of the last three chapters still much has to be done to create a working simulation. The equations of the previous chapters that are directly used in the simulation algorithms are repeated for readability reasons.

Although the previous chapter already discussed how to calculate the acoustic radiation from the plate to the error sensors, the modelling of the *incoming* noise has not been presented yet. The technique proposed here looks similar to the radiation approach and will be explained in this chapter as a part of the simulated noise types.

Determining the operation methods and implementing the algorithms for system identification and active noise control are presented in the last part of this chapter. Instead of offering long and complicated computer code listings, the step-by-step procedures are explained with the use of flow-charts.

5.2 Experiment set-up

All experiments of which the results are shown in this thesis are carried out during summer 2006 in the acoustical laboratory of EADS Corporate Research Center GmbH[1] in Ottobrunn, Germany.

5.2.1 Transmission Loss

As noted in paragraph 2.3 the transmission loss of a plate can be measured by building it into the opening of a heavy wall between a reverberation room and an anechoic room. Broadband noise on the loudspeakers inside the reverberation room will build up a diffuse sound field[2] and some of the acoustic energy will be transferred by the plate into the next room. The ratio of the incident intensity on the plate and the radiated intensity by the plate as a function of frequency is the transmission loss in which we are interested. For accurate results, the minimum length of the time measurements should be taken into account (ISO 15186 [30]).

Source side

The reverberation room used (see Fig. 5.1) has a volume of approx. 130 m^3 and a total surface (wall, floor and ceiling) of approx. 150 m^2. Placed inside are two loudspeakers (JBL SP225-9, 1200 W) which get their signal from two independent channels. The two noise generators (Brüel & Kjaer 1405) produce white noise which is led into a mixer (PCM-25). The mixer filters the signals with a low-pass filter that filters out signal components above 20 kHz and (pre-)amplifies the rest before finally going through the power amplifier (Crown CE4000, 2x1200 W) (see Fig. 5.2).

The sound pressure in the reverberation room is measured using a 1/2-inch random-incidence microphone (G.R.A.S. Sound & Vibration, type: 40AR) fixed on a rotating arm for better estimation of the average sound pressure level in the room.

The temperature, the (static) air pressure and the humidity during the experiments are measured and to be found approximately:

- Temperature: $T = 20^{o}$ C
- Air pressure: $p_0 = 96 \cdot 10^3$ Pa
- Relative humidity: $\eta_{\text{hu}} = 50$ %.

[1] At the time of publishing this thesis the laboratory name has changed into EADS Innovation Works

[2] A reverberation room always has a minimum frequency below which the sound field is not "diffuse enough". For the room used this frequency limit is approx. 100 Hz.

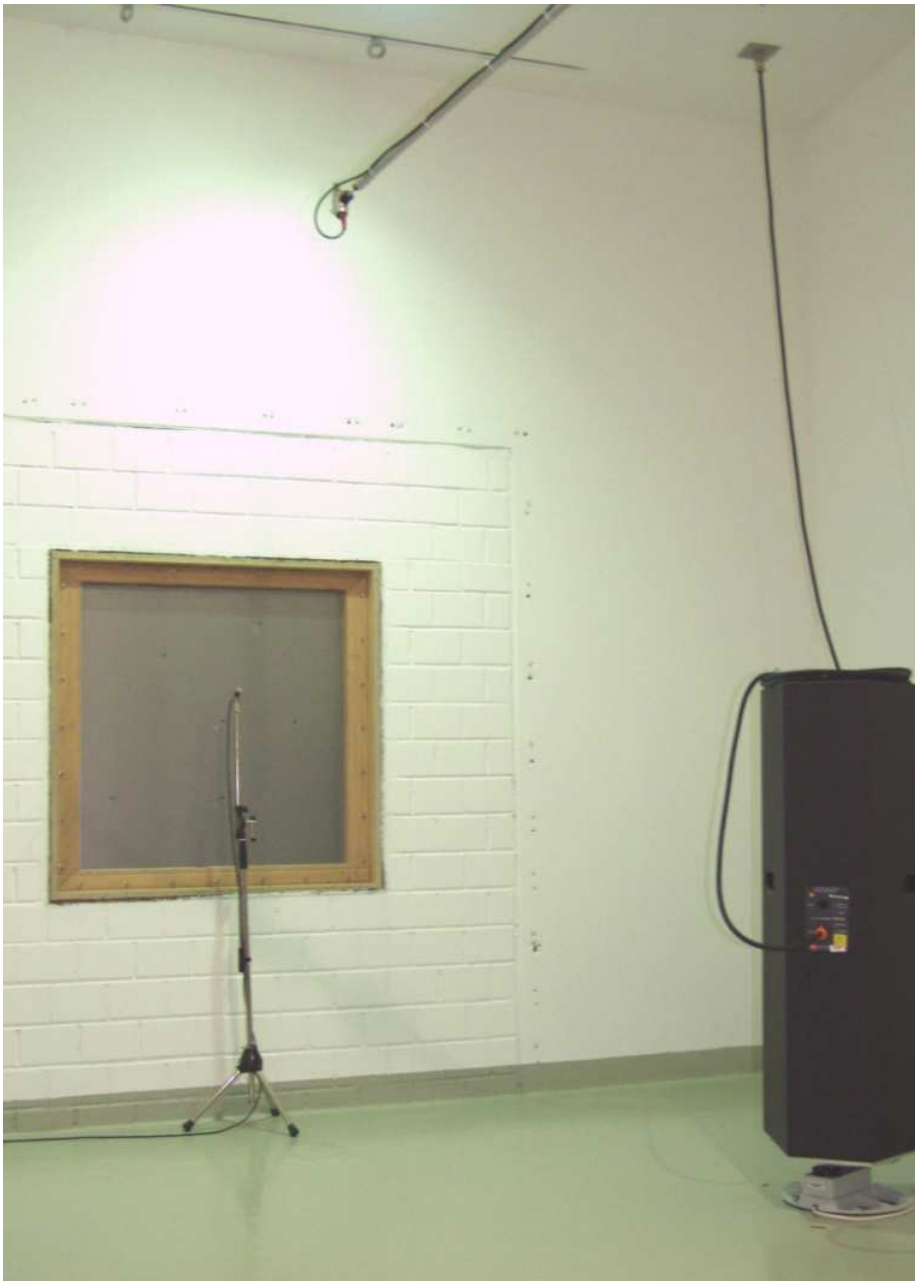

Figure 5.1: Reverberation room and source side. What can be seen is the plate built inside the wall, one of the two loudspeakers and the rotatable microphone arm on the ceiling can be seen. The microphone in front of the plate is the ANC reference microphone.

Using these values we come to the following two important properties of the air (Verkerk [54]), which are used for the calculations and the simulations:

- Speed of sound: $c_0 = 345$ m/s
- Air density: $\rho_0 = 1.13$ kg/m^3.

Figure 5.2: *From top to bottom*: Random noise generators (Brüel & Kjaer, type: 1405), Mixer (PCM, type: 25), Amplifier (Crown, type: CE4000).

Baffle and plate

The plate to be measured is fixed airtight inside a heavy wooden frame which is built into the massive wall. From both sides rubber strips press on the boundaries of the plate and carry its weight. Although in reality a mixture of clamped and simply supported boundaries, for the simulations the boundary conditions are considered to be *simply supported*.

The dimensions of the test panel used for the experiments are predetermined by the laboratory facility[3]. The material properties of the aluminium plate used for calculations and simulations are taken from the literature (INA [27]):

- Thickness: $h = 1.0 \cdot 10^{-3}$ m

[3] A different plate size than the one used in this dissertation is possible. Smaller sizes require an adapted frame conform the standard restriction (ISO 140-1 [29]) and lowest frequency boundaries will increase. A larger plate size would require major changes of the wall between reverberant and anechoic rooms.

- Width: $L_x = 0.96$ m
- Height: $L_y = 0.94$ m
- Density: $\rho = 2.7 \cdot 10^3$ kg/m^3
- Young's modulus: $E = 70 \cdot 10^9$ Pa
- Poisson's ratio: $\nu = 0.35$.

For comparison, the transmission loss of a steel plate is also measured and has the same dimensions. The other parameters of steel are:

- Density: $\rho = 7.9 \cdot 10^3$ kg/m^3
- Young's modulus: $E = 210 \cdot 10^9$ Pa
- Poisson's ratio: $\nu = 0.30$.

Using Eq. 2.23, the critical frequency f_{cr} at an incidence angle of 78$^{\text{o}}$ is for both plates about 12.5 kHz.

Receiver side

At the receiving side of the measurement set-up we find an anechoic room with acoustic isolation at the walls, the floor and the ceiling. The isolation consists of wedges of isolating material with a length of about 0.80 m, which means that sound is effectively absorbed for frequencies higher than approx. 100 Hz. A frame with rail and electric motor is situated about 0.5 m from the baffle (see Fig. 5.3) and carries an arm with an intensity probe (TFS Technische Akustik, type: SIP 101/SBS3i) (see Fig. 5.4). This probe contains three microphones and the distances between them are 8 mm and 42 mm. Due to this three-microphone construction a reliable intensity measurement can be made from approx. 80 Hz to 8 kHz. The distance between the first microphone and the plate is approx. 0.4 m. Connected to a computer the intensity probe can be moved to any point in the plane at 0.4 m in front of the plate.

All microphones including the one in the reverberation room are connected to a personal computer with the appropriate hard- and software. This computer also controls the intensity probe arm. In the measurement program (μ-Remus) a grid of 10×10 equidistant points spread over the plate's surface is generated for which the intensity is measured. A measurements sequence is automated in such a way that between two measurements the intensity probe will move towards the next point on the grid. Output of the program are the intensity for every grid point and the transmission loss, both 1/3-octave band based.

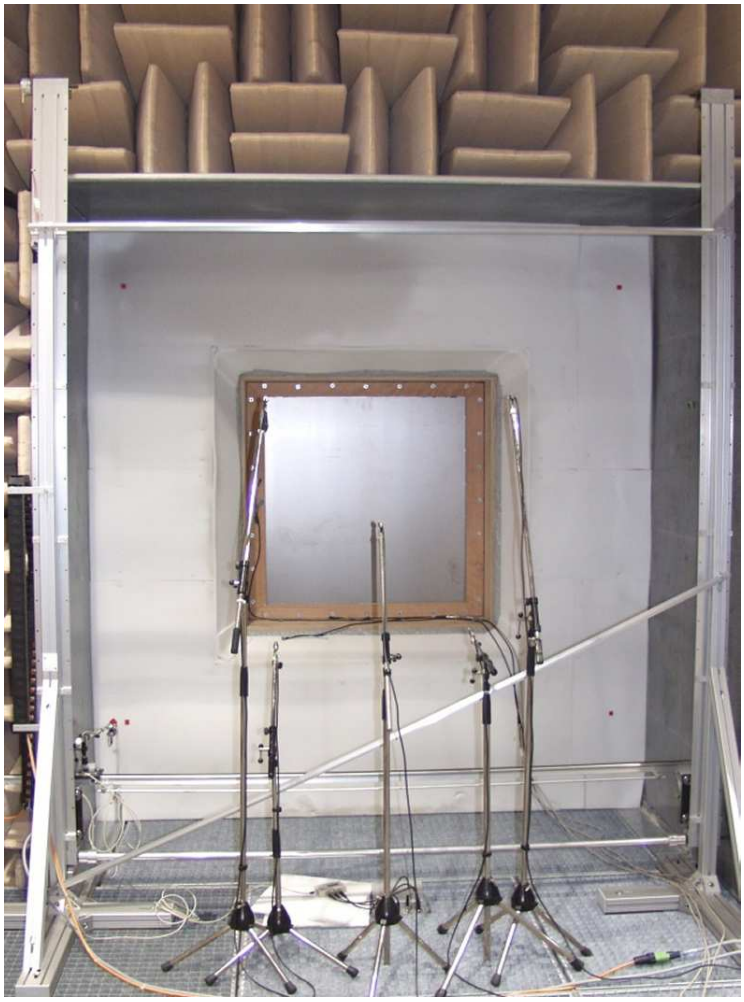

Figure 5.3: Receiver side of the plate in the anechoic room. The intensity probe rail can be seen with its origin in the bottom left corner, as well as the five error microphones with stands.

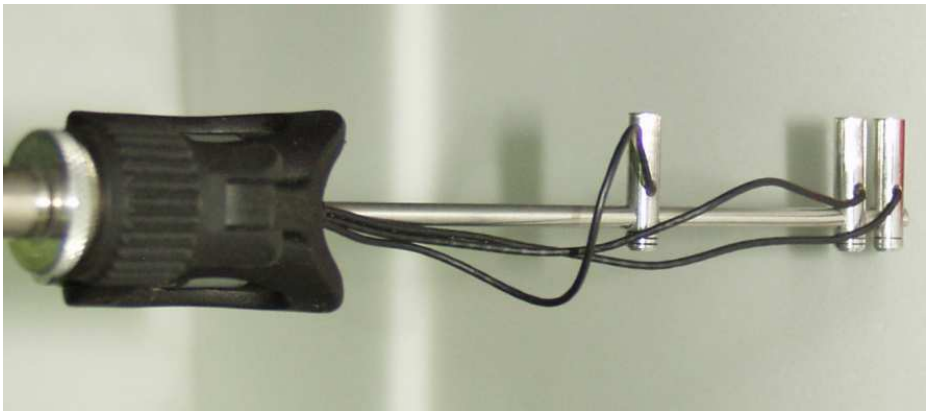

Figure 5.4: The intensity probe (TFS Technische Akustik, type: SIP 101/SBS3i) with its three microphone heads. The spacings between the heads are 8 mm and 42 mm, resulting in a frequency range of approximately 80 Hz - 8 kHz.

5.2.2 Modal analysis

To experimentally determine the resonance modes of the plate built inside the baffle, a modal analysis can be done. This is done by determining many frequency response functions (FRFs) from one point of the plate to another using a force measuring hammer and one or more accelerometers. Using the *roving hammer* technique one can fix the accelerometers spread over the plate and hit the plate according to a predetermined pattern. Advantage is that this way the accelerometers need not be moved during the entire measurement procedure. The responses at the accelerometers due to the hammer impacts are recorded and the FRFs are calculated.

Special post-processing software is available that imports the FRFs and the positions of hammer and accelerometers. The FRFs are compared and if common peaks are found, the displacement amplitudes of the points are listed as the shape of the structure that belongs to that resonance frequency. From the width of the peaks the *damping factor* for that specific mode can be extracted.

The recording equipment used for this modal analysis is an 8t-channel LMS Test.Xpress. One channel is for the impact hammer (PCB 086C02, with such a tip that is hard enough to ensure high enough frequencies) and the other seven channels are used for the accelerometers (PCB 353B15, 2.0 gram), which are spread out over the plate to pick up most of the modes. A pattern of 100 measuring points is determined and positions are marked on the plate (see Fig. 5.5). The FRF form these positions to the accelerometers is determined and post-processing is done using the software LMS CADA-X. To investigate a possible influence of the accelerometer masses on the modal behaviour of the plate, a simulational modal analysis with and without actuator masses has been executed. Results can be found in paragraph 6.2.

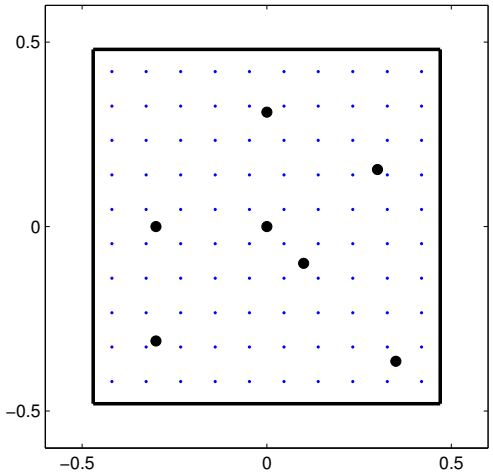

Figure 5.5: Schematic representation of the plate with the accelerometers (black dots) and the hammer impact positions (blue dots).

5.2.3 Active noise control

The controller

The active noise controller used for the experiments is made in the year 2000 by *TNO* and has as operating system *Real Time Linux* (RTLinux). For the suppression of stochastic noise the controller has a maximum of three output channels and six input channels, meaning the maximum dimension of the ANC set-up with reference channel is: $J \times K \times M = 1 \times 5 \times 3$).

The analogue-digital/digital-analogue (AD/DA) converter card has a voltage limit of $V = \pm 10$ volt and has a fixed sample rate of $f_{\mathrm{s,AD}} = 15\ 625$ Hz. The ANC algorithm sample rate f_{s} is synchronised with this fixed frequency through a software adjustable downscale factor a:

$$f_{\mathrm{s}} = \frac{f_{\mathrm{s,AD}}}{a}. \tag{5.1}$$

Between two samples a time of $1/f_{\mathrm{s}}$ seconds is left for the controller to execute the following steps:

- acquire the input signals (reference and errors)
- anti-alias filter and downsample those signals
- add the new samples to their buffers
- execute the controller algorithm
- upsample and filter the actuator signals
- process the signals for the graphical user interface.

The downscale factor a determines the highest frequency possible to be controlled. Setting a, it should be taken into account that all above mentioned operations have to be executed for every sample. For a bandwidth up to about 800 Hz we come to a downscale factor of $a = 8$. Tests have shown that with this downscale factor and full channel usage ($1 \times 5 \times 3$) the controller still is able to execute the necessary calculations.

Two other controller settings that can be adjusted to fine-tune the controlling are the convergence step-size μ and the weighting factor β (see also paragraph 3.4.1). Default values are $\mu = 0.001$ and $\beta = 0.01$ and experiments have shown that these values are agreeable for all active experiments.

The sensors

On the source side of the plate, the single reference channel needs to pick up the sound field as accurately as possible. For this, a random-incidence microphone (G.R.A.S. Sound & Vibration, type: 40AR) has been placed relatively close to the center of the plate at a distance of 0.2 m. As for the microphone on the rotating arm, the random-incidence property ensures a diffuse sound field pressure measurement without the disturbance of the microphone body.

On the error side we choose the maximum of five microphones, which are 1/2-inch free-field microphones (G.R.A.S. Sound & Vibration, type: 40AE). Free-field means that such a microphone most accurately measures the sound pressure waves coming from a single source and travelling directly towards it (0^o degrees incidence).

To be able to reduce the noise radiated by the plate, a wide area behind it has to be covered by the error microphones. In choosing the error positions, one should take into account that the distance from plate to error microphones should be large enough not to be influenced too much by the plate's near field [4]. If so, the controller might focus on reducing noise that not necessarily radiates into the more important far field. The disadvantage of a large distance between error microphones and secondary actuators (in our case on the plate) is that impulse responses between the two become lengthy in time which reduces the overall ANC performance. The five error microphones are placed on the coordinates of Table 5.1, seen from the center of the plate (see also Fig. 5.3). It should be noted that other positions are possible too, as long as they remain fixed during the measurements.

Microphone nr.	x-coordinate [m]	y-coordinate [m]	z-coordinate [m]
0	0.0	0.0	-0.2
1	-0.38	0.38	1.5
2	0.38	0.38	1.5
3	-0.38	-0.38	1.5
4	-0.38	-0.38	1.5
5	0.0	0.0	1.5

Table 5.1: Position of the reference microphone (nr. 0) and the five error microphones (nr. 1-5). Origin is the center of the plate and the positive z-axis is directed towards the receiver side.

The actuators

In this dissertation we want to use the benefits of active noise control without adding too much mass to the plate. For this purpose, *piezoelectric actuators* are chosen to induce

[4] The acoustic near field is defined as the area close to a sound source in which the pressure and the particle velocity are not in phase. For a monopole this can be approximated by $k.r << 1$ in which k is the wave number and r the distance to the source [10].

the bending waves that will be responsible for the destructive interference at the error sensors. The used actuator type (Midé Technology Corporation, model: ACX QP20w, see Fig. 5.6) is a sandwich of two electrically isolated piezoceramic layers that stretch or contract depending on the applied voltage. The two layers are electrically cross-connected, meaning that, on applying a certain voltage, the layers stretch and contract contrary, resulting into a bending of the transducer. Glued onto the plate, it will force the plate to bend along.

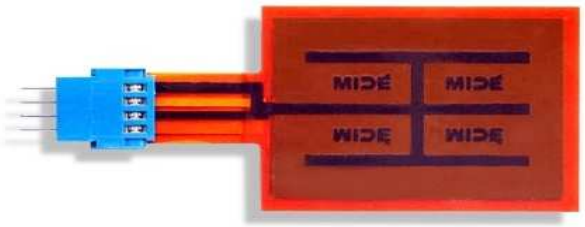

Figure 5.6: Piezo-electric transducer QuickPack QP20w, developed by Midé Technology Corporation [40]. Its dimensions are (length × width × thickness): 51 × 38 × 0.8 mm.

The voltage limit allowed to be applied on the actuators is ±200 V. The voltage amplifier (Walcher Elektronik GmbH, HVA-440/2) has a fixed amplification factor of 20, and, together with the controller's output voltage limit of ±10 volt, the system can not overdrive the piezos.

The piezoelectric actuators can be seen as capacitors and, respecting the voltage and frequency limits, the electric current I for our piezos stays typically low ($I < 100$ mA), meaning a power consumption of maximal $P = V_{\text{RMS}} \cdot I_{\text{RMS}} = 20$ watt. This is the upper limit for this actuator type. In the experiments conducted in this thesis the voltage, current and power consumption were much lower.

Actuator position

To determine the best positions for the three available actuators we need to predict which mode shapes are most dominant for broadband excitation and which mode shapes radiate most efficiently to the error sensors. In order to do so, the *modal participation* can be calculated (see appendix A). As excitation a normal incidence pressure load from 0 Hz - 800 Hz is used and the average (normalised) modal participation for the transmitted noise at the center microphone 5 is calculated. The results for the first 50 modes, sorted to frequency, are plotted in Fig. 5.7.

Fig. 5.8 shows the patterns of the first three most dominant modes: mode 1 (1,1), mode 5 (3,1) and mode 6 (1,3). In these plots the brightness of the colours represents the

displacement perpendicular to the surface. All shapes obey the sine-function as seen in Eq. 2.26 and similar mode shapes can be given for the other dominant modes of Fig. 5.8.

From the analytical mode shape equation it can be seen that the plate coordinates with amplitude maximum will also have maximum bending. To be able to efficiently excite the mentioned dominant modes, the bending actuators should best be glued on those positions. Considering the given results, we choose to glue our three actuators on the positions of Table 5.2. A picture of the plate with the three actuators can be seen in Fig. 5.9.

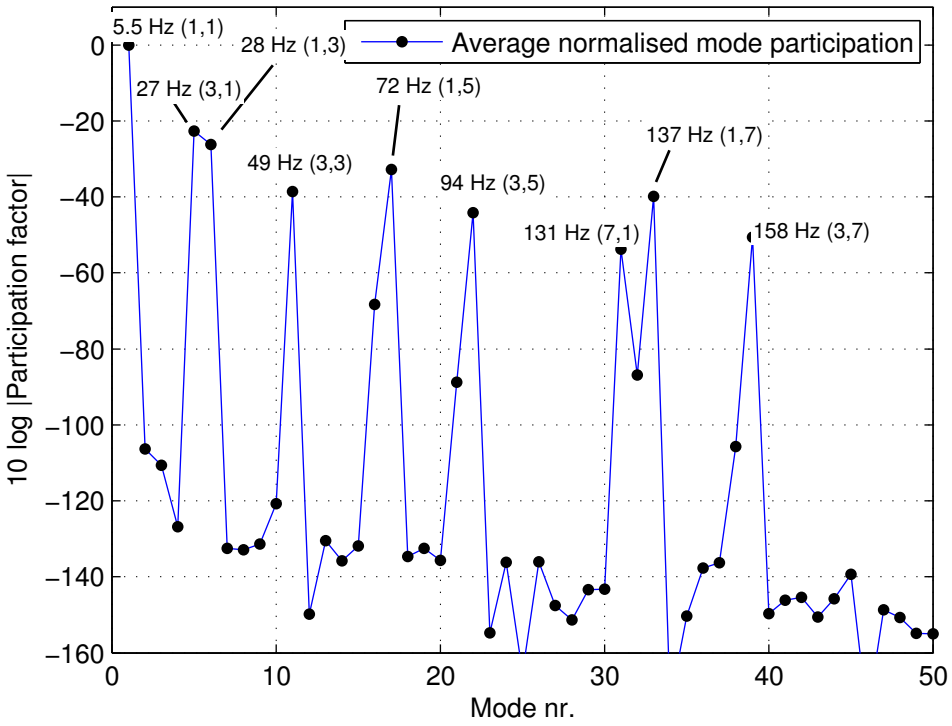

Figure 5.7: Estimated modal participation on the central microphone 5 due to normal incidence noise on the plate. The values are normalised to the participation of mode 1 and plotted in dB. For some peaks the mode shape and natural frequency is given. The notation means that, for example for mode 5 (27 Hz), the plate has 3 *anti-nodes* or local displacement maxima in the $x-$direction and 1 anti-node in the $y-$direction.

Actuator nr.	x-coordinate [m]	y-coordinate [m]
1	0.0	0.0
2	-0.32	0.0
3	0.0	-0.32

Table 5.2: Position of the center of the three actuators on the plate. The actuators are placed on the maxima of the modes 1, 5 and 6 (see also Fig. 5.8) and Fig. 5.9.

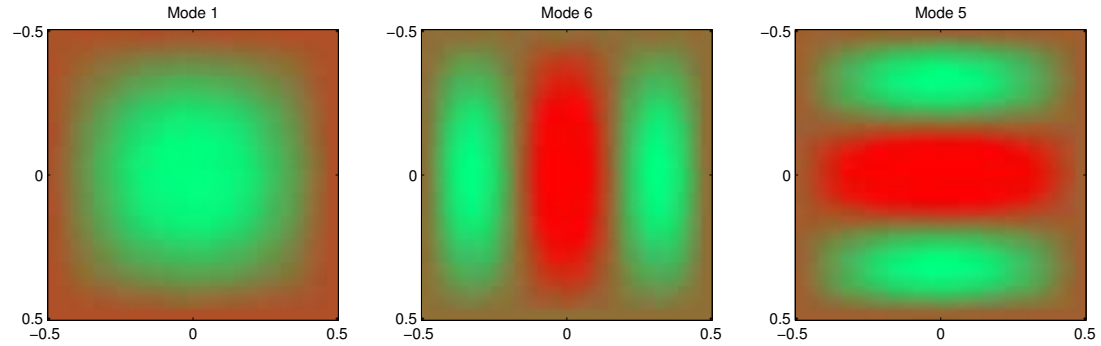

Figure 5.8: Calculated mode shapes that belong to the first three peaks seen in Fig. 5.7. *From left to right*: mode 1 (1,1), mode 5 (3,1) and mode 6 (1,3).

Figure 5.9: Receiver side of the plate with the three piezoelectric actuators attached.

5.2.4 Noise types

For the active noise control measurements and simulations three different noise types are used: random noise, tonal noise (meaning a sinusoidal signal with a single frequency) and a sweep signal.

Random noise

In random noise all frequencies appear stochastically, as during a normal transmission loss measurements (see Chapter 2). This noise type is the most difficult one for successful ANC results, because the predictability of the noise that comes through the plate is low.

Tonal noise

In tonal noise a sinusoidal tone with full predictability is used to test the active noise control system for its maximum performance and reduction. Looking at possible applications as engine isolation for a vehicle we can roughly compare the tonal excitation with the situation of a vehicle with constant (engine) speed.

Sweep signal noise

In sweep signal noise the tonal noise's frequency changes gradually from a lower frequency limit to an upper frequency limit in a certain amount of time. It is used to test if the controller is able to follow the frequency change of the noise and can show if the system is more sensitive for certain frequencies compared to others. The sweep can be compared with the situation of the engine noise of a vehicle that is accelerating. Lower frequency and upper frequency limit as well as the frequency change per time unit can be chosen.

5.3 Simulation set-up

All discussed simulations are preformed in Matlab 7.0 on an HP personal computer (Intel Pentium 4 CPU 2.8 GHz, 1GB RAM) running on Windows XP Professional. The FEM model matrices are imported from MSC/Patran which runs on a Unix-system.

5.3.1 Plate mesh

The mesh of any FE model and thus also our plate should be sufficient fine to be able to describe all vibrations correctly. Aliasing, as it occurs during sampling of a continuous time signal (see Paragraph 3.2), where a too large sampling distance Δt is chosen with respect to the highest frequency components, can also happen spatially: a too large distance between the mesh points will result in a misinterpretation of the vibrations with the highest frequencies. A too small sampling distance however will waste unnecessary computer calculation time.

Using Eq. 2.8 we can calculate the bending wavenumber for a frequency of 800 Hz in the aluminium plate. Using the definition $\lambda_b \equiv 2\pi/k_b$, we come to a wavelength of 0.11 m. A (squared) shell element with size 0.02 m is chosen (see Fig. 5.10), which will be sufficient to describe waves in the aluminium plate up to least 800 Hz. The same goes for steel, where the wavelength at 800 Hz is approximately 0.11 m too.

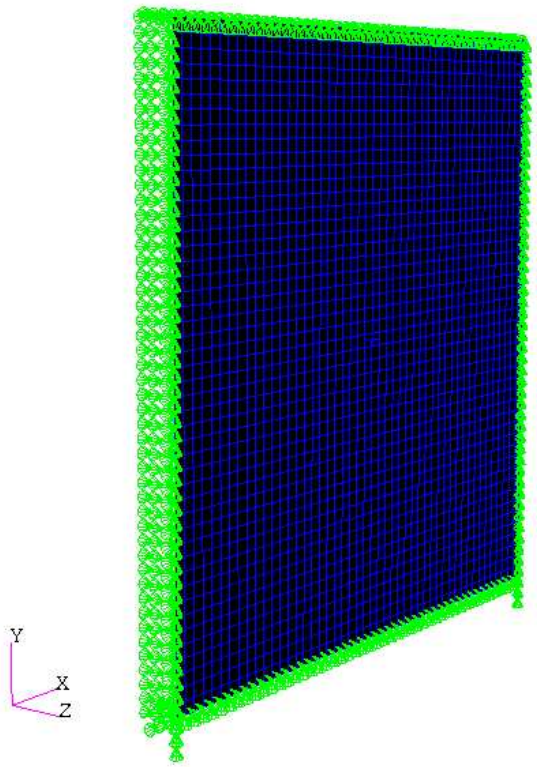

Figure 5.10: Mesh of the plate, plotted in perspective using the programme Patran. The green symbols in the figure represent the simply-supported boundary conditions at the edges of the surface.

5.3.2 Modal analysis

Already discussed in Paragraph 4.2.3 and appendix A we can solve the eigenvalue problem of Eq. 4.22 and obtain the eigenvalues and eigenvectors, which are respectively the mode frequencies and mode shapes of the model. The results can be found in Paragraph 6.2.

Damping

After executing the experimental modal analysis and extracting the natural frequencies, the damping factors of those resonances can be exported by the post-processing software. Using least-squares optimisation, the damping function Eq. 4.18 can be fitted through the modal damping values. From that function the Rayleigh damping factors α_1 and α_2 can

be extracted, which are used in the model throughout for all simulations. Results can be found in Paragraph 6.2.

5.3.3 Actuator simulation

For the investigation of active noise control in transient finite element simulations, chosen is not to concentrate too much on the simulation of the piezoelectric actuator by using a very fine mesh with sandwich piezoelectric layers. Instead, more important is a fast and relatively clear model. However, simply applying a force as actuator on the plate is not enough; the bending effects of the actuators should be taken into account.

As is explained, an actuator will bend due to a voltage difference on the piezoelectric layers and so induce bending to the plate at the actuator area. Transferring this to rotational loads of the FE model (see Eq. 4.9) we can say that there is a moment q on each corner node of the actuator area. This moment can be written out in terms of moments in the x- and y-direction which we can use in the simulation (see Fig. 5.11) (Johnson [35]).

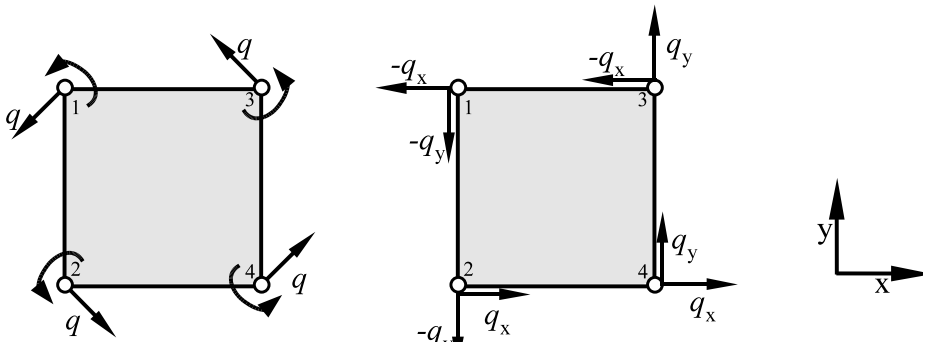

Figure 5.11: *Left Figure*: Moment q is applied on all four corners of the simulated actuator. *Right Figure*: The moment q can be written in terms of q_x and q_y.

The size of each actuator in the model is not chosen to be a single square plate element but two elements, more or less conform the dimension of the real actuators. Positions on the plate are given in Table 5.2. A short extra computer routine inside the simulation algorithm transforms the ANC output channels into the correct moments for each node.[5] Results can be seen in the next chapter.

5.3.4 Transient simulation sample rate

A fundamental setting to be chosen before starting a time-dependent simulation is the time step size Δt (see also Paragraph 4.3). As with the signal processing for active noise

[5] Of course the unit source value of 1 V for real piezo-actuators can not be compared with the unit source value of 1 Nm for the simulated actuator; the last one will have a much higher response. For the ANC algorithm this does not play a role: it will automatically scale down the signal to the actuator appropriately.

control, a consensus has to be made between frequency range on the one side and speed of simulation on the other side. In general it is advised to have a transient simulation sample rate of about 20 times the minimum frequency of interest. Depending on the model and the integration techniques, the simulation is less accurate if using a smaller sample rate factor (MacNeal [38], Ansys [4]). In our case, where the upper frequency for ANC is between 500 and 800 Hz, we choose a simulation sample rate of 10 kHz so Δt will be 0.1 ms. All random and white noise signals used are filtered with a low-pass anti-aliasing FIR filter with 3-dB-point at 1 kHz.

5.3.5 Noise source loads

In Paragraph 4.2.3 the general equation of motion used for finite element simulation can be found as Eq. 4.19. In this equation the right hand side contains the source, which is either a force or a moment that works on a node. Because we are interested in and make use of pressures, we need to convert the pressures to obtain the correct forces for all nodes[6]. The following equation calculates the nodal force in the z-direction for node m. For this calculation each node is is considered to have a surface around it of the size of an element, $S^{(\mathrm{e})}$. The forces in the other directions are considered to be zero.

$$f_z^{(m)} \approx p^{(m)} S^{(\mathrm{e})}, \tag{5.2}$$

where $f_z^{(\mathrm{m})}$ is the nodal force in the z-direction due to the pressure $p^{(m)}$.

5.3.6 Noise incidence types

Normal incidence

For the situation of normal incidence, where plane acoustic waves approach the plate perpendicular, the pressure (and therefore the force) is considered equal over the entire plate. The normal incidence approach is used for some simulations in this thesis using stochastic noise. The source signal is of course anti-aliasing filtered before applying it as pressure on the plate.

Random and field incidence

The random incidence, as it appears in a diffuse sound field, is a more complicated situation. It can be seen as *the summation of infinite uncorrelated plane waves coming from all directions* (see Rafaely [49] and Jacobsen [34]):

$$p_{\mathrm{A}}(t) = \lim_{J\to\infty} \frac{1}{\sqrt{J}} \sum_{j=1}^{J} p_j \left(t - \frac{r_{j,A}}{c_0} \right), \tag{5.3}$$

[6] In this conversion the local movements of the plate are neglected.

where $p_{\mathrm{A}}(t)$ is the pressure signal in a point A inside the sound field, J is the number of plane waves, $p_j(t)$ is the pressure of a plane wave j and $r_{j,A}$ is the distance from the plane wave's source point[7] to the point A.

In trying to simulate a diffuse sound field one should not make the easy mistake of generating separate random source signals for all node on the plate. This way the important *spatial correlation* of the sound field is not considered. A more appropriate way of simulating a sound field which resembles a diffuse field is by using a finite ($J < \infty$) number of uncorrelated plane wave sources.

In paragraph 4.4.2 a technique with a matrix $\boldsymbol{Q}$ which includes amplitude factors at certain time delays is introduced to calculate the time domain radiation from the plate to a point in the air. In this paragraph we will use that technique again, with the difference that now we will make use of plane waves that come from imaginary source point locations and are travelling towards the plate's nodes. We therefore need as many matrices as we will choose source points.

Again, most important in the approach is the determination of the time delays for every node. For a plane wave p_j the angles θ and ϕ in which the wave approaches the plate are randomly chosen (see Fig 5.12). Only condition is that the plane waves travels from the negative z-area towards the plate. The two randomly chosen angles are responsible for the variable arriving time of the wave at the different nodes.

Let us consider a point m somewhere on the plate, coordinates are $(x^{(\mathrm{m})}, y^{(\mathrm{m})})$. The plane wave p_j with random pressure signal approaches the plate with the chosen angles θ and φ and it falls in at the plate's origin at a certain time t_0. Projected on the $(x, y)-$plane, the wave front will have a *phase velocity* of c_{xy} (Berkhout [10]):

$$c_{xy} = \frac{c_0}{\sin\theta}. \tag{5.4}$$

In this $(x, y)-$plane the wave front will need a time $\Delta t^{(\mathrm{m})}$ to travel from the origin to node m, which can be calculated using the phase velocities in the $x-$ and $y-$direction:

$$\Delta t^{(\mathrm{m})} = \frac{x^{(\mathrm{m})}}{c_x} + \frac{y^{(\mathrm{m})}}{c_y} = \frac{(x\cos\varphi + y\sin\varphi)}{c_{xy}} = \frac{\sin\theta}{c_0}(x\cos\varphi + y\sin\varphi) \tag{5.5}$$

Having thus obtained a continuous time delay $\Delta t^{(\mathrm{m})}$ for this combination of plane wave and node, we now have to transform it to the discrete time by using linear interpolation as in Eq. 4.37. The transform of continuous pressure $p(t)$ at node m due to plane wave j into discrete pressure $p[n]$ will be:

[7] Actually, a plane wave does not have a source point but a source area. In this thesis the source point of a plane wave is considered to be that point in the source area for which the plane wave later on coincides with the origin $(x, y, z) = (0, 0, 0)$, the center of the plate.

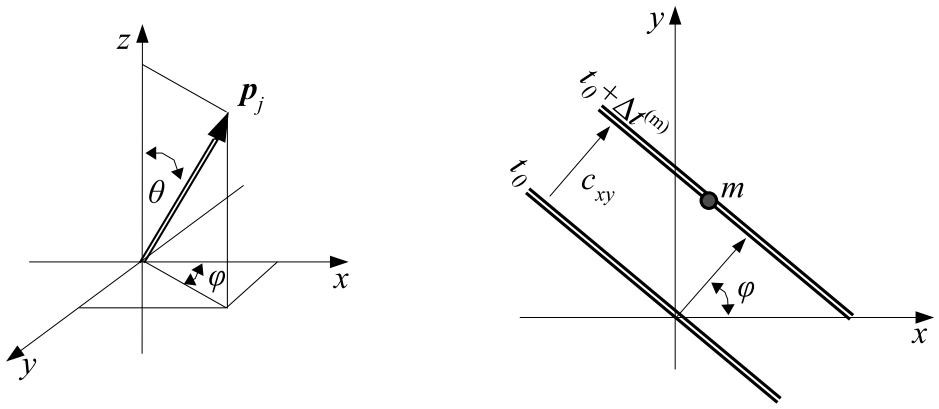

Figure 5.12: *Left Figure*: The double arrow denotes the direction of a plane wave p_j at the moment it crosses the origin (0,0,0); θ is the angle it makes with the z-axis and φ is the angle between the $x-$axis and the projection of the double arrow in the $(x, y)-$plane. *Right Figure*: In the $(x, y)-$plane the plane wave travels with a (phase-)velocity of c_{xy}. The time of arrival at the origin $(x, y) = (0, 0)$ is t_0 and after $\Delta t^{(\mathrm{m})}$ seconds it arrives at node m.

$$p_j^{(\mathrm{m})}\left(t - \Delta t_j^{(\mathrm{m})}\right) \longrightarrow \gamma_1 p_j\left[n - \zeta^{(\mathrm{m})}\right] + \gamma_2 p_j\left[n - \zeta^{(\mathrm{m})} - 1\right], \tag{5.6}$$

with for ζ, the time delay integer, again the following floor function:

$$\zeta^{(\mathrm{m})} = \left\lfloor \frac{\Delta t_j^{(\mathrm{m})}}{\Delta t} \right\rfloor$$

and the $\gamma-$factors are calculated as in Eq. 4.38.

If we do this for every point on the plate for which we want to determine the pressure, we can create a matrix $\boldsymbol{Q}_j$:

$$\boldsymbol{Q}_j = \begin{bmatrix} 0 & \cdots & 0 & \gamma_1^{(1)} & \gamma_2^{(1)} & 0 & \cdots & 0 & 0 \\ \vdots & & \vdots & \vdots & \vdots & \vdots & & \vdots & \\ 0 & \cdots & \gamma_1^{(\mathrm{m})} & \gamma_2^{(\mathrm{m})} & 0 & 0 & \cdots & 0 & 0 \\ \vdots & & \vdots & \vdots & \vdots & \vdots & & \vdots & \vdots \\ 0 & \cdots & 0 & 0 & 0 & 0 & \cdots & \gamma_1^{(M)} & \gamma_2^{(M)} \end{bmatrix}.$$

which we have to multiply with the a random anti-aliased source signal $\boldsymbol{p}_j[n]$. Result is a vector with the load pressures for all M nodes considered at time n due to plane wave j:

$$\boldsymbol{p}_j^{(\mathrm{m})}[n] = \boldsymbol{Q}_j \boldsymbol{p}_j[n]. \tag{5.7}$$

To reduce the size of $\boldsymbol{Q}_j$ we can remove the zeros on the left side of the matrix column-

wise. This is the same as bringing the plane wave sources so close to the plate, that one of the plate corners (in the case below it is node m) coincides with the source plane of the wave:

$$\boldsymbol{Q}_j = \begin{bmatrix} 0 & \gamma_1^{(1)} & \gamma_2^{(1)} & 0 & \cdots & 0 & 0 \\ \vdots & \vdots & \vdots & \vdots & & \vdots & \\ \gamma_1^{(\mathrm{m})} & \gamma_2^{(\mathrm{m})} & 0 & 0 & \cdots & 0 & 0 \\ \vdots & \vdots & \vdots & \vdots & & \vdots & \vdots \\ 0 & 0 & 0 & 0 & \cdots & \gamma_1^{(M)} & \gamma_2^{(M)} \end{bmatrix}.$$

This node pressure calculation has to be done for all J simulated plane waves and the J obtained pressure vectors can be summed using the following equation, which can be seen as a discrete version of Eq. 5.3:

$$\boldsymbol{p}^{(\mathrm{m})}[n] = \frac{1}{\sqrt{J}} \sum_{j=1}^{J} \boldsymbol{p}_j^{(\mathrm{m})}[n]. \tag{5.8}$$

To speed up the calculation explained above, it can be considered to reduce the number of points on the plate for which the pressure is calculated. The dense plate mesh is necessary for bending wave calculations (see Paragraph 5.3.1). Acoustic waves in air typically have much longer wave lengths and can have a more coarse mesh. If decided to reduce the number of points for the random incidence calculation, the force load still needs to be calculated for every node. This can for example be done with an 2-dimensional interpolation procedure.

The thus obtained pressure signals at the plate's nodes can be either calculated during or before the actual transient time simulation. The first approach will make the transient simulation recursion a bit slower. The second one requires the simulation time length beforehand and the calculated pressure signals need to be stored. For the simulations in this thesis the first solution is therefore chosen.

In paragraph 2.2.1 we have discussed the field-incidence rule, which prefers a limit of 78^o for the incident plane waves in diffuse field calculations. This limit will therefore be set for the angle θ in the simulations.

5.3.7 Transmission Loss data

Having determined the sound field on the incident side of the plate according to the description above, we can calculate the average pressure on this side and use as input for the transmission loss calculation.

On the output side the average pressure is determined by using the five mentioned microphone positions (see Table 5.1). However, these five microphones are further away from

the plate than the intensity microphone in the experiments and do not cover the entire radiating hemisphere of the plate. Therefore a correction is needed to obtain accurate transmission loss results (see also Paragraph 6.3). The final transmission loss equations for the simulations will look as follows:

$$R = 10 \log \left(\frac{E\{p_{\text{inc}}^2\}}{E\{p_{\text{rad}}^2\}} \right) - \text{correction} \qquad \text{dB}. \tag{5.9}$$

5.4 FE implementation of ANC algorithm

In Paragraph 4.3, the equation of motion is transformed in such a way that the nodal acceleration at the next point in time can be calculated:

$$\ddot{\boldsymbol{u}}_{n+1} = \boldsymbol{\Gamma}_1^{-1} \Big(\boldsymbol{f}_{\text{ext},n+1} - \boldsymbol{K} \left(\boldsymbol{u}_n + \Delta t \dot{\boldsymbol{u}}_n \right) + \boldsymbol{\Gamma}_2 \ddot{\boldsymbol{u}}_n \Big). \tag{5.10}$$

with

$$\boldsymbol{\Gamma}_1 = \boldsymbol{M} + \frac{1}{2} \Delta t \boldsymbol{B} + \frac{1}{4} \left(\Delta t \right)^2 \boldsymbol{K} \qquad \text{and} \qquad \boldsymbol{\Gamma}_2 = -\frac{1}{4} \Delta t (2\boldsymbol{B} + \Delta t \boldsymbol{K})$$

Calculating the matrices M, B and K can be done beforehand and the same goes for $\boldsymbol{\Gamma}_1$, $\boldsymbol{\Gamma}_2$ and $\boldsymbol{\Gamma}_1^{-1}$.

Having calculated $\ddot{\boldsymbol{u}}_{n+1}$, we use the following equations to calculate the velocity and displacement for time $n+1$:

$$\begin{aligned} \dot{\boldsymbol{u}}_{n+1} &= \dot{\boldsymbol{u}}_n + \tfrac{1}{2} \Delta t \left(\ddot{\boldsymbol{u}}_n + \ddot{\boldsymbol{u}}_{n+1} \right) \\ \boldsymbol{u}_{n+1} &= \boldsymbol{u}_n + \Delta t \, \dot{\boldsymbol{u}}_n + \tfrac{1}{4} \left(\Delta t \right)^2 \left(\ddot{\boldsymbol{u}}_n + \ddot{\boldsymbol{u}}_{n+1} \right). \end{aligned} \tag{5.11}$$

Also, the formula to calculate the radiation from the structure to a receiver point A was constructed and is as follows:

$$p_{\text{A}}[n] = \sum^{\text{diag}} \left(\boldsymbol{Q}_{\text{A}} \ddot{\boldsymbol{U}}[n] \right). \tag{5.12}$$

Determining matrix $\boldsymbol{Q}_{\text{A}}$ can be done beforehand too and has to be done for every virtual microphone position. The result of the equation, a pressure sample $p_{\text{A}}[n]$, is added on top of the buffer $\boldsymbol{p}_{\text{A}}[n]$ which is the discrete pressure signal in point A.

Downsampling

For transient finite element simulations the discrete time interval $\Delta t = f_{\text{s}}^{-1}$ has to be set and it was already stated that a sample rate of at least ten times the highest frequency of interest should be chosen (Ansys [4]). The active noise control algorithm, however, does not need such a high oversampling rate. It would cost unnecessary calculation time and

buffers would need to be much longer to have the same required time span. Consensus will be a factor 2.5 times the highest frequency of interest. Decimating the 2.5 kHz signal, it means that that every fourth time during the simulation loop the system identification algorithm or ANC algorithm is executed.

The FE simulation result with its high sample rate probably contains components with a frequency higher than the bandwidth meant for active noise control. This means that we can not simply extract every forth sample of the simulation but need to use an anti-aliasing filter to prevent the algorithm from interpreting false frequencies. With this filter which we will call $\boldsymbol{h}_{\mathrm{UD}}$ (U-D stands for Up-Downsampling) we now know that the (pressure) signal does not contain strong frequency components above the Nyquist frequency and can reduce the sample rate for ANC or system identification purpose by taking every fourth sample. Now we have two different discrete time variables: the *downsampled* version we keep calling $[n]$ and the high-frequency FE simulation time version we will call $[n_{\mathrm{FEM}}]$, with $\Delta t = 4\Delta t_{\mathrm{FEM}}$.

With this separation between FE sampling time and ANC sampling time we can say for the anti-aliasing filter $\boldsymbol{h}_{\mathrm{UD}}$ that it only needs to be executed every fourth time as well. Schematically it can be seen in figure 5.13 and the equation for applying the filter will be[8]:

$$p_{\mathrm{A}}[n] = \boldsymbol{h}_{\mathrm{UD}}{}^{\mathrm{T}}\boldsymbol{p}_{\mathrm{A}}[n_{\mathrm{FEM}}] \tag{5.13}$$

with for L_{UD} the length of the anti-aliasing filter.

Upsampling

The output of the system identification or ANC algorithm, $y[n]$, is usually a voltage that is fed to the secondary source actuator. Where the input signal for the algorithm needed to be downsampled, the output signal needs to be *upsampled* to have a smooth output signal available for the secondary source(s) during FE simulation. If not, the voltage on the secondary source would be the same during four samples and then suddenly change to the next value like a block function. The upsampling calculation that smooths this step-function needs to be done every step in time $[n]$ and the same anti-aliasing filter $\boldsymbol{h}_{\mathrm{UD}}$ can be used:

$$y_{\mathrm{filt}}[n_{\mathrm{FEM}}] = \boldsymbol{h}_{\mathrm{UD}}{}^{\mathrm{T}}\boldsymbol{y}[n_{\mathrm{FEM}}]. \tag{5.14}$$

Here $\boldsymbol{y}[n_{\mathrm{FEM}}]$ is a (high sample rate) buffer which is updated during the FE loop with the last output of the ANC algorithm: $y[n]$. This means that in our case four samples are the same before a new ANC output is calculated and inserted.

[8] In this thesis a FIR filter is used, but other filters, e.g. IIR, are also possible.

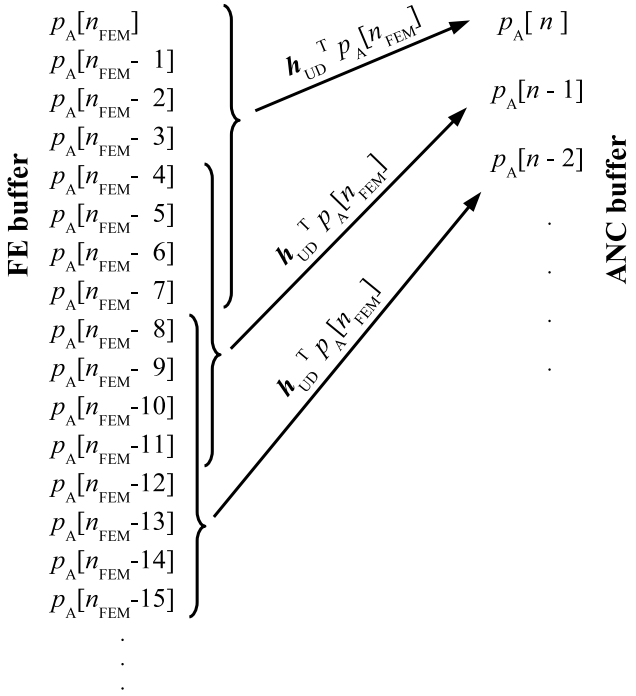

Figure 5.13: Schematic representation of the two pressure signal buffers and the anti-aliasing procedure to reduce the sample rate for ANC or system identification purpose. In this example the anti-aliasing filter h_{UD} has length $L_{\mathrm{UD}} = 7$.

5.4.1 Single channel implementation

Although a system identification with only a single delta pulse might be possible for our FE model, we will start with discussing the LMS system identification with random broadband noise in this paragraph, denoted with SYSID. Next, we will discuss the solving algorithm SOLVE that finds a solution for the equation of motion as discussed in the previous chapter. This algorithm is used for both the system identification and the active noise control algorithm. This ANC algorithm is called FxLMS and will be discussed in the last part of this paragraph.

Single channel system identification algorithm (SYSID1)

As we have seen in paragraph 3.3.1, the system identification tries to estimate the plant's impulse response $\boldsymbol{g}$ of the FE model. It starts with generating a random secondary source sample $y[n]$ which is put on top of the buffer $\boldsymbol{y}[n]$. This new sample is used as input for the SOLVE algorithm (see next subparagraph). The output of this SOLVE algorithm is the simulated signal at the error sensor position, the (high sample rate) buffer $\boldsymbol{d}[n_{\mathrm{FEM}}]$.

This signal has to be downsampled as in Eq. 5.13 and the result, sample $d[n]$, is used to calculate the error $e[n]$. This $e[n]$ equals the difference between the real plant output $d[n]$ and the output $\hat{d}[n]$ of the adaptive estimated system $\hat{\boldsymbol{g}}$, using the same input signal $\boldsymbol{y}[n]$:

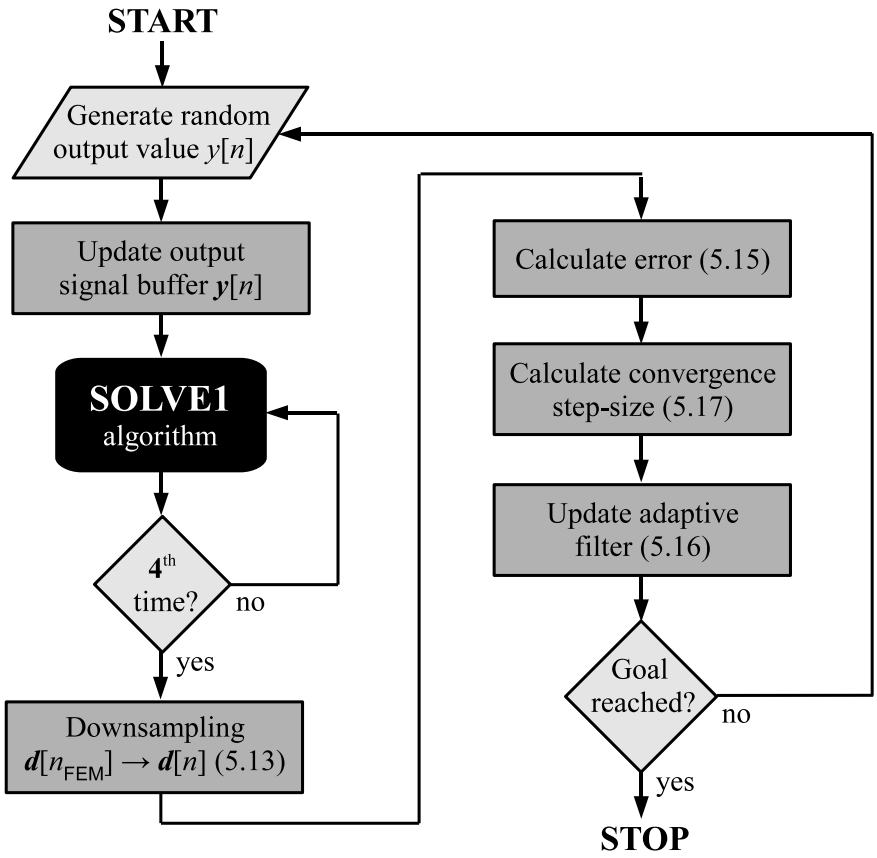

Figure 5.14: Flow chart of the SYSID1 algorithm for single channel plant estimation. The numbers in the tasks refer to the equations in the text. Other step orders inside in the algorithm are possible.

$$e[n] = d[n] - \hat{d}[n] = d[n] - \hat{\boldsymbol{g}}_n^{\mathrm{T}} \boldsymbol{y}[n]. \tag{5.15}$$

The new error sample is used to update the estimated impulse response:

$$\hat{\boldsymbol{g}}_{n+1} = \hat{\boldsymbol{g}}_n + 2\mu \boldsymbol{y}[n] e[n] \tag{5.16}$$

with for the convergence step-size μ:

$$\mu = \frac{\mu_0}{\boldsymbol{y}^{\mathrm{T}}[n]\boldsymbol{y}[n]}, \qquad \mu_0 \leq 1. \tag{5.17}$$

The entire procedure as a *flow chart* can be seen in Fig. 5.14. As soon as a certain goal is reached, for example after a preset number of iterations or as soon as the error $e[n]$ is smaller than some predetermined value, the procedure stops. If not, it starts from the top again using the existing buffers and filter values.

Single channel solving algorithm (SOLVE1)

The SOLVE1 algorithm starts with taking its input value $y[n]$ and upsample it to the value $y[n_{\text{FEM}}]$ (Eq. 5.14). This value is entered in the load vector $\boldsymbol{f}_{\text{ext},n+1}$ and now Eq. 5.10, meaning the new acceleration, can be solved. Subsequently, using the acceleration we can apply Eq. 5.11 to derive the new velocity and displacement. Finally the acceleration history is used to calculate the radiated noise at the receiver position (using Eq. 5.12) and this result is added to its buffer (see Fig 5.15).

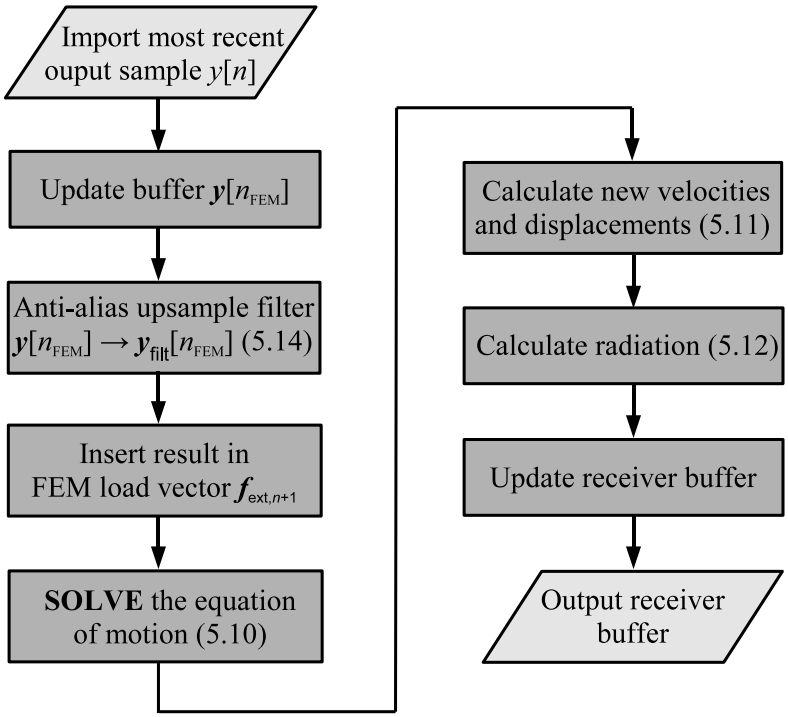

Figure 5.15: Flow chart of the single channel SOLVE1 algorithm.

Single channel filtered-reference algorithm (FxLMS1)

Once the plant is properly identified with the impulse response $\hat{\boldsymbol{g}}$, we can initiate the ANC algorithm. This is done by setting an initiating value for μ_0 and β and starting the noise source procedure. A short summary of the equations from paragraph 3.4.1 that are used is given below and the flow chart can be seen in Fig. 5.16.

First, the reference value $x[n]$ is read and inserted on top of the buffer $\boldsymbol{x}[n]$. Then, using the estimated plant $\hat{\boldsymbol{g}}$, the filtered-reference sample $r[n]$ is calculated:

$$r[n] = \hat{\boldsymbol{g}}^{\mathrm{T}} \boldsymbol{x}[n] \tag{5.18}$$

and is inserted on top of the buffer $\boldsymbol{r}[n]$. With this updated filtered-reference signal, the convergence step-size μ is calculated as follows:

$$\mu = \frac{\mu_0}{\boldsymbol{r}[n]^{\mathrm{T}} \boldsymbol{r}[n]}, \qquad 0 < \mu_0 \leq 1. \tag{5.19}$$

Now the adaptive filter $\boldsymbol{w}_n$, most important in the algorithm, can be updated. It starts with only zeros at the beginning of the procedure and is updated as follows:

$$\boldsymbol{w}_{n+1} = (1 - 2\mu\beta)\, \boldsymbol{w}_n - 2\mu \boldsymbol{r}[n] e[n]. \tag{5.20}$$

With this new filter $\boldsymbol{w}$ we can calculate the next output sample $y[n]$, using the Eq. 5.21:

$$y[n] = \boldsymbol{w}_n^{\mathrm{T}} \boldsymbol{x}[n]. \tag{5.21}$$

This output sample is used as input of the SOLVE1 procedure, in our case four times due to the 1:4 ratio of the sample rates. Finally, after radiation calculation as in Eq. 5.12 and downsampling, we can update the error buffer $\boldsymbol{e}[n]$ with the new value and start again at the beginning of the procedure.

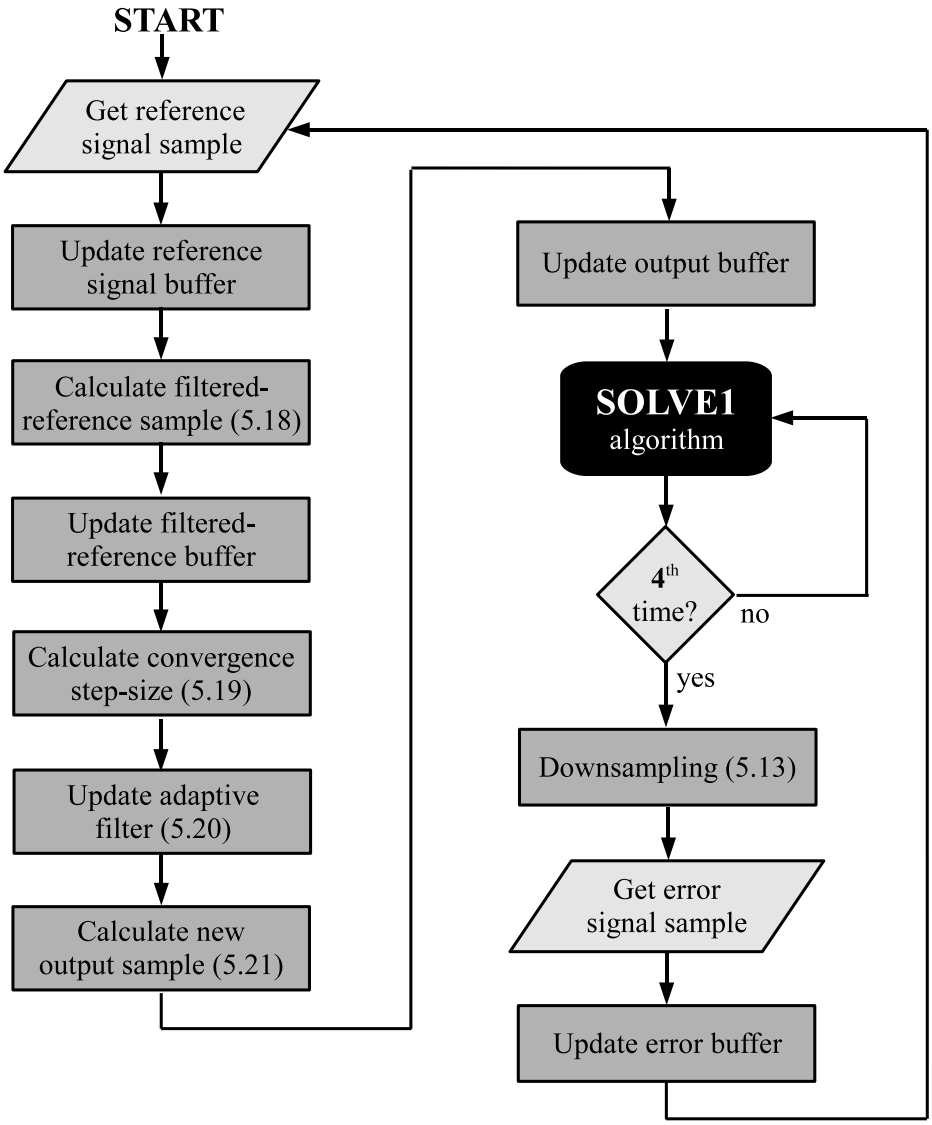

Figure 5.16: Flow chart of the single channel ANC algorithm FxLMS1.

5.4.2 Multichannel implementation

As we have seen in paragraph 3.4.2, multichannel active noise control requires a few more steps than single-channel control. The FE model however does not change, and solving the equation of motion therefore remains the same. Calculating the radiation with Eq. 5.12 now has to be done for more then one receiver points and a few extra steps have to be added to the ANC algorithm.

Multichannel system identification (SYSID2)

As discussed in paragraph 3.4.2, the update equation for estimating the plant responses with multiple channels can be written as a matrix multiplication:

$$\hat{\boldsymbol{G}}_{k,n+1} = \hat{\boldsymbol{G}}_{k,n} + 2\mu \boldsymbol{y}_k[n]\boldsymbol{E}[n]. \tag{5.22}$$

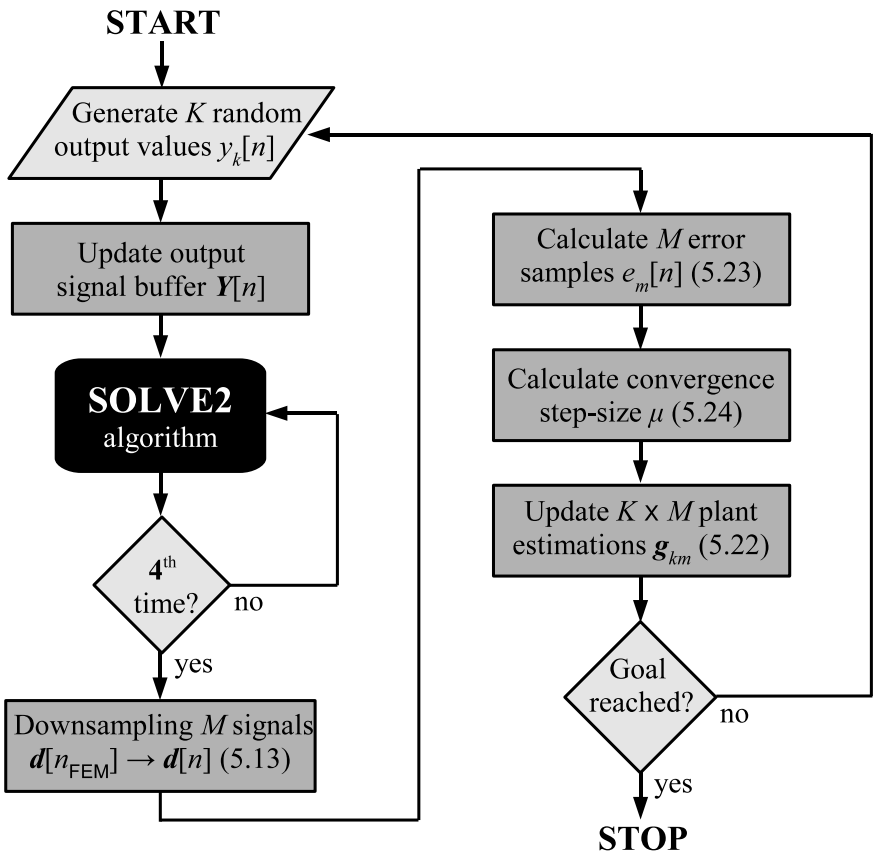

Figure 5.17: Flow chart of the multichannel system identification algorithm.

The single channel SYSID1 flow-chart needs a few small changes when having more then one channels. For example, $\boldsymbol{y}[n]$ now changes to K different output channels $\boldsymbol{y}_k[n]$ and the error calculation now has to be done M times using the following equation:

$$e_m[n] = d_m[n] - \sum_{k=1}^{K} \hat{\boldsymbol{g}}_{km}^{\mathrm{T}} \boldsymbol{y}_k[n]. \tag{5.23}$$

The convergence step-size μ is calculated as follows, but can also be calculated before starting the estimation algorithm:

$$\mu = \frac{\mu_0}{\max_k(\boldsymbol{y}_k^{\mathrm{T}} \boldsymbol{y}_k)}, \quad 0 < \mu_0 \leq 1. \tag{5.24}$$

The new flow-chart can be seen in Fig. 5.17.

Multichannel solving algorithm (SOLVE2)

As in the previous paragraph but now for K output channels, the SOLVE2 algorithm starts with upsampling $\boldsymbol{y}_k[n]$ to the high frequency (but anti-alias filtered) signal $\boldsymbol{y}_{k,\mathrm{filt}}[n_{\mathrm{FEM}}]$. The latest values of these buffer signals will be entered into the load vector $\boldsymbol{f}_{\mathrm{ext},n+1}$ of the equation of motion, which will be solved normally, independent from the number of channels (see Fig. 5.18).

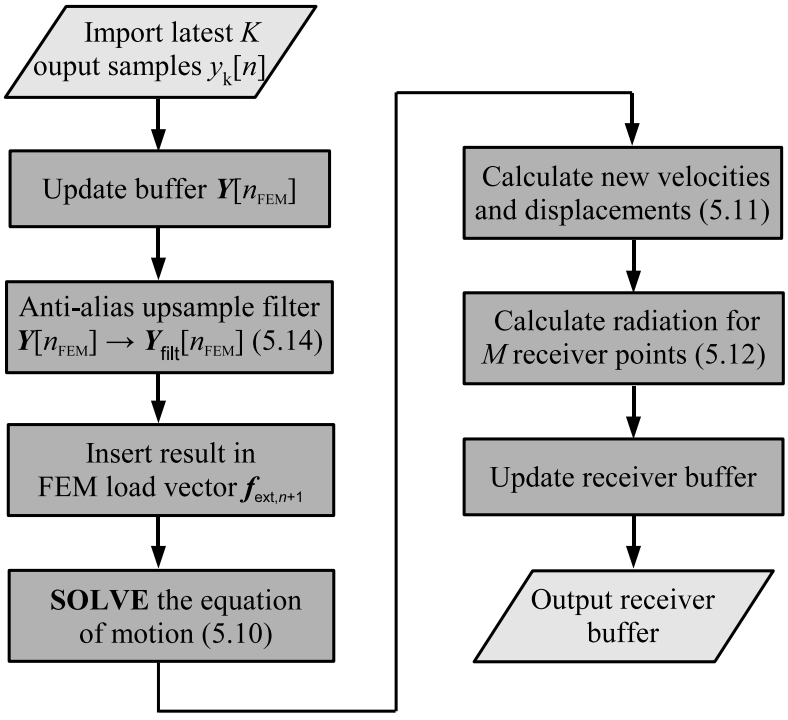

Figure 5.18: Flow chart of the multichannel SOLVE2 algorithm.

In paragraph 4.4.1 we have seen how to build a matrix $\boldsymbol{Q}$ to calculate the radiation in a certain point away from the plate using the nodes' acceleration. When dealing with M error sensors, we thus need to create M different matrices $\boldsymbol{Q}_m$ before starting the system identification. The radiation calculating of Eq. 5.12 needs to be executed M times during the solve procedure.

Multichannel filtered-reference algorithm (FxLMS2)

The procedure for multichannel active noise control is more or less given in paragraph 3.4.2 and can be seen as a flow-chart in Fig. 5.19. We can start the procedure by retrieving the J different reference sensor samples $x_j[n]$. Put into the buffer $\boldsymbol{X}[n]$, we can multiply it with the set of (estimated) impulse responses $\hat{\boldsymbol{G}}$:

$$\boldsymbol{R}_n = \hat{\boldsymbol{G}}\boldsymbol{X}[n]. \tag{5.25}$$

This equation returns $\boldsymbol{R}_n$, a matrix with the latest filtered-reference values. They will be put on top in the filtered-reference buffer matrix $\boldsymbol{R}$ (see also Eq. 3.51 and Eq. 3.52). Having the M error samples $e_m[n]$ available too, we can now execute the update equation to improve the $J \times K$ adaptive filters $\boldsymbol{w}_{jk}$:

$$\boldsymbol{w}_{jk,n+1} = (1 - 2\mu\beta)\boldsymbol{w}_{jk,n} - 2\mu \sum_{m=1}^{M} \boldsymbol{r}_{jkm}[n]e_m[n]. \tag{5.26}$$

The convergence factor μ can be calculated beforehand or during every step, and is calculated as follows:

$$\mu = \frac{\mu_0}{\max_{jkm}(\boldsymbol{r}_{jkm}^{\mathrm{T}}\boldsymbol{r}_{jkm})}, \quad 0 < \mu_0 \leq 1. \tag{5.27}$$

Now we can calculate the K new output samples that will be send to the SOLVE2 procedure, using the following equation:

$$y_k[n] = \sum_{j=1}^{J} \boldsymbol{w}_{jk,n}^{\mathrm{T}}\boldsymbol{x}_k[n]. \tag{5.28}$$

Again, the solving algorithm solves the FE equation of motion four times using the output loads calculated above. After that, the high sample rate error data is downsampled again, the new error samples $e_m[n+1]$ are calculated and the procedure can start from the top again.

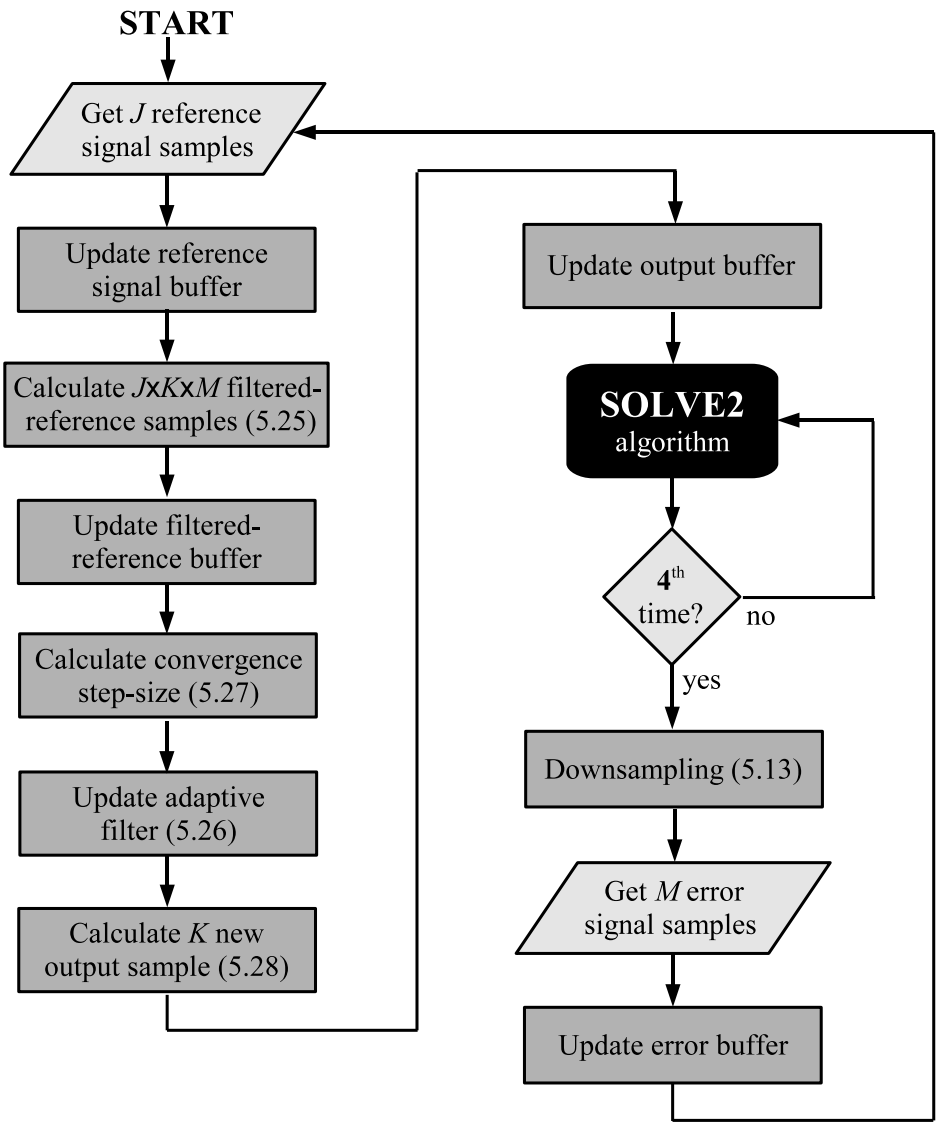

Figure 5.19: Flow chart of the multichannel ANC algorithm FxLMS2.

5.5 Conclusions

The implementation of theories and ideas into computer code takes time and effort. The natural phenomenon of noise reflection as it occurs inside a reverberation room needs to be simplified first and assumptions are made. Next, equations can be developed that describe this simplified model. After that, the equations need to be discretised and finitised, meaning that continuous operations like integrals and not-a-number terms like infinity disappear. Finally the resulting equations can be transformed into computer language, which is assumed to still give a good representation of reality.

This chapter consisted of to parts: experiment and simulation. Both those parts contain two important topics: transmission loss and active noise control. For the experimental investigations only a moderate amount of preparation was necessary, mainly for the ANC measurements set-up. The FE simulations however have been built up from almost a blank page; only the three matrices $\boldsymbol{M}$, $\boldsymbol{B}$ and $\boldsymbol{K}$ could be generated more or less automatically using commercial computer software.

During the whole process of building a simulation program three topics need not be forgotten: aliasing, calculation speed and reality representation. The first one, aliasing, can appear every time a signal is discretised or downsampled and measures are taken by multiplying the buffered signal with a pre-created low-pass filter. The second aspect, the calculation speed, is of constant concern during the creation of a simulation model. In all decisions about how to implement an equation or what to do with the data the developer should ask himself: “Is this the fastest, least memory taken approach? Can it be more efficient?” The third aspect should always be in a simulator’s mind: “Does this model represent reality?” By simplifying and making assumptions, one should not loose sight of the fact that the simulation should act as a representable substitute of the measurement.

Chapter 6

Experiment and Simulation Results

6.1 Introduction

After an extensive introduction in Chapter 2 to 4 and a detailed description of how the experiments and simulations should be carried out in Chapter 5, leaves this chapter to present, compare and interpret the results.

The first part of this chapter shows us the results of the analytical, the numerical and the experimental modal analysis. The results are listed next to each other for easy comparison and in the appendix all experimentally found mode shapes are shown graphically.

In the second part the (passive) transmission loss measurements are presented and briefly compared to some of the analytically obtained values. Besides that, also the finite element simulations without active control are shown.

The third and last part of this chapter is reserved for all active noise control results, both for the experiments as well as the simulations.

6.2 Modal analysis

As explained in the previous paragraph a modal analysis of both the experimental set-up as well as the numerical model is executed for the 1 mm thick aluminium plate. These results are compared with the analytical modes taken from the theory in Chapter 2. Ideally the three would return the same results; practically it will show that not every experimentally found node can be matched with a numerical one.

Eq. 2.27 shows how the resonance modes of a simply supported plate without actuators can be calculated analytically. Using this equation, 23 modes can be found between 0 and

100 Hz. The results are sorted to the frequency and can be found in the two most left columns of Table 6.1. The first column gives the mode shapes, written in the form (i_x, i_y) where i_x means the number of anti-nodes or local displacement maxima in the $x-$direction and i_y in the $y-$direction of the plate (see also Fig. 5.8). The second column contains the analytically calculated frequencies that belong to those mode shapes.

The FE modal analysis also returned a list of 23 modes and the modes were found to match very well with the analytical result. The corresponding natural frequencies can be found in the third column of the table.

All mode shapes that were found with the experimental modal analysis are shown in Appendix E. Not every mode is clearly identifiable as a pure symmetrical mode as is with the analytical and FE approach. Nevertheless, seven mode shapes have been identified and placed next to the other results in the table, together with their damping factors. The modes of which the shape could not be identified as a clear (i_x, i_y) mode are listed in the lower part of the table.

Looking at the experimental mode shapes of the appendix, it seems that the upper half of the plate behaves slightly different than the lower half. Although it is tried to fix the plate into the boundary with the same force for every screw, this anomaly is probably due to small boundary condition differences.

Another cause for some unidentified mode shapes can be the almost-square shape of the plate. Theoretically, the frequencies modes like (2,3) and (3,2) are very close to each other if the plate is near-squared and the frequency difference can be calculated. Practically, every mode shape does not have a fixed exact frequency for which it vibrates, but will have a frequency span. For example, the experimentally found mode (3,2) will have a maximum response at 36.56 Hz, but will also respond to a load with, say, 37.5 Hz. This means that if two modes exist close to each other, they will interfere and experimentally the two peaks cannot be clearly identified and separated. The lowest mode (5.46 Hz) does not have other resonances close by and it is not clear why this specific resonance has not been found.

To investigate a possible influence of the accelerometers on the modal behaviour of the plate, another simulation has been executed in which seven point masses of $2.0 \cdot 10^{-3}$ kg were added to the nodes closest to the positions of the accelerometers. Table 6.2 shows the results. It shows that the relative frequency change due to the added masses stays below 1% for the resonances below 100 Hz.

Mode Shape	**Analytical Freq.** [Hz]	**Sim. Freq.** [Hz]	**Measured Freq.** [Hz]	**Damping factor** [10^{-2}]
(1,1)	5.46	5.46	–	–
(2,1)	13.49	13.48	15.15	1.9540
(1,2)	13.83	13.83	–	–
(2,2)	21.86	21.84	20.20	1.8227
(3,1)	26.86	26.85	–	–
(1,3)	27.78	27.77	–	–
(3,2)	35.23	35.20	36.56	0.8365
(2,3)	35.80	35.78	–	–
(4,1)	45.58	45.56	–	–
(1,4)	47.31	47.28	–	–
(3,3)	49.17	49.12	50.51	0.6043
(4,2)	53.95	53.90	52.37	1.2546
(2,4)	55.33	55.28	–	–
(4,3)	67.90	67.79	–	–
(3,4)	68.70	68.59	–	–
(5,1)	69.65	69.61	–	–
(1,5)	72.41	72.36	–	–
(5,2)	78.02	77.93	–	–
(2,5)	80.43	80.34	–	–
(4,4)	87.42	87.23	90.42	0.5843
(5,3)	91.97	91.79	–	–
(3,5)	93.81	93.63	96.33	0.7707
(6,1)	99.07	98.99	–	–
–	–	–	44.49	1.3430
–	–	–	55.45	0.3107
–	–	–	59.49	0.8061
–	–	–	75.73	0.8653
–	–	–	84.11	0.5558
–	–	–	86.71	0.7644

Table 6.1: Result of the modal analysis. The first two columns contain the mode shape and the frequency of the analytical modal analysis. The third column contains the natural frequencies found with the FE simulation method. The last two columns contain the frequency and damping ratio of the experimental results. The lower part of the table contains the experimentally found modes that can not be classified as one of the calculated results.

Mode sh.	**Freq. [Hz]** *without acc.*	**Freq. [Hz]** *with acc.*	**Diff.** [%]
(1,1)	5.46	5.44	0.37
(2,1)	13.48	13.43	0.37
(1,2)	13.83	13.79	0.29
(2,2)	21.84	21.78	0.28
(3,1)	26.85	26.69	0.60
(1,3)	27.77	27.62	0.54
⋮	⋮	⋮	⋮
(3,3)	49.12	48.74	0.78
⋮	⋮	⋮	⋮
(3,5)	93.63	93.03	0.65
(6,1)	98.99	98.78	0.21

Table 6.2: Comparison between the simulated modal frequencies without and with accelerometer masses on the plate.

Damping factors

The modal damping factors found during post-processing of the experimental data are plotted to the frequency as black dots in Fig. 6.1. The polynomial damping function $\eta(f)$ (see Eq. 4.18) that best fits the data points is plotted in blue. The obtained damping factors are used to create the damping matrix $\boldsymbol{B}$ and are as follows:

$$\begin{aligned} \alpha_1 &= 3.93 \\ \alpha_2 &= 1.29 \cdot 10^{-5}. \end{aligned}$$

6.3 Passive transmission loss

6.3.1 Experiments

Using the set-up explained in Paragraph 5.2.1, the transmission loss of the aluminium plate is determined by scanning the intensity over the output surface. The result, which is 1/3-octave band based, can be seen as the red line in Fig. 6.2.

Seen from the five error microphones (positions are given in Tab. 5.1), we can calculate the average intensity at those positions. This intensity is, of course, lower than the measured intensity close to the plate and this results in a higher transmission loss line (blue: narrowband, black: 1/3-octave bands).

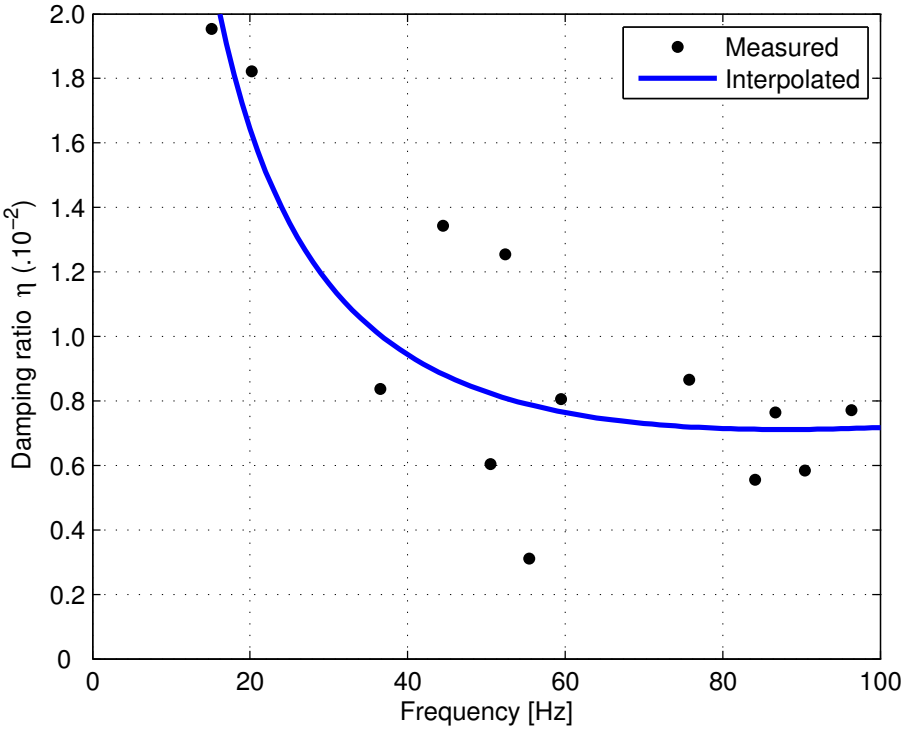

Figure 6.1: Measured damping ratio (black dots) and interpolated values (blue line).

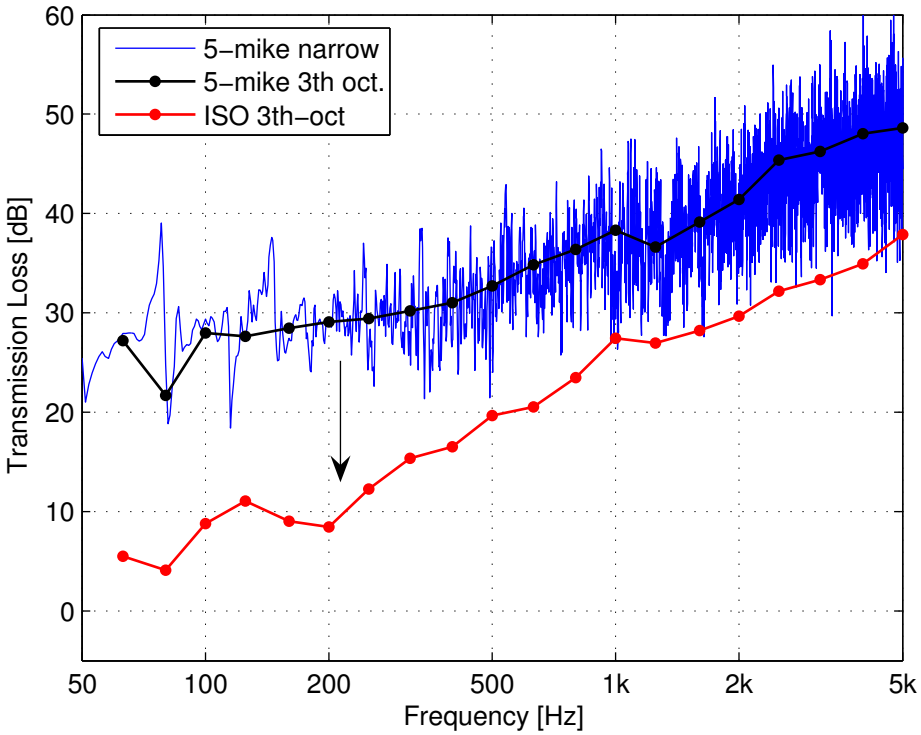

Figure 6.2: Narrowband transmission loss measured with the 5-microphone set-up (blue), its 1/3-octave band version (black) and the 1/3-octave band transmission loss measured with the intensity probe (red). The arrow denotes the scaling that needs to be done to match the 5-microphone measurement with the ISO measurement.

The difference between the black and the red line of Fig. 6.2 is plotted using black dots in the following figure, Fig. 6.3, and can be seen as the scaling factor[1] needed to transform the five-microphone transmission loss data into ISO-certified transmission loss data. To be able to correct narrowband results from the five microphones as well, cubic interpolation is applied to the black dots to obtain the blue line. Using this correction factor and the data from the error-microphones we can now plot narrowband transmission loss data too.

Ideally, this scaling line would be a flat line which would mean that every frequency is equally represented at the error locations. Differences are probably caused by differences in radiation patterns of certain modes, where the limited number of microphones do not pick up all frequencies equally. Because an active noise controller first focusses on the strongest frequencies at the microphones, a tone that is overrepresented in the error region is over-regulated by the controller.

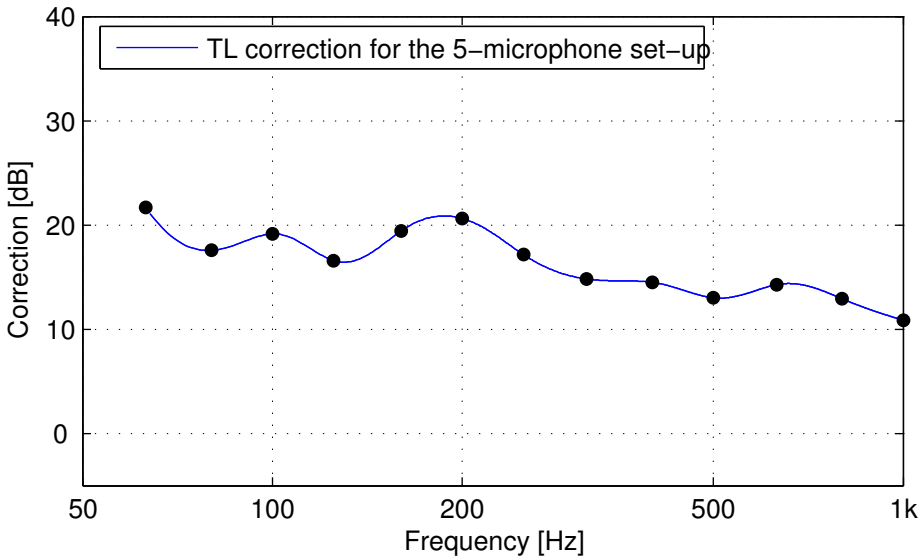

Figure 6.3: Correction values in 1/3-octave bands and dB for the difference between 5-microphone TL measurement and ISO intensity probe measurement results seen in Fig. 6.2 (black dots). After cubic interpolation a smooth narrowband line is obtained, which will be the correction for the narrowband measurements with the 5-microphone set-up. In the decibel domain all correction values need to be *subtracted* from the original transmission loss result.

Fig. 6.4 shows us the narrowband result (blue). What stands out is the strong modal character in the low-frequency area. The transmission loss at 81 Hz and 115 Hz is almost zero, meaning almost no energy loss for signals with those frequencies travelling through the plate. A signal of 78 Hz, however, would loose about 40 dB, meaning the acoustic energy behind the plate has been reduced with a factor 10^4. Something that would not have been found out if investigating the 1/3-octave results only.

[1] A scaling factor in the sound power dimension is a *scaling shift* in decibels.

Added to Fig. 6.4 are several analytical results using the equations of Chapter 2. The red line is the analytical prediction of the transmission loss through an infinite plate at normal incidence (Eq. 2.21). For field incidence, the transmission loss data is 5 dB lower (green line, Eq. 2.25). The theory for finite plates (Eq 2.29), which gives us the *worst case* transmission loss for frequencies between the resonances, is shown as a black line. It seems that, although generally a bit too high, this line is slightly better in predicting the average transmission loss trend: flatter in the low-frequencies and lower in the high-frequencies.

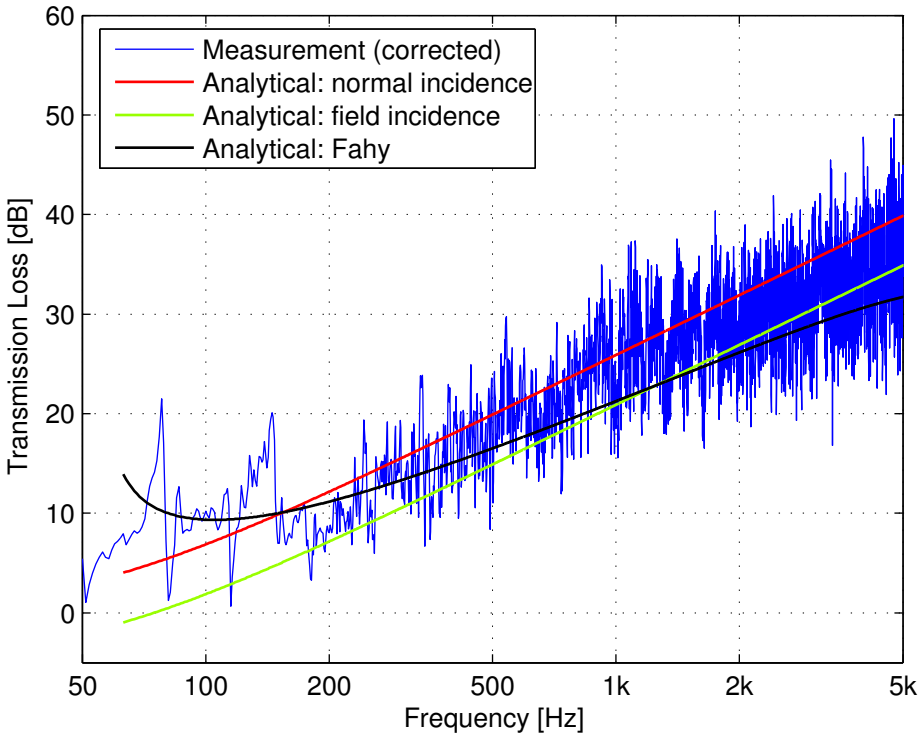

Figure 6.4: Corrected narrowband 5-microphone transmission loss data (blue), compared with the analytical normal incidence infinite plate transmission loss (Eq. 2.21) (red), field incidence infinite plate (Eq. 2.25) (green) and Fahy's finite plate transmission loss (Eq 2.29) (black).

Aluminium plate with foam and steel plate

As an example of passive noise control, a 4 mm thick layer of foam weighing approx. 1 kg is attached to the aluminium plate. This results in a slightly higher transmission loss in the high frequency area (see Fig. 6.5).

Another example of increasing the transmission loss passively is shown in Fig. 6.6, where the transmission loss of the 1 mm aluminium plate (2.5 kg) is compared to the transmission loss of a 1 mm thick steel plate (7.0 kg). It shows that a heavier plate does increase the overall noise reduction. However, for certain resonance frequencies the transmission loss still is very low[2].

The 1/3-octave band results of the aluminium plate without and with foam and the steel plate can be seen in Fig. 6.7. The mass-law explained in Paragraph 2.2.1 predicts us that the transmission loss of the steel plate will be about 9.3 dB higher than the aluminium one, which our results confirm.

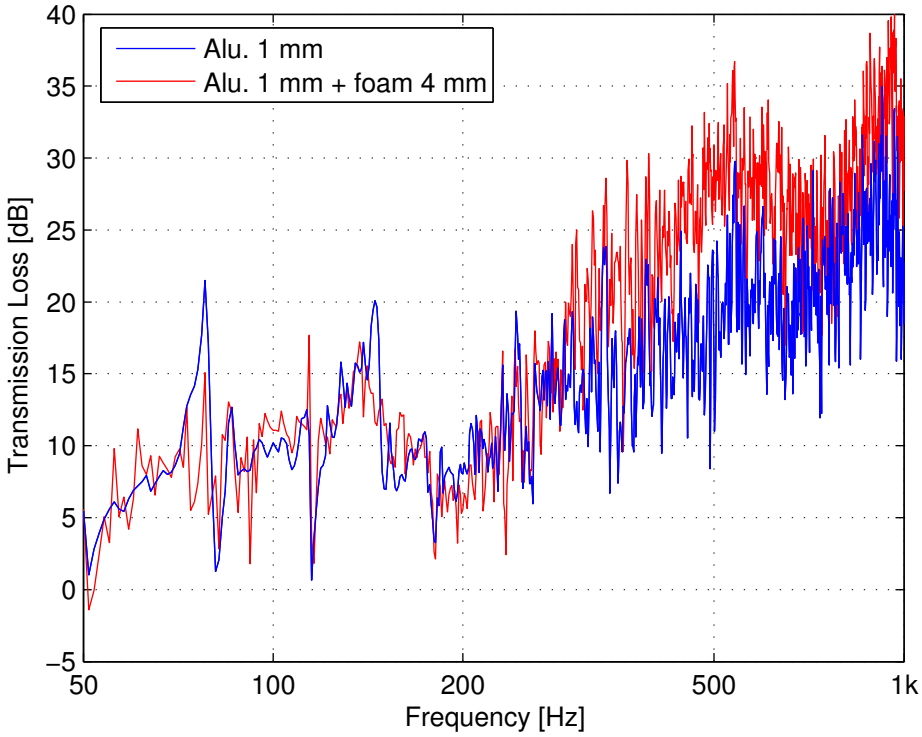

Figure 6.5: Corrected narrowband transmission loss of single 1 mm thick aluminium plate without (blue) and with (red) 1 kg/m^2 foam.

[2]Usually, in acoustics one automatically looks at the peaks of a plotted line. With transmission loss data one should focus on the *lows* instead. Around these lows almost all acoustic energy is transmitted and around those frequencies the noise reduction is most important.

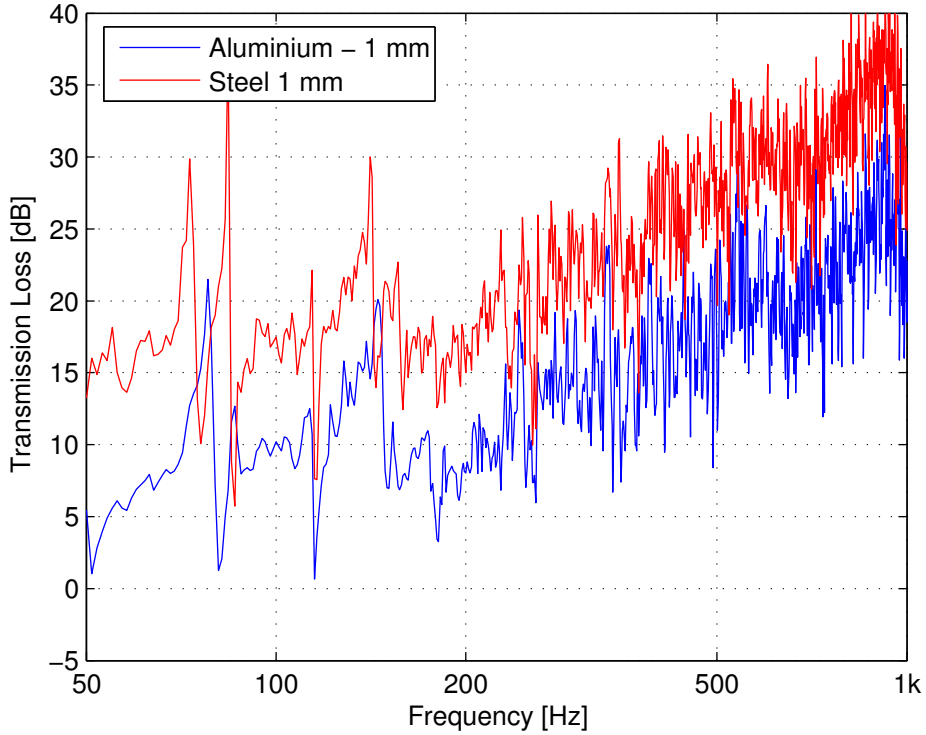

Figure 6.6: Narrowband corrected transmission loss for 1 mm aluminium (blue) and 1 mm steel plate (red).

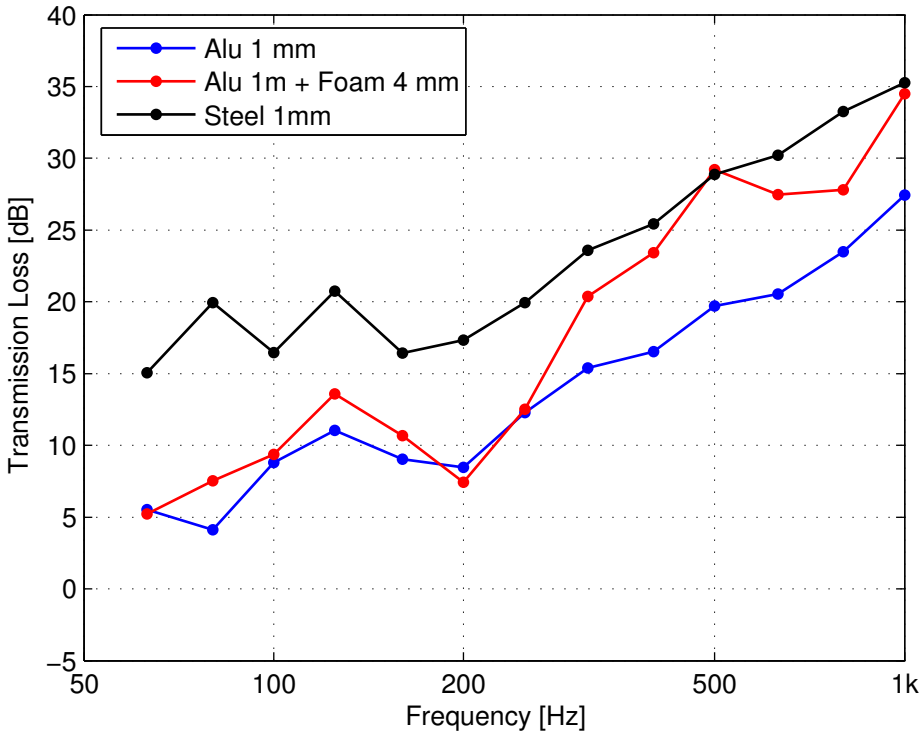

Figure 6.7: The 1/3-octave band transmission loss data of the 1 mm aluminium plate (blue), the aluminium plate with 4 mm foam layer (red) and the 1 mm steel plate (black).

6.3.2 Simulations

Normal incidence - aluminium plate

The first and least complicated simulation is the one for passive transmission loss at normal incidence, where the pressure wave at the source side is uniform across the surface. As stated in paragraph 5.3.4, all broadband signals used for the simulations are filtered by a low-pass filter to damp all frequency components higher than 1 kHz. The result is plotted as transmission loss data (red) in Fig. 6.8 and is compared with the measurement at random incidence[3] (blue).

The normal-incidence simulation has fewer participating modes, which can be seen in a smoother transmission loss line. If we compare the simulated result with the analytical normal incidence (see Fig. 6.9), there seem to be differences. It should be noticed however that the analytical calculation obeys the mass-law for infinite plates. This should be compared to the finite plate transmission loss values between two resonance frequencies, meaning the upper side of the red line.

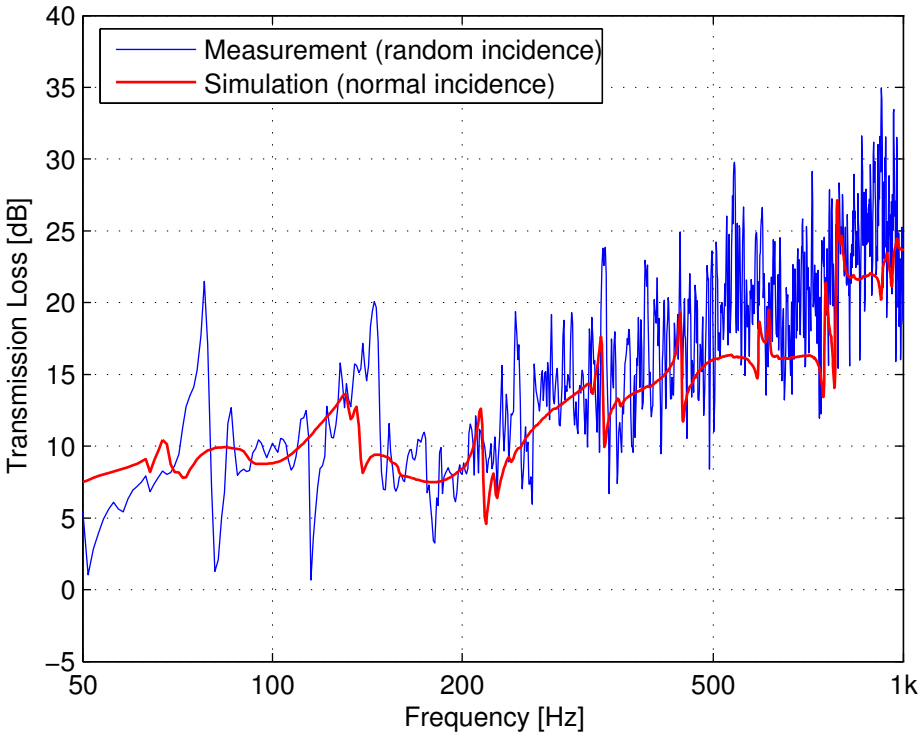

Figure 6.8: Transmission loss of the random incidence measurement (blue) and the normal incidence simulation (red) of the aluminium plate.

[3]Unfortunately there is no normal incidence measurement available.

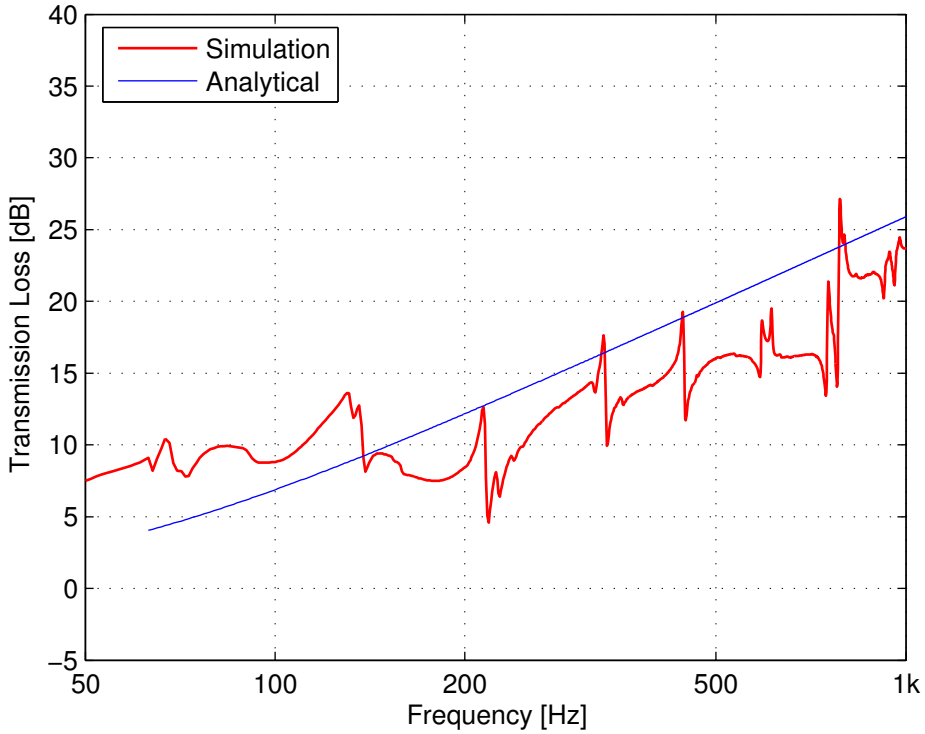

Figure 6.9: Transmission loss of the aluminium plate normal incidence infinite plate theory (blue) and the normal incidence simulation (red).

Random incidence - aluminium plate

To simulate the model with random incidence, we have to apply the theory explained in the previous chapter about random noise incidence. Chosen are 100 plane waves and a simulation length of 20.000 samples. The result, plotted in Fig. 6.10 as a red line, shows us that much more plate modes are excited than with normal incidence. Comparing measurement and simulation, we see that the two lines have a more or less similar trend. On a narrowband scale, we sometimes see considerable differences. For example, the low in the measured transmission loss at 115 Hz did not appear at all during simulation.

Fig 6.11 shows the 1/3-octave band version of Fig. 6.10. As with the narrowband results, there are low-frequency differences between measurement and simulation. In the high-frequency area there seems to be an increasing error for increasing frequency. Because the experimental set-up is designed for accurate measurements up to at least 5 kHz and the 10 kHz transient simulation sample rate ensures accurate simulation results up to only 500 Hz, it is assumed that numerical errors are responsible for the high-frequency differences. Besides sampling rates, also the element size should be taken into account for higher frequency FE simulations (see also Paragraph 5.3.1).

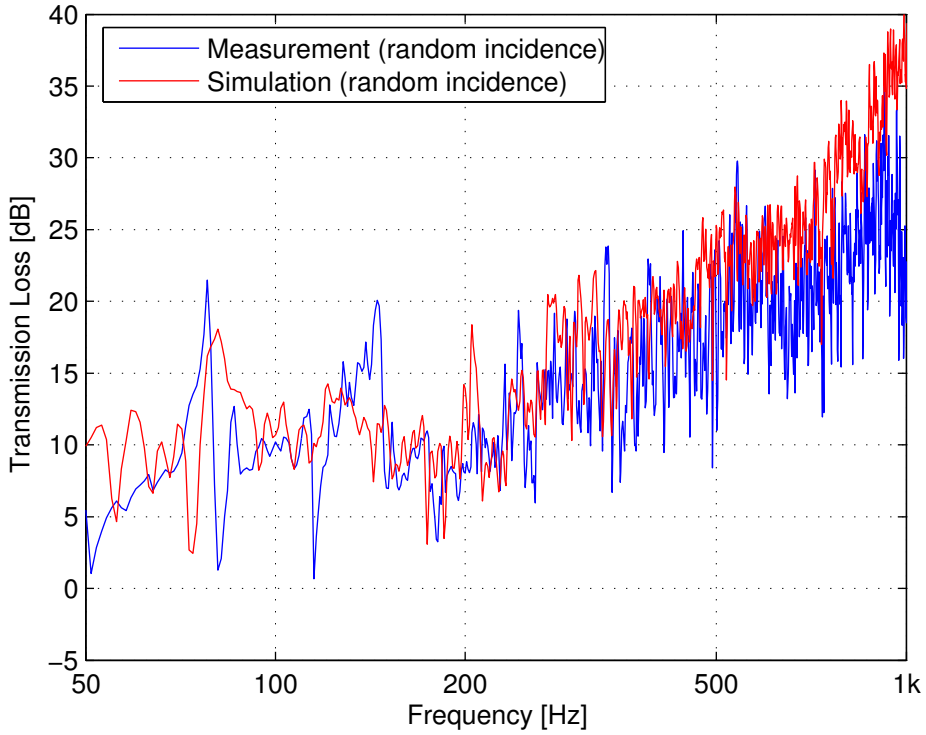

Figure 6.10: Transmission loss of the random incidence measurement (blue) and the random incidence simulation (red) of the aluminium plate.

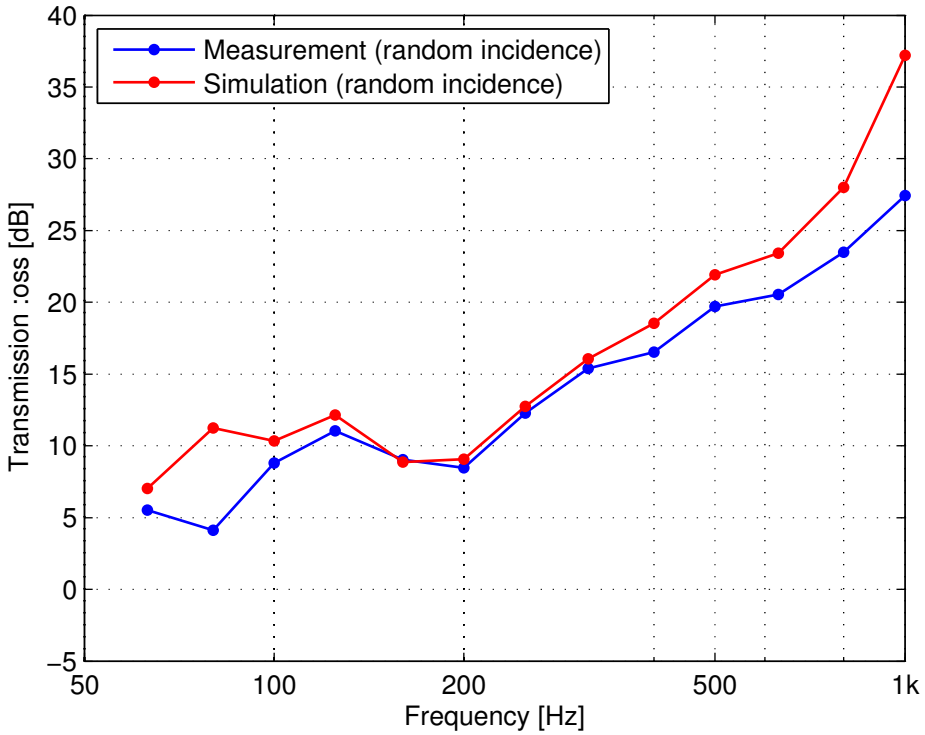

Figure 6.11: Same as Fig. 6.10 but in 1/3-octave bands.

Steel plate

Having a computer code available that simulates the transmission loss of a plate, it is only a small step to change from aluminium to steel: only three material constants in the code need to be changed (material properties: see paragraph 5.2.1). The result of the simulation with random incidence can be found in Fig. 6.12. Again, although there are some narrow band differences, the trend of the simulated result (red) corresponds with the one of the measured (blue).

Fig. 6.13 shows the 1/3-octave band transmission loss data of measurement and simulation again. Although less than for the aluminium plate, also here the high-frequency area shows an increasing mismatch between measurement and simulation.

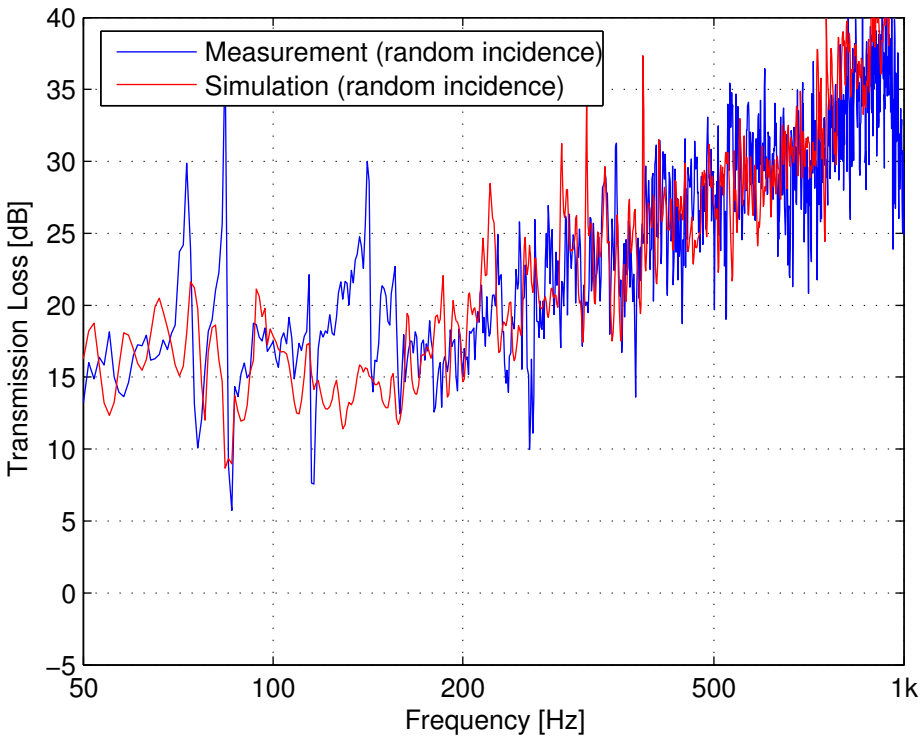

Figure 6.12: Random incidence transmission loss of the 1 mm steel plate from measurement (blue) and simulation (red).

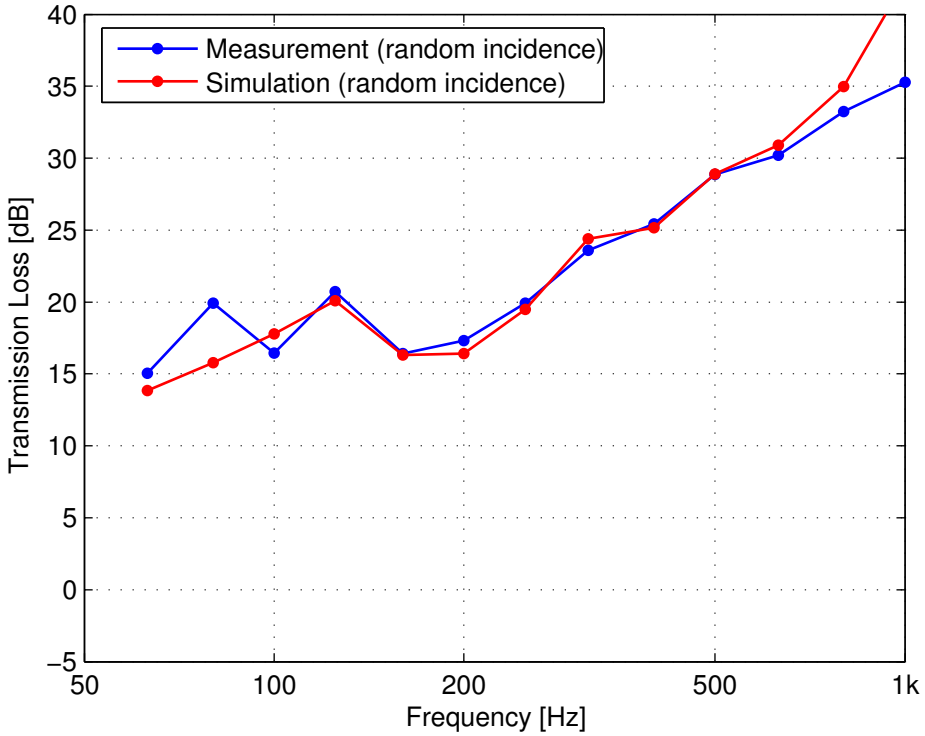

Figure 6.13: The same as Fig. 6.12 but in 1/3-octave bands.

6.4 Active transmission loss

6.4.1 Experiments

System identification

Before starting to actively control the sound that is transmitted by the plate, the experimental set-up needs to be identified by estimating the impulse responses from each actuator to each error sensor. Every time the system changes, for example when the plate is replaced or when the position of the actuators is changed, this has to be redone.

The least-mean-square system identification of the controller that is used estimates the impulse responses during a time length that can be set in advance. Online it can be observed how the controller optimizes the impulse responses during the first five seconds. If a long identification length is set, the computer will keep on trying to improve during the given time, even if an optimum is found and no improvement can be observed.

In Fig. 6.14 the impulse response and frequency spectrum from actuator 1 to the central microphone 5 is shown. In the time data, it can be seen that the first peak starts at approximately 11 ms, this although the acoustic travel time at room temperature for 1.5 m distance is about 4.3 ms. To explain this difference, it should be noted that this impulse response is not just the acoustic response from actuator to microphone; it is the complete response from the output to the input of the controller including influences from the used amplifiers, A/D-converters, anti-aliasing filters etc.

In the lower plot the spectrum of the impulse response can be seen. It shows big amplitude differences and, due to the 10 log-dependency, a difference of 20 dB in this plot is equivalent to a 40 dB difference in the sound pressure level at the microphone location. Of the first three peaks (81 Hz, 115 Hz and 148 Hz) only the first two are also strongly present in the passive transmission loss plot (see for example Fig. 6.4). The peak at 148 Hz apparently is a frequency with efficient central actuator radiation, but has low response when the plate is excited by a diffuse sound field.

Something else that attracts attention in the spectrum plot is the strong decay for higher frequencies, starting from about 500 Hz. This is probably the result of the controller's internal filtering that makes sure that signals above the upper limit of 800 Hz are damped (see Paragraph 5.2.3).

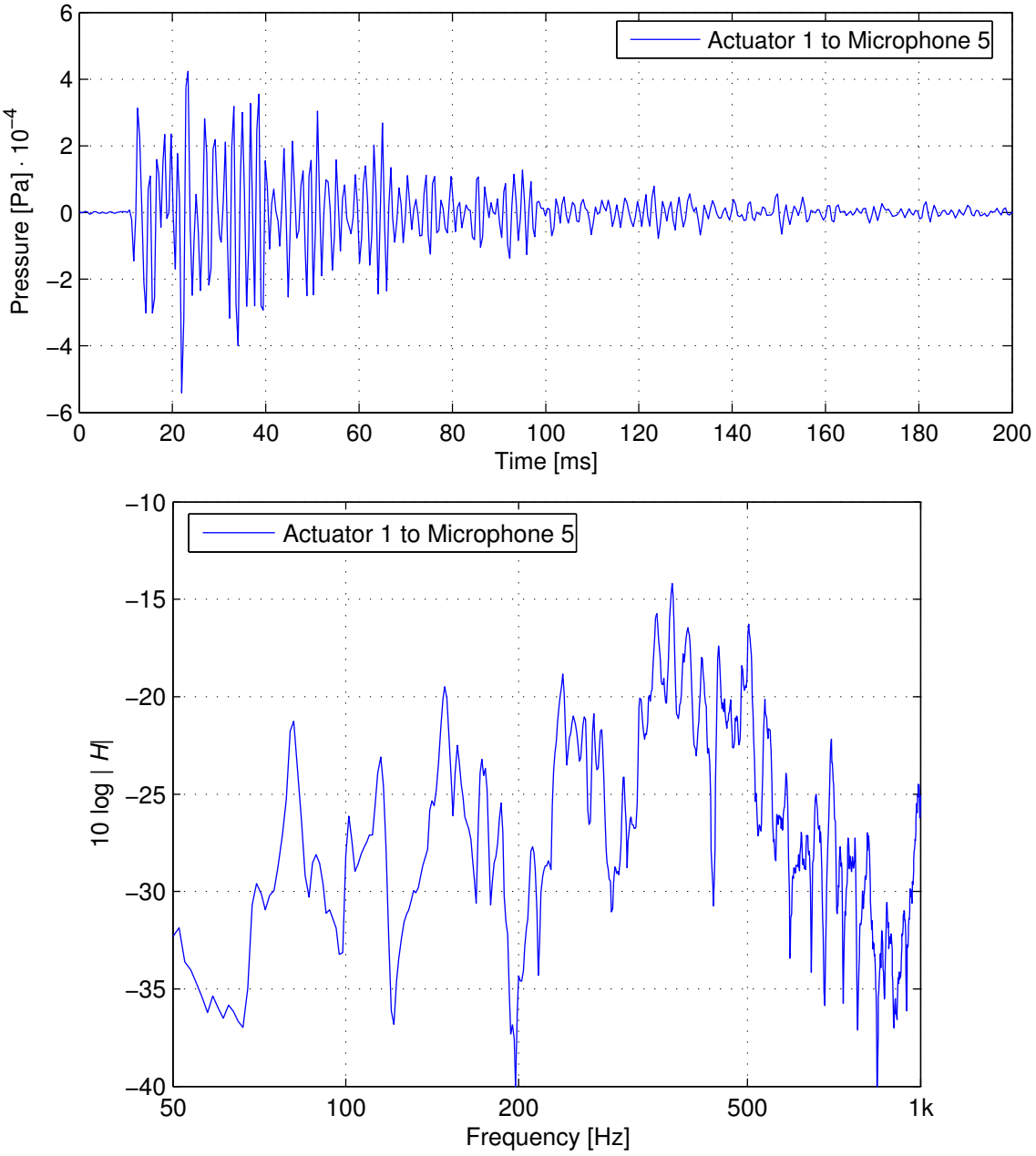

Figure 6.14: *Upper figure*: Impulse response from output 1 (central piezoelectric actuator) to error microphone 5 (central microphone). After about 200 ms (with a a sample rate of $F_s = 15625/8 = 1952$ Hz this means about 390 samples) the impulse response is declined to almost zero. *Lower figure*: Frequency response function (FRF) and spectrum of the above time signal. It shows a strong modal character as well as an amplitude decline above 500 Hz.

ANC with white noise

The same broadband noise settings used for the passive transmission loss measurements are now used for our active experiments. After turning on the controller, it adapts to a steady state situation in which it seems to especially focus on the peak around 80 Hz and the peaks between 150 and 220 Hz (see Fig. 6.15). The figure shows the controllers strategy: analysing the error sensor signals it will focus on the strongest peak and tries to reduce it. If that peak is successfully reducing and drops below other peaks, it will start focussing on the new highest peak as well, etc..

Looking at this figure, we see strong peaks in the error sensor signal. This signal is in fact only an average of all error microphones and the average in time. In reality, the peak at about 80 Hz for example is not a constant tone but fluctuates in amplitude. This random fluctuation causes difficulties for the controller. It can not predict the future behaviour of the error signal very well, and therefore can not anticipate it.

The results of these active and passive measurement with broadband noise can also be shown in the form of a transmission loss plot. Fig. 6.16 shows the transmission loss with and without active control, again corrected for the 5-microphone set-up. As expected from the error sensor data, reduction is achieved around 80 Hz and in the area from 120 to 220 Hz.

Interesting to see in the 1/3-octave band plot is that the higher the frequency gets, the less noise reduction there is. This can be explained by the fact that for high frequencies, meaning high phase changing, the controller has less time to predict the near-future signal and respond to it accurately.

The current paragraph has shown that it is difficult but not impossible to actively increase the transmission loss for random broadband noise. With a lightweight low-damped plate with strong resonances, the white noise transforms into noise with stronger tonal character at the radiated side. These tonal properties make the work for the controller a bit less difficult: it can focus on those frequencies and try to reduce them first.

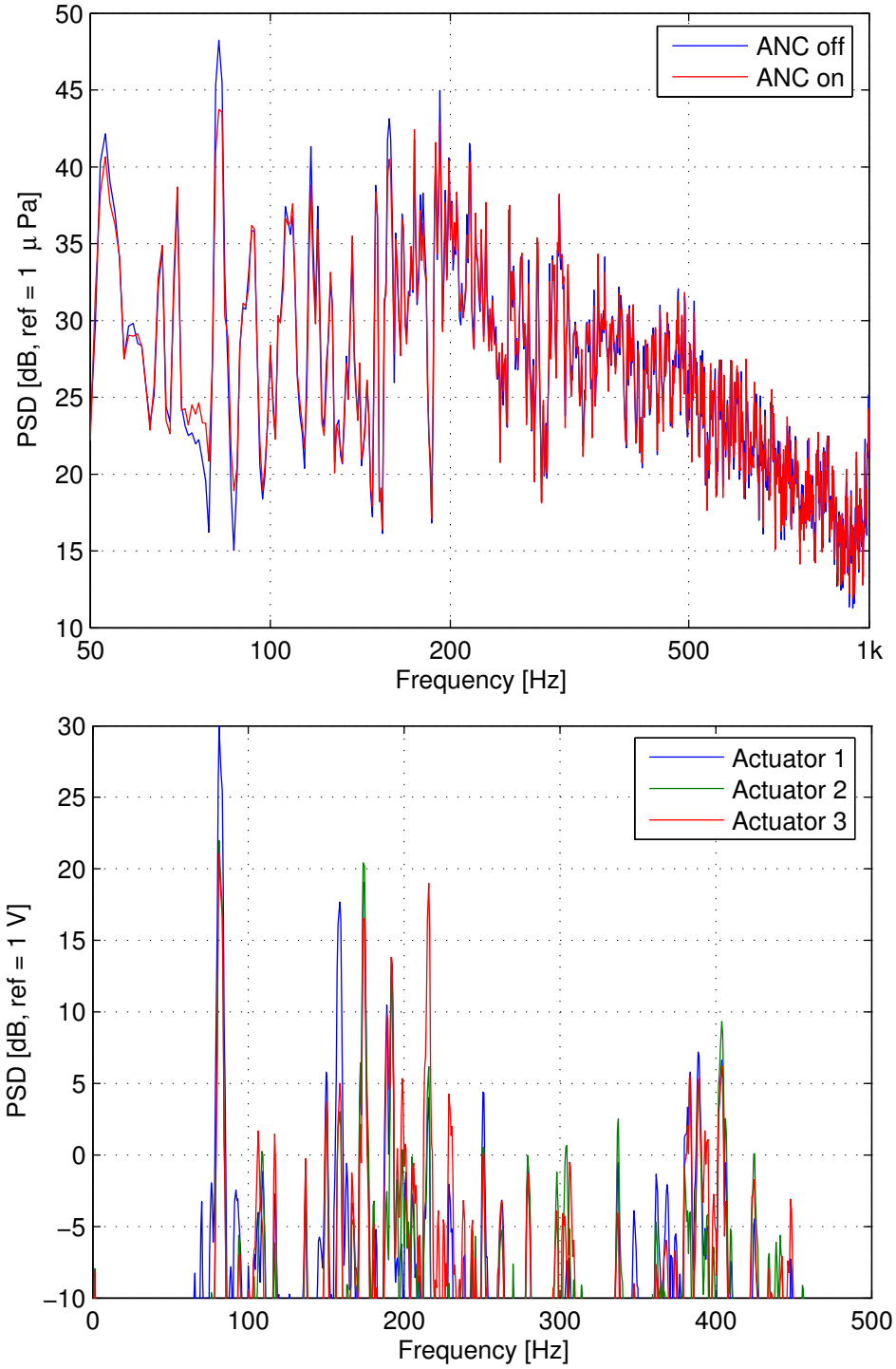

Figure 6.15: *Upper figure*: Average power spectral density of all five microphones with (blue) and without (red) active noise control. *Lower figure*: PSD of the three actuators during active noise control.

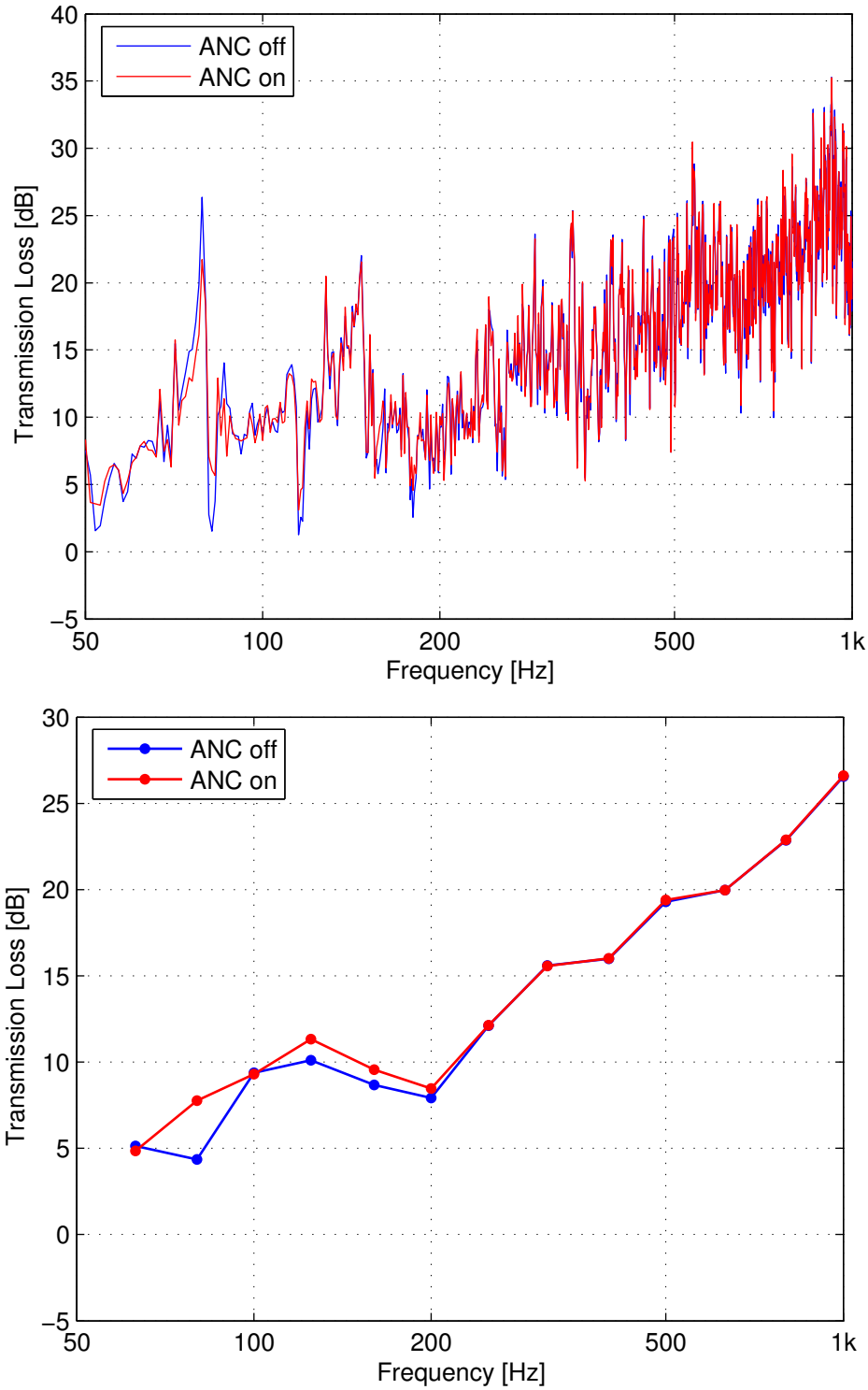

Figure 6.16: *Upper figure*: Transmission Loss with and without ANC for white noise excitation. *Lower figure*: The same but in 1/3-octave bands.

ANC with tonal noise

During the experimental system identification of Paragraph 6.4.1 we have seen that the central actuator has strong radiation peaks at 81 Hz, 115 Hz and 148 Hz. The narrow-band transmission loss data plotted in Fig. 6.4 showed that the plate's sound transmission for 148 Hz is not so high as for the other frequencies. This will probably mean that for this frequency the ANC system has a relatively high potential: with small actuator effort a loud 148 Hz sine-tone can be reduced.

Using a signal generator the sinusoidal signal is sent to the loudspeakers in the reverberation room. At a certain point in time we call $t = 0$, the controller is turned on and starts looking for an optimum in minimizing the error signals. In Fig. 6.17 the signals of microphone 5 and actuator 1 are shown as an example. After about 0.75 s a reduction of approximately 14 dB is reached. After that time the controller keeps trying to improve, but the error signal does not reduce any further. At steady state the voltage at piezo 1 is approx. 26 V_{RMS} and the electrical current is 6.2 mA_{RMS}, meaning an electrical power consumption ($P = V \times I$) of the piezoelectric actuator of only 0.16 W_{RMS}.

To investigate what happens at the plate surface in steady state control we can use the intensity probe again to scan the radiated intensity at the plate's surface. Results of this procedure are given out in 1/3-octave bands, and the intensity distribution at the 160 Hz-band (which includes the 148 Hz tone) is shown in Fig. 6.18.

Fig. 6.19 shows us the difference in dB between the two intensity measurements. In the figure it can be seen that at the lower half of the plate the radiated intensity has a reduction of about 20 to 50 dB. The upper half, and more precise, the upper right corner, only reaches a reduction of about 5 dB.

Looking at the intensity figures, we can understand why the controller is not able to reduce the 148 Hz peak even more. In this case it is not the limitation of the actuator power that plays a role (which was 20 W_{RMS} according to paragraph 5.2.3). It seems that actuators can reduce the noise radiated from the center and the lower part of the plate easily, but if the reduction at the top part does not improve, the signal at the error sensors does not decline.

In the lower part of Fig. 6.17 a second peak can be seen around 300 Hz. Because this peak is also present in the passive plot (left, without control) it can only be caused by the harmonic distortion at the source side in the reverberation room. Because it is not decreasing nor increasing, it can be concluded that the piezo-actuators do not have significant harmonic distortion for this tonal output.

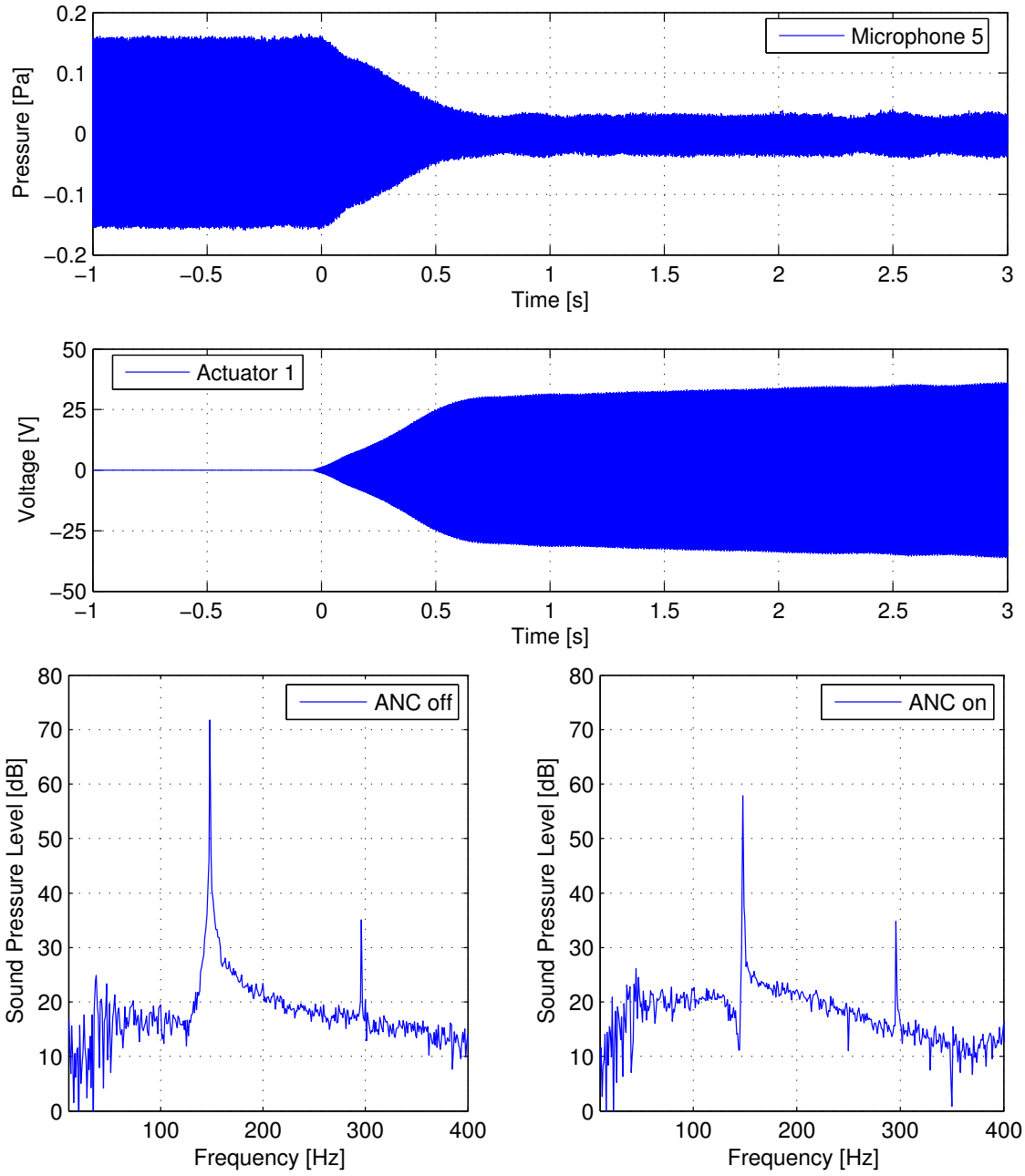

Figure 6.17: *Upper figure*: Plots of the time signals on the central microphone (nr. 5) (upper axis) and on the central actuator 1 (lower axis) during the start of the ANC. *Lower figure*: Sound power levels of microphone 5 with ANC off (left) and ANC on (right). A reduction of approx. 14 dB is reached.

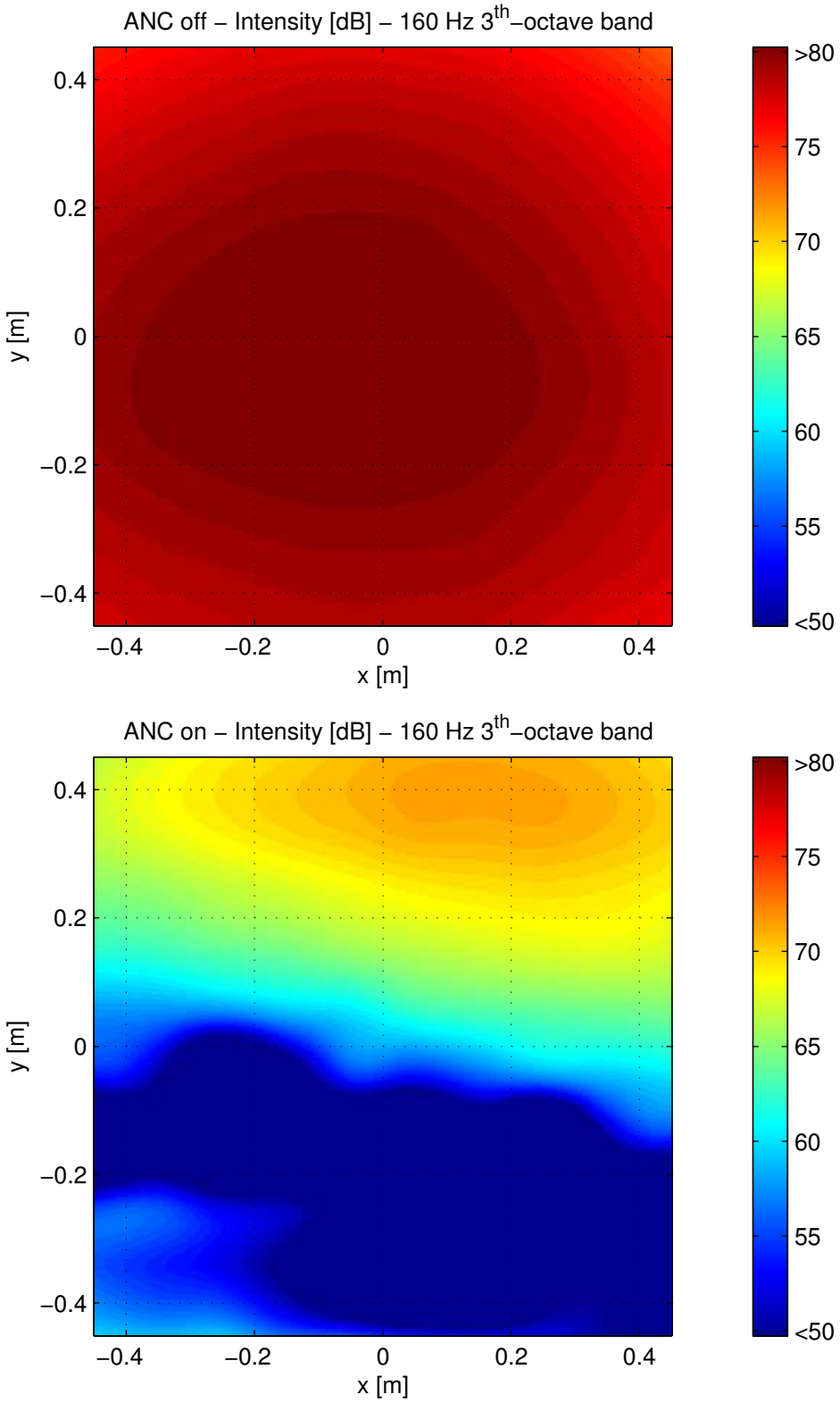

Figure 6.18: Intensity distribution over the plate for the 160 Hz 1/3-octave band with active control turned off (upper figure) and turned on (lower figure).

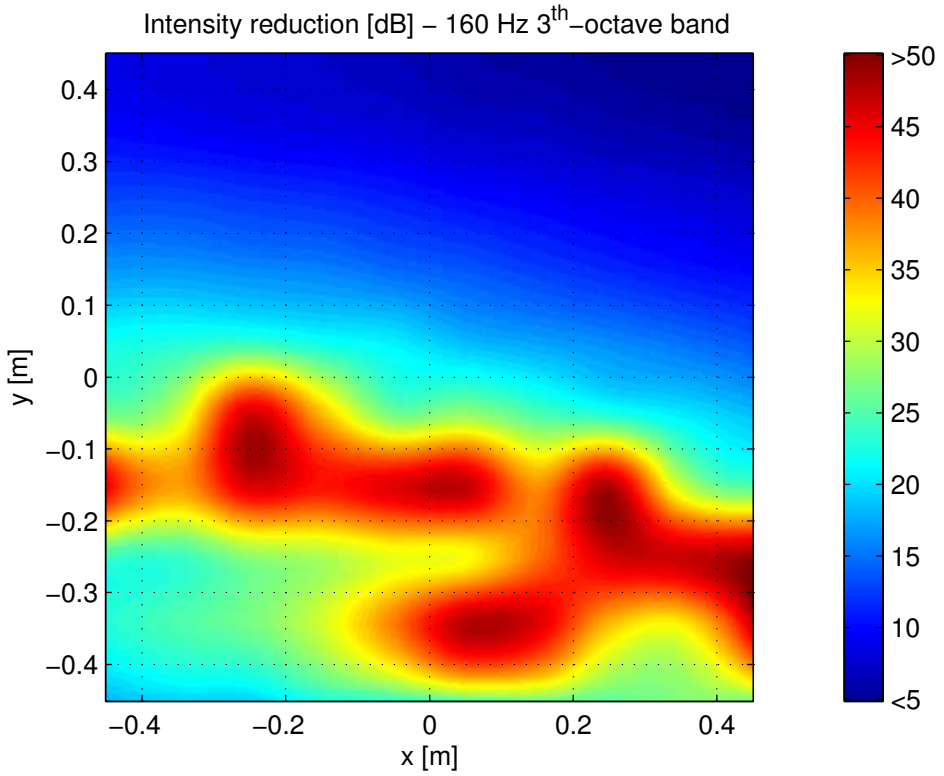

Figure 6.19: Intensity difference between active noise control off and on (Fig. 6.18).

ANC with sweep signal

The third noise type discussed in paragraph 5.2.3 is the sweep signal. In this case the frequency of the sine tone is gradually increasing from 50 to 500 Hz within 25 s, corresponding to an increase of 18 Hz/s.

In Fig. 6.20 the result without and with ANC can be seen in a form of a spectrogram[4]. Because it is rather difficult to see the reduction from the colours alone, a difference-plot is given in Fig. 6.21.

To not let big differences in the background noise disturb the difference-spectrogram, a background pressure value corresponding with 45 dB is added, which is about 25 dB lower than the highest peak. Result is a spectrogram which is zero outside the region of interest and shows reliable values for the sweep signal. In the difference-plot can be seen that there are frequencies for which the reduction is up to 8 dB. For other frequencies the controller is not able to reduce the error signals.

It also seems that for some frequencies even an amplification can be observed. If the amplitude of the noise for that frequency is low this is however not a problem.

The sweep signal spans a wide frequency spectrum and can be shown in form of a transmission loss curve as well (see Fig. 6.22). Ideally, the transmission loss should be independent from the type of noise signal, as long as all frequencies are represented. Practically, there are some differences compared to the normal transmission loss measurement.

On first appearance the reduction due to ANC seems less than expected: Fig. 6.21 did show us reductions up to 8 dB for some frequencies; the transmission loss curve however does not increase with that amount. The problem probably is that the transmission loss is determined using averages, also including the part of the signal for which the controlling is adapting itself but not yet reducing the noise. This part does of course not show up in the difference-spectrogram because the difference with the ANC off signal is zero. In the TL diagram this unreduced part can not be ignored, leading to a transmission loss difference due to ANC of less than 8 dB.

[4]The spectrogram shows the spectrum of a signal at different points in time, using the DFT. In this case the colour represent the sound pressure level.

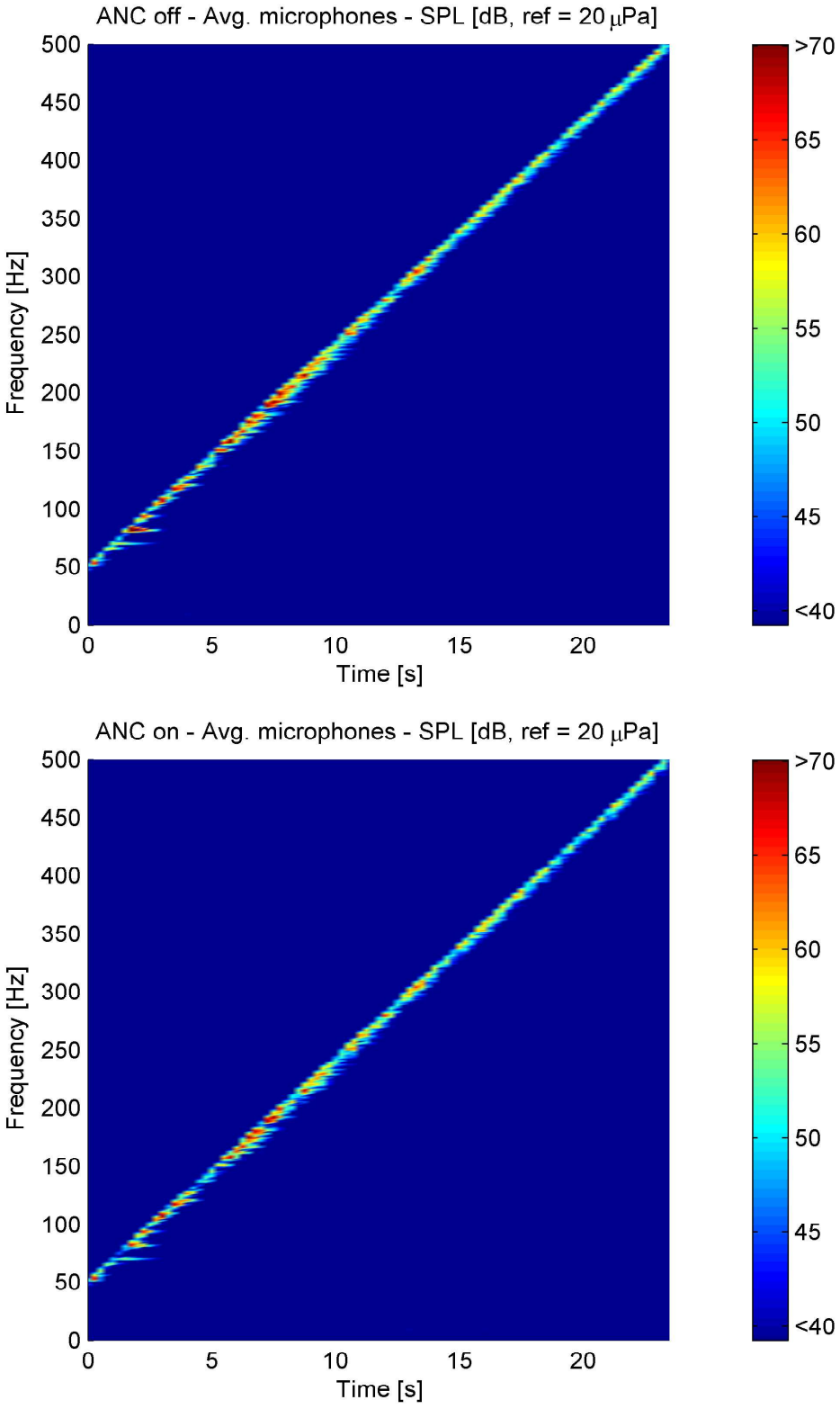

Figure 6.20: *Upper figure*: Spectrogram of the average sound pressure level of the five microphones during the frequency sweep, active noise control is off. *Lower figure*: The same as above but with ANC on.

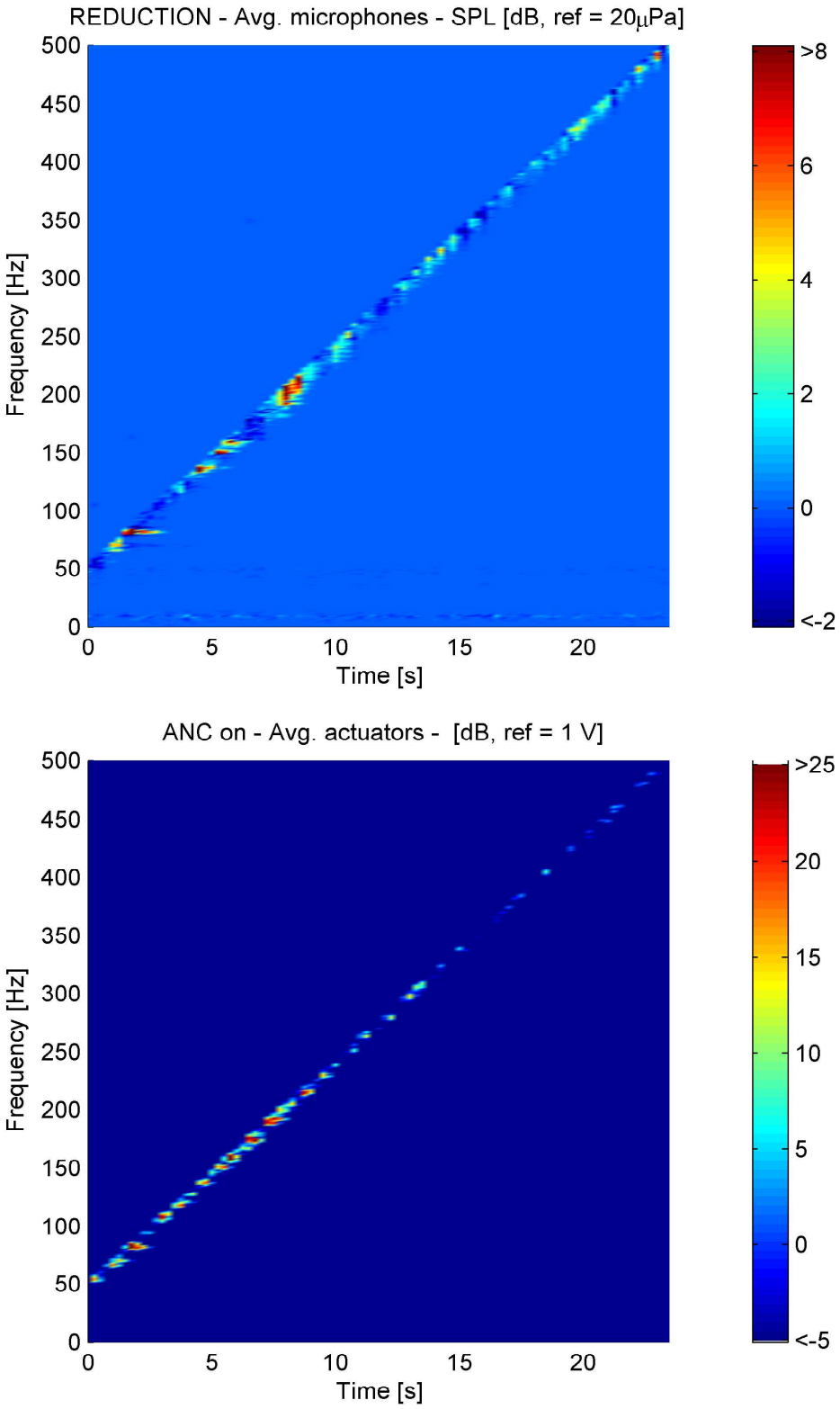

Figure 6.21: *Upper figure*: Average reduction on the five microphones due to active noise control, which is the difference between the two figures in Fig 6.20. *Lower figure*: Average output of the three actuators during active noise control.

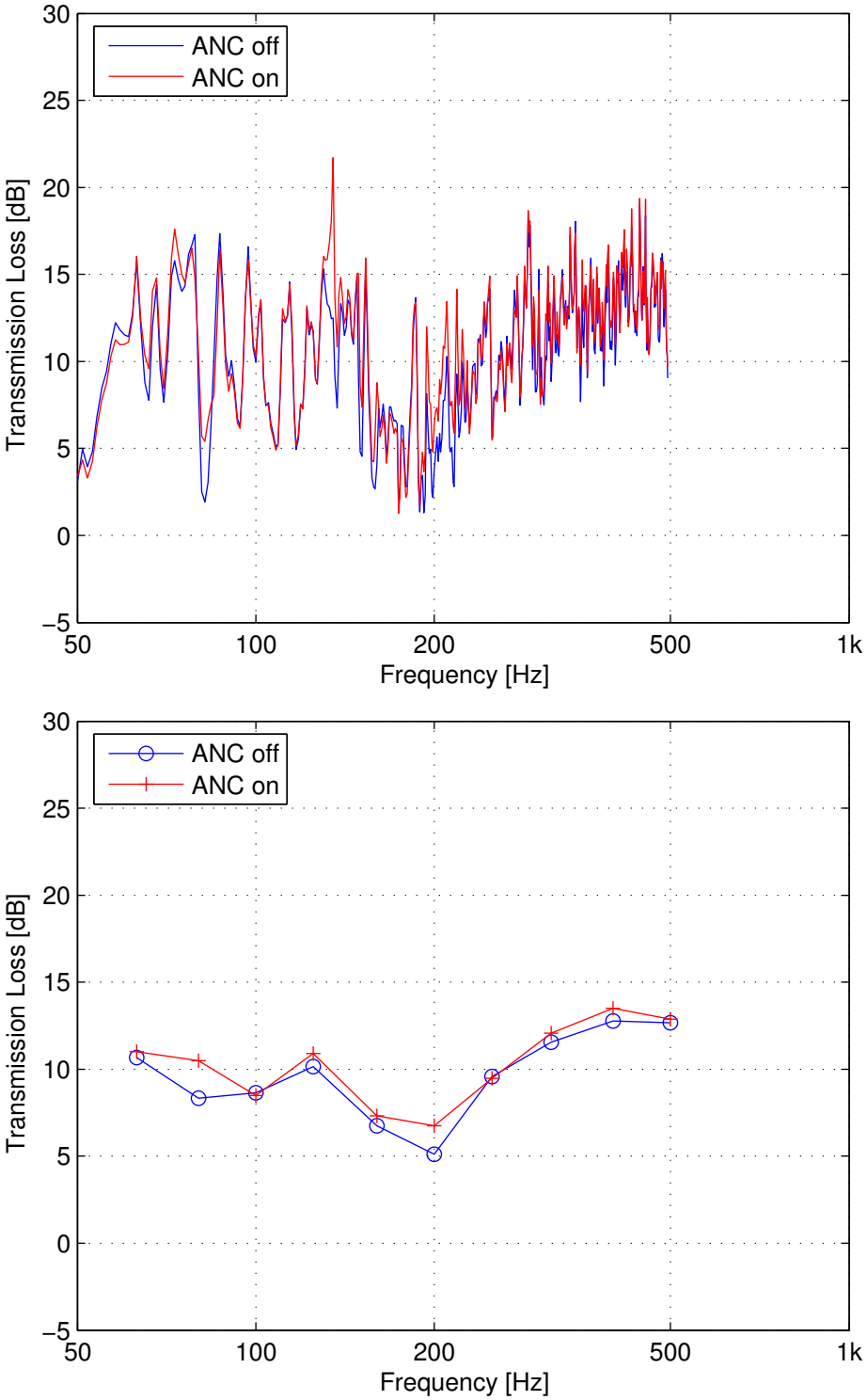

Figure 6.22: *Upper figure*: Measured narrowband transmission loss with sweep signal source, with and without ANC. *Lower figure*: The same but in 3$^{\text{rd}}$-bands.

6.4.2 Simulations

System identification

To simulate the impulse responses from the actuators to the microphones, we can either use the SYSID1 algorithm for each single set of actuator and microphone, or SYSID2 for the multichannel system identification algorithm (see Paragraph 5.4.1). Both lead to the same result and the estimated impulse response from actuator 1 to microphone 5 is shown in Fig. 6.23. The source signal is a randomly generated signal of moments at the nodes around the actuator position and a time length of 5 s is used.

As a comparison, the FRF of the measurement (orange) is plotted too. Looking at the peaks and the lows of both lines, some similarity can be observed between both lines in which the blue line is shifted a bit to the left, corresponding to a frequency mismatch of about 10%. Possible causes for the differences between the two lines are probably due to modal differences of the real and the simulated plate. Also the simulation approach of the actuator-plate interaction probably plays a role here. The use of different anti-aliasing low-pass filters can be noticed from the fact that the measurement line already decays at 500 Hz, whereas the simulation response is not damped until 1 kHz.

As briefly mentioned in paragraph 5.4.1, it might be possible to simulate the impulse response using a delta pulse instead of random noise as a source signal. In the real situation it is not possible to create such a pure delta pulse at the actuator without distortion. Besides that, also the presence of background noise could influence the result. To minimise this influence and to avoid a distorted pulse signal, random noise or a sweep signal is generally used.

For the simulations environment, both these problems do not exist. If possible, a system identification using a delta pulse would reduce the simulation time by far: no lengthy optimisation process is needed to get to the desired impulse response results.

The spectra of the two frequency response functions, for random noise and the delta pulse, can be compared in Fig. 6.24. It shows that this way of determining the impulse response returns a smoother line. The simulated time per actuator has been reduced from 5 s for the LMS/white noise method to 0.250 s for using a delta pulse. Expressed in actual calculation time this approach reduces the calculation time from 30 hours for all three actuators to only 1.5 hours.

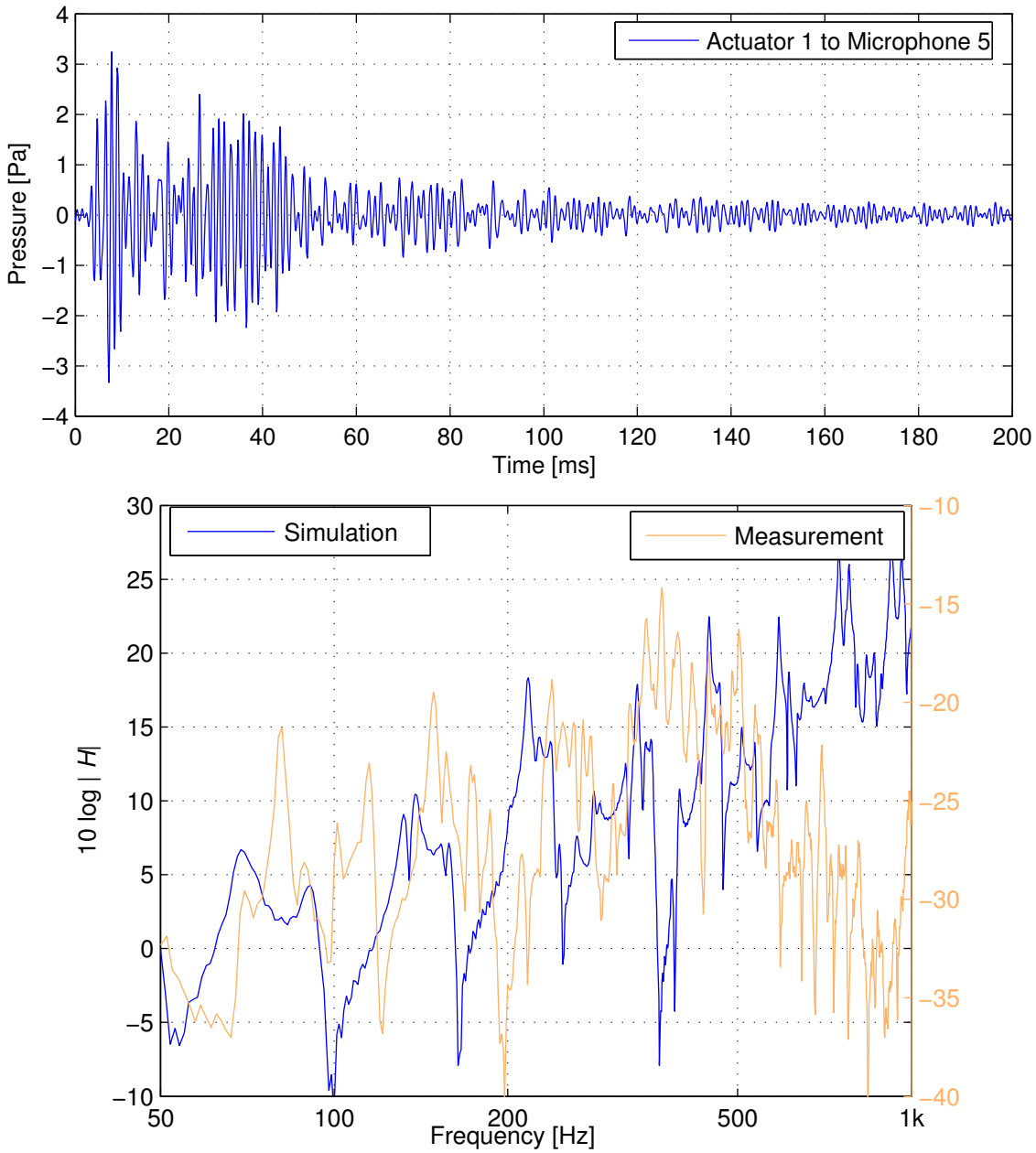

Figure 6.23: *Upper figure*: Simulated impulse response from the central output actuator to the central error microphone. *Lower figure*: Frequency response function of the above time signal (blue). The orange line is the frequency response function from the measurement.

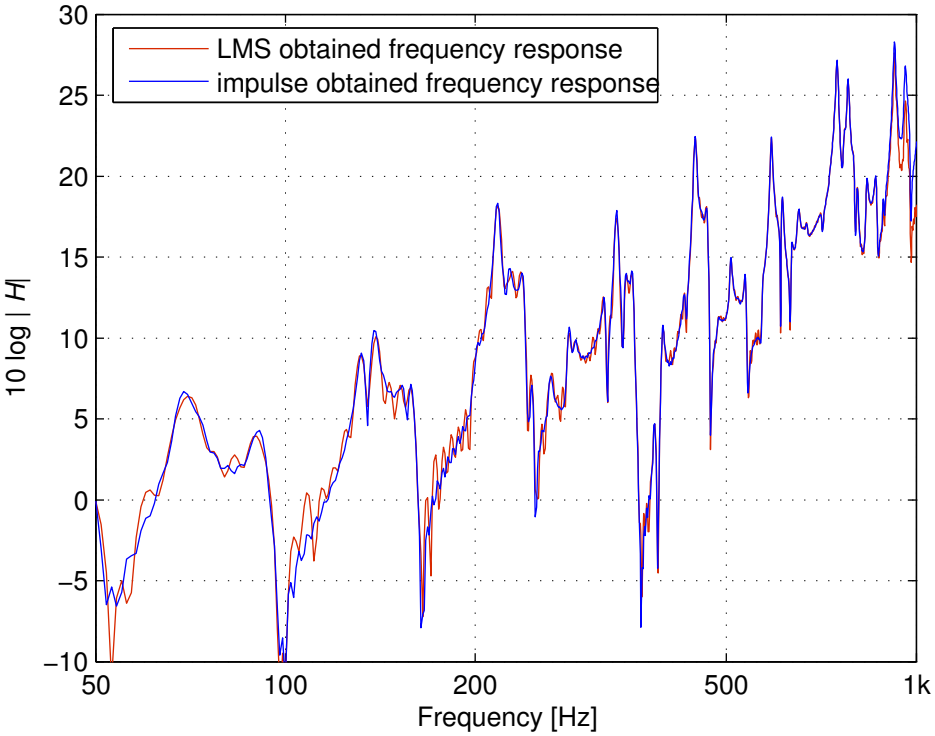

Figure 6.24: Comparison between the simulated frequency responses function using the LMS algorithm (red line) and using a delta-pulse (blue line). This clearly shows that the impulse, which is more efficient, can be used to determine the frequency response functions from the actuators to the error sensors.

White noise excitation

Using the previously obtained impulse responses we can start the simulations for broad-band random noise. For better comparison between no control and active noise control the same source load is used for both simulations. The results are plotted in Fig. 6.25.

As we have already seen with the experiments, the ANC algorithm starts focusing its effort on the highest peak, in this case the one around 70 Hz. After some reduction, the peaks around 200 Hz become the highest and have the most influence on the error signals, consequently the controller starts trying to reduce those next. For some peaks, there is no reduction at all, although the output shows that the ANC algorithm is trying to reduce them by sending that frequency to the output channels. Apparently it does not find an optimal filter for which reduction at those frequencies would take place too.

The corresponding transmission loss curve can be found in Fig. 6.26. Compared to the experimental results in Fig. 6.26, we can say that the simulated reduction is not as high as it was for the experiments. The frequency span however is a bit wider. Although very small, reduction is possible up to about 500 Hz.

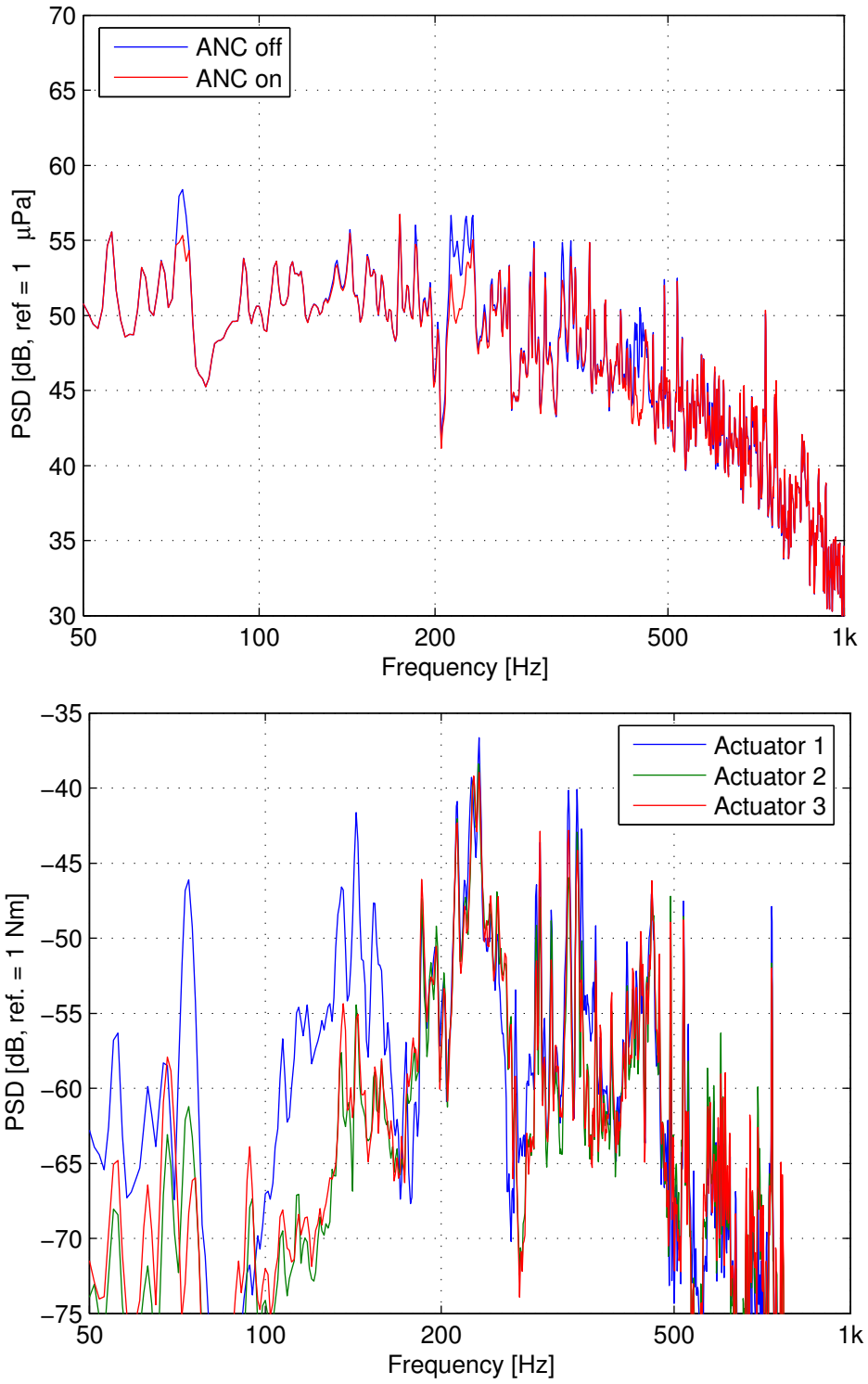

Figure 6.25: *Upper figure*: Average power spectral density of the pressure at all five microphone positions with (blue) and without (red) active noise control. *Lower figure*: Power spectral density of the three actuators during control.

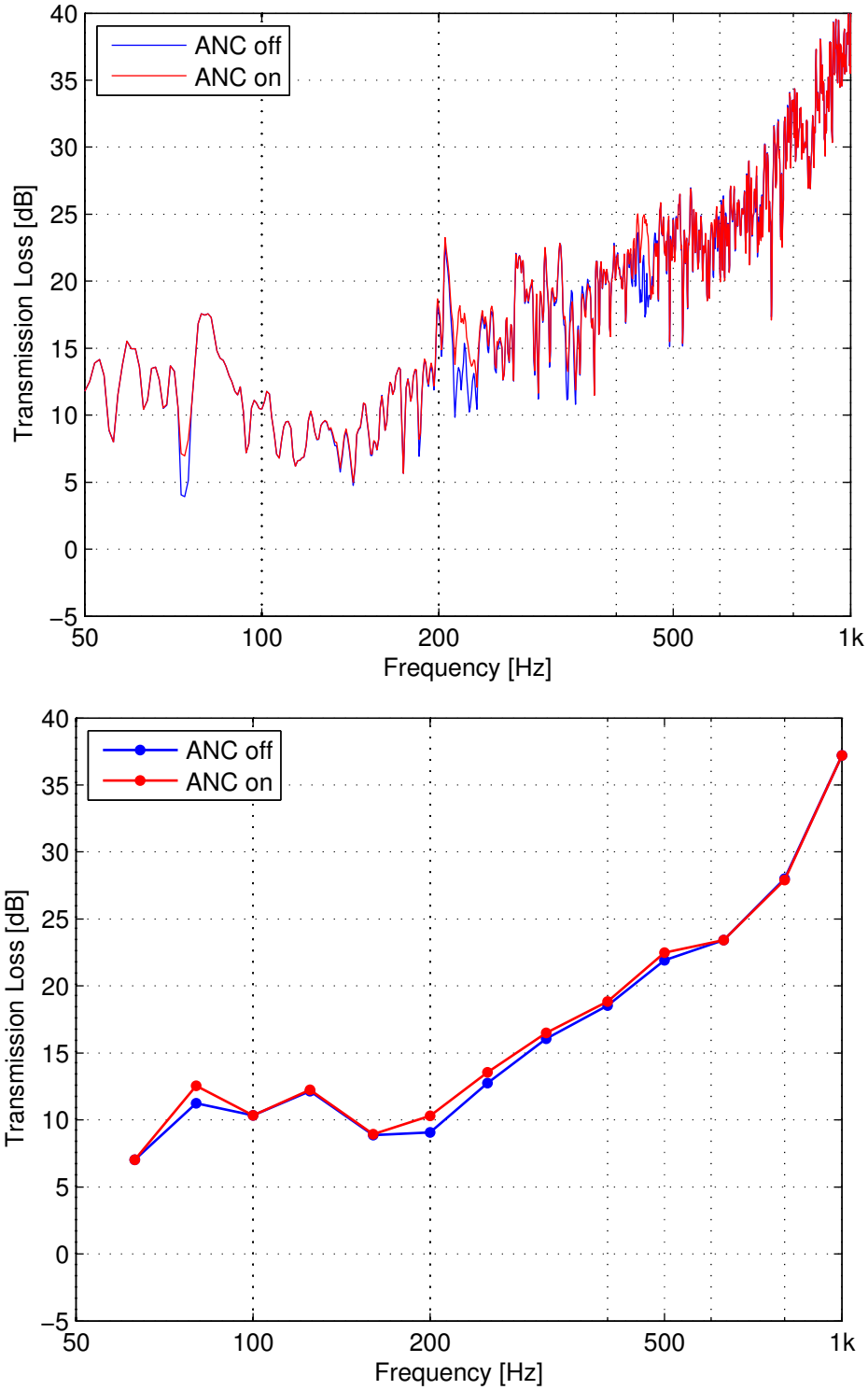

Figure 6.26: *Upper figure*: Transmission Loss with and without ANC for random noise simulation, corrected for the five-microphone set-up. *Lower figure*: The same but in 1/3-octave bands.

Tonal noise excitation

Similar to the experiments of the previous paragraph, the FE simulation and ANC algorithm are tested with a sinusoidal signal of 148 Hz. Instead of (filtered) random noise, the randomly spread plane wave sources all send out this sine function now.

The results show that the simulated noise reduction for tonal noise is significantly higher than the experimental reduction: a reduction of 27 dB is reached after about 500 ms (see Fig. 6.27).

The radiated intensity over the surface of the plate model can be estimated using the normal velocity at all nodes (see also Eq. 2.3). The result for ANC off and ANC on is shown in Fig. 6.28. Again, the upper right corner still radiates the most acoustic energy during control (compare with Fig. 6.18). Looking at the intensity differences (Fig. 6.29), this time the dark blue area of low reduction is not as large as it was for the experimental result (Fig. 6.19). On the other side of the spectrum we see that the red area of very high reduction from the experiments is almost gone.

Thus comparing measurement and simulation intensity differences, we see that the maximum and minimum reduction for the simulation are less extreme compared to the measurement. It appears that the simulated actuators have a wider controlling range on the plate than the real ones. Displaying the overall reduction at the error sensors in decibel, it means that the highest intensity reduction at the plate does not play a role. Even if the measurement is able to reduce parts of the plate with more than 50 dB, if one corner of the plate still radiates almost the same energy as it did without control, the overall result is poor.

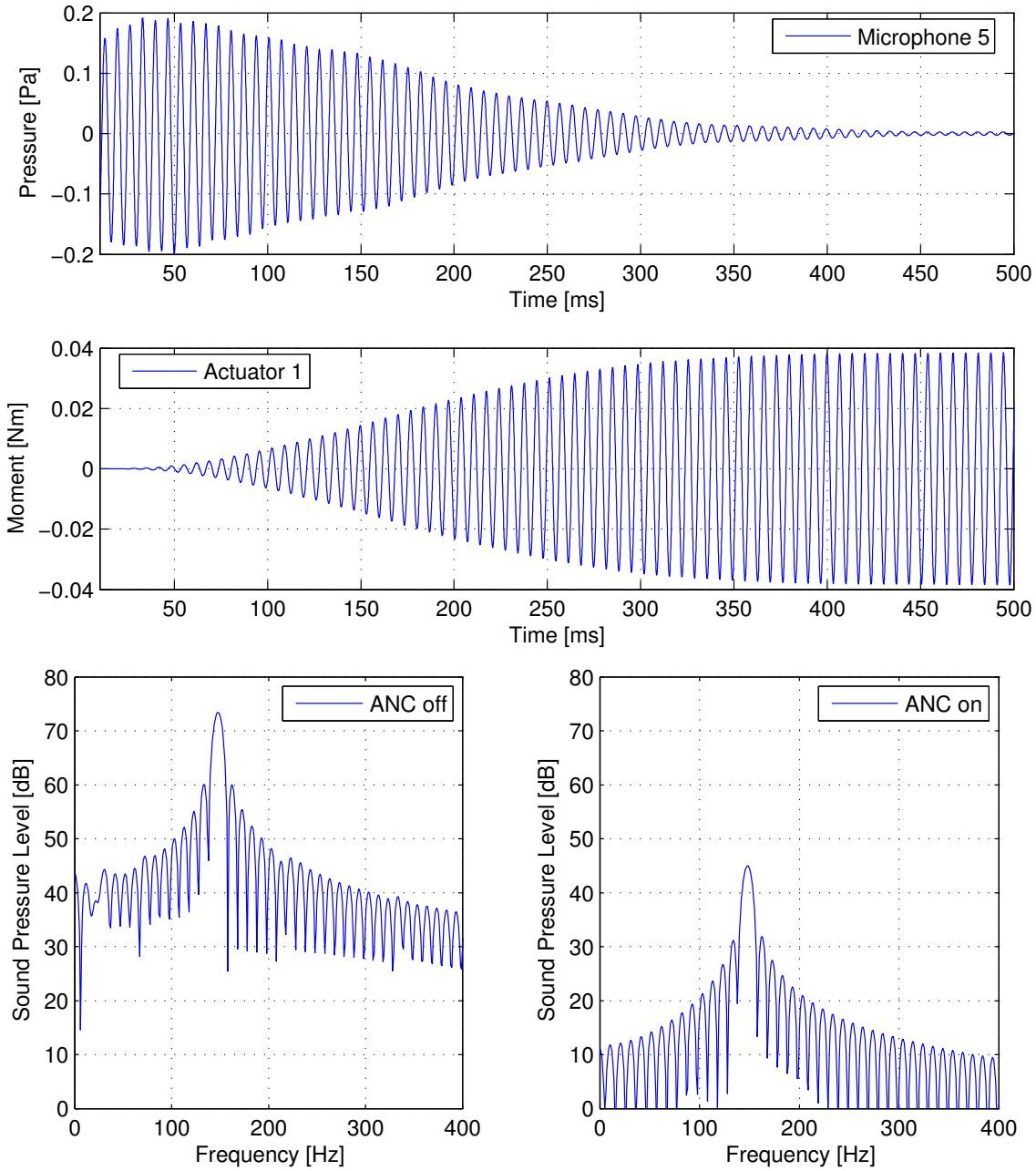

Figure 6.27: *Upper half*: The simulated harmonic signals at the central error position (upper axis) and the output signal on central actuator 1 (lower axis) during the first 500 ms of ANC. *Lower half*: Sound power levels of the simulated central microphone signal with ANC off (left) and ANC on (right). A reduction of approx. 27 dB is reached. The different shape of the peak compared to the one of the experiment in Fig. 6.17 is only due to the shorter time window used. For these figures only the top of the peak should be considered.

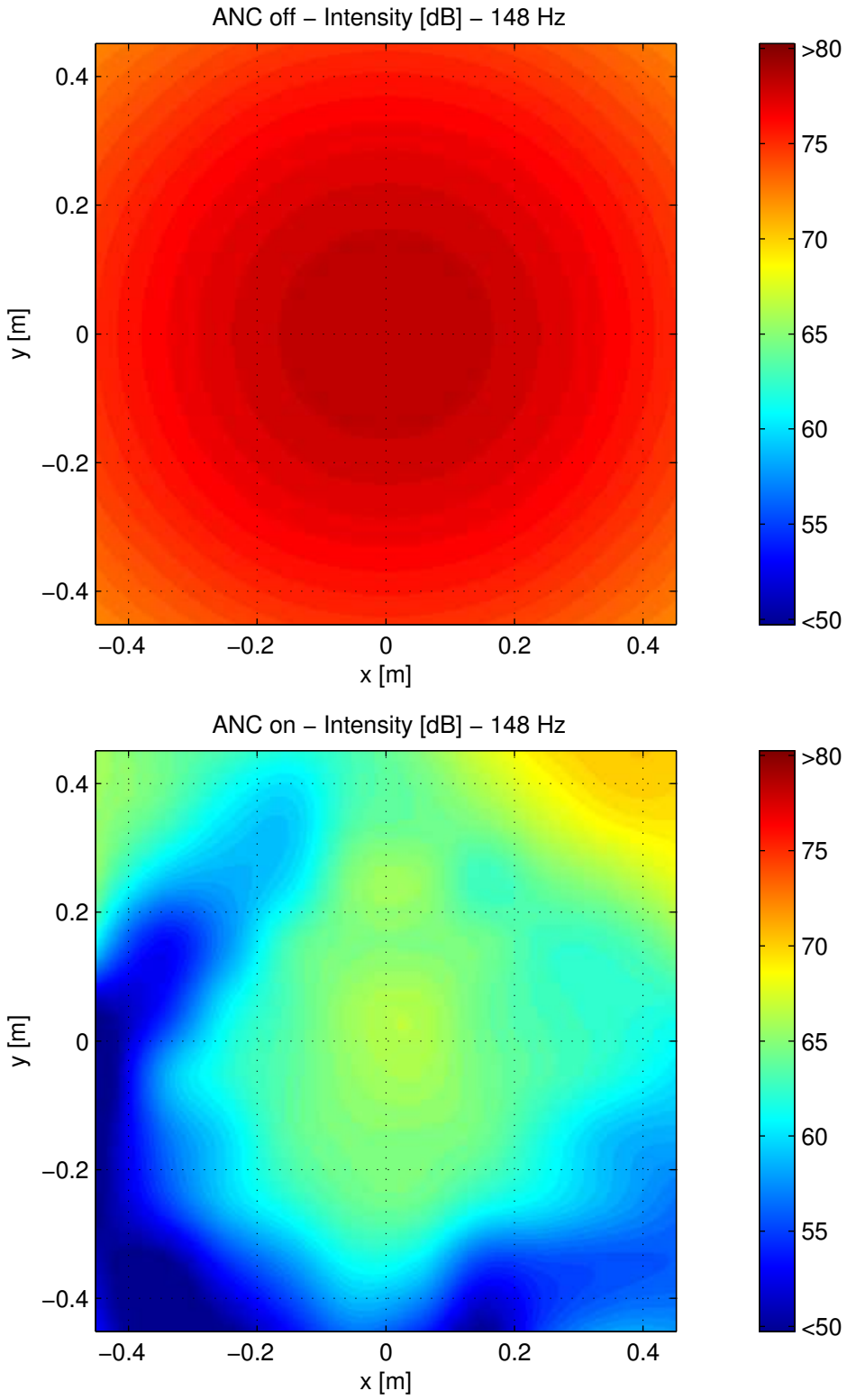

Figure 6.28: Intensity distribution over the plate for 148 Hz with active control turned off (upper figure) and turned on (lower figure). Compare with the measurement results shown in Fig. 6.18.

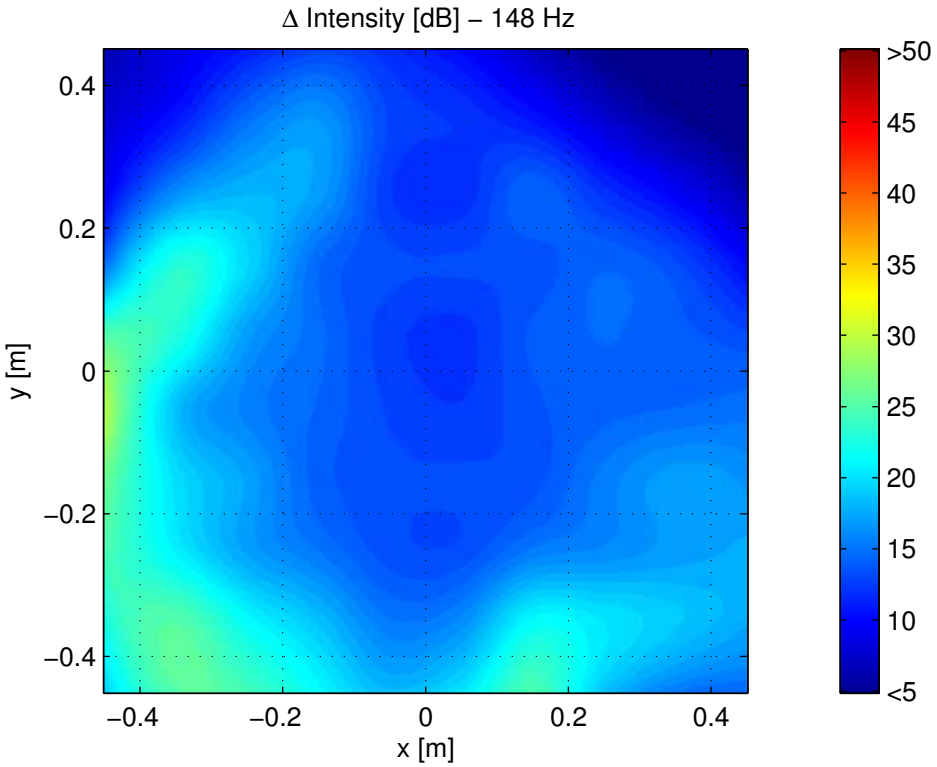

Figure 6.29: Intensity difference between active noise control off and on for FEM simulation (Fig. 6.28).

Sweep excitation

For the simulations with sweep noise, the plane wave sources sent out a sinusoidal signal inclining from 50 to 500 Hz within 25 s, just like the sweep experiments previously discussed. In the upper plot of Fig. 6.30 the average reduction for all five microphones can be seen as a spectrogram.

Instead of the higher noise reduction for the tonal simulations, now the results are more or less in the same dimension as the experiments (Fig. 6.20 & 6.21). For some frequency regions the reduction is about 8 dB. For other frequencies the reduction is negligible or even negative, the same as with the experiments. Again noticeable is that the reduction is more evenly spread over the entire spectrum compared to the experiment result. Also there seems to be a better reduction of resonances in the upper half of the frequency spectrum. This can be seen from the horizontal lines at the right side of the sweep line. This better reduction can be explained from the tonal noise results: the ANC algorithm in the simulation does need its time to find an optimum solution, but if found, the reduction is better than we have seen with the experimental set-up.

The corresponding transmission loss data (see Fig. 6.31) confirms that a wider frequency span of reduction is reached for the simulations compared to the experiments. For both the experiment as well as the simulation the strong low frequency resonance below 100 Hz is reduced with about 3 to 4 dB.

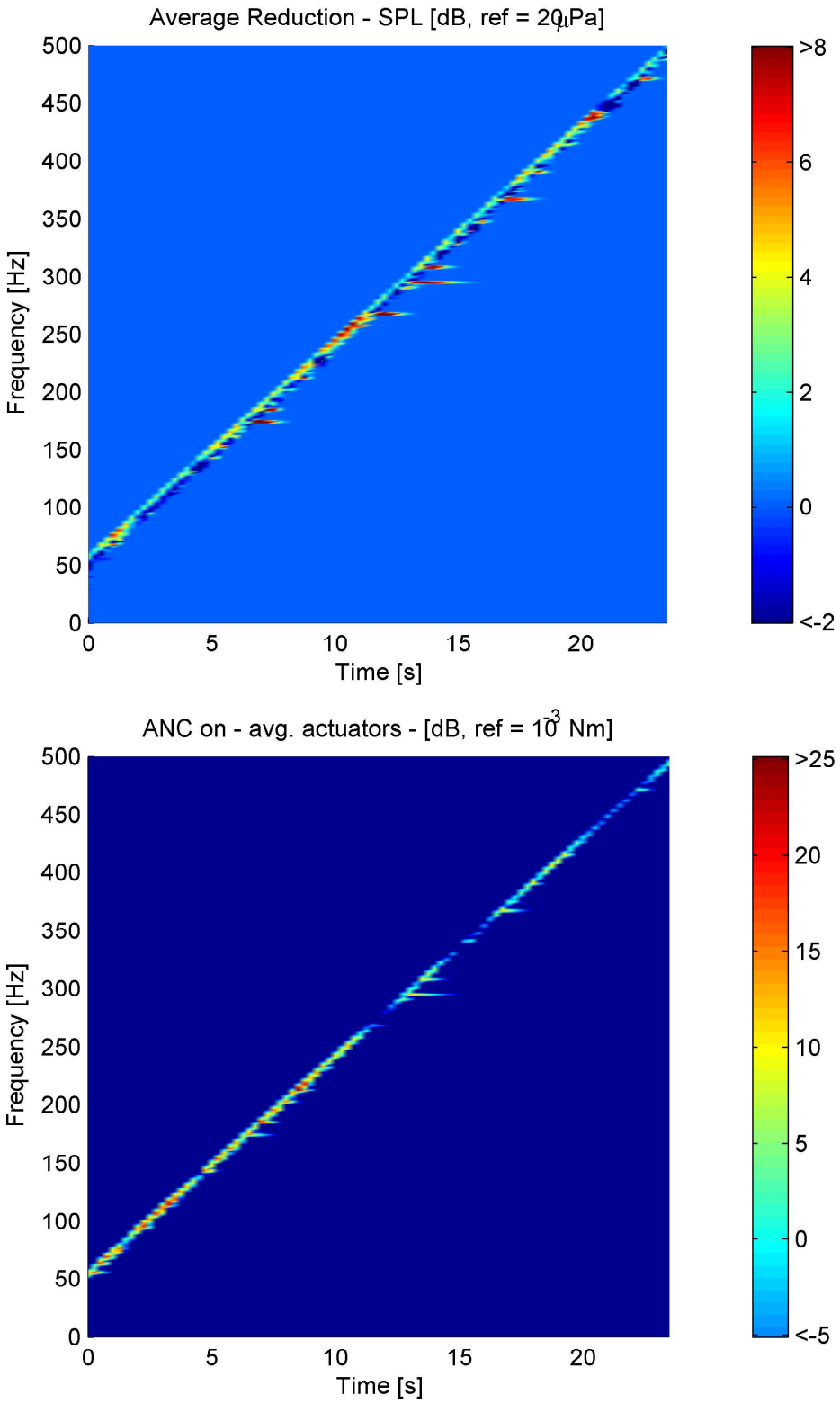

Figure 6.30: *Upper figure*: Average reduction of the five microphone positions due to active noise control in the form of a spectrogram. *Lower figure*: Average output (moment) at the three actuator positions during ANC.

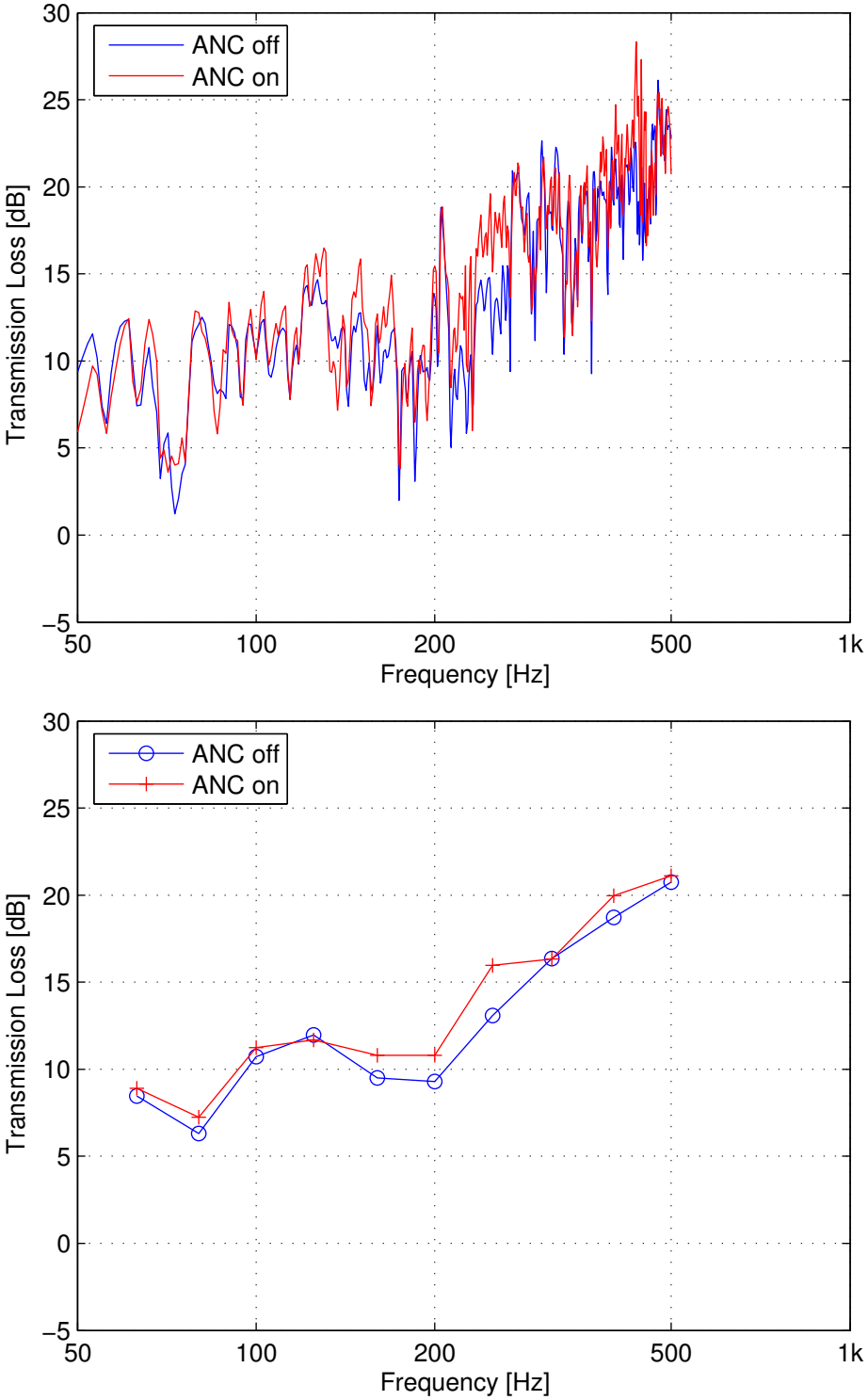

Figure 6.31: *Upper figure*: Simulated transmission loss for with and without ANC with as source signal a sweep function. *Lower figure*: The same but in 1/3-octave bands.

6.5 Conclusions

This chapter showed the results of the modal analyses and the passive and active transmission loss experiments and simulations. Some results have been conform the expectations; for other results we have seen differences between experiment and simulation.

The analytical and numerical modal analyses showed us that, using our fine enough mesh, the simulation is in very good accordance with the analytical theory. Of the experimentally found natural frequencies and shapes, about half of them fit quite well within the list of calculated modes. The others could not be identified as being the symmetrical modes that the theory predicts. Not uniform-enough boundary conditions and interference between modes close to each other have been mentioned as possible causes, but cannot explain why some important low-frequency modes were not found. A less square plate could improve results, reducing the interference between different mode shapes with nearby resonance frequencies. Also a finer frequency resolution than the $\Delta f = 1$ Hz used would make it lighter to distinguish resonances with close by frequencies. Contact-free acceleration measurements like a laser (scanning) vibrometer could improve results to some extent, but simulations have shown that the frequency shifts due to the accelerometer masses on the plate are small. From the experimental modal results the damping factors have been extracted and used in the transient simulation equation of motion.

From the transmission loss measurements that have been carried out, the 1/3-octave band results are used to obtain correction factors to transform our five-microphone measurement results into transmission loss values. Applying this correction we can compare the narrowband results with different general analytical predictions mentioned in the theory. Also a comparison has been made between the transmission loss of an aluminium plate, an aluminium plate with foam isolation and a steel plate. All results were more or less conform the expectations.

The simulations on passive transmission loss performed next showed us that it is possible to simulate the procedure of measuring the transmission loss by using the transient finite element method without air elements. The averages of the incoming pressure waves (normal or random incident) and of the receiving microphone signals are used to calculate the results. The narrowband differences between measurement and simulation results can be mainly accredited to either the presence or the absence of certain structural modes. Also above a certain frequency limit the error with the measurement increased and numerical factors as sampling rate and element size have been mentioned as possible causes.

Third and biggest part of this chapter is about active noise control. Using this technique it has been tried to reduce the sound that is transmitted through the partition. These investigations have been executed with three difference noise signals: white noise, tonal noise and a sweep.

The ANC experiment with white noise showed that the controller is able to follow and reduce the highest peaks on the side of the error microphones. This reduction is however only limited, not because of certain actuators power limitations, but because the controller is not able to *predict* the propagating noise more accurate.

Using tonal noise in a steady state situation we have full predictability of the noise arriving at the error microphones. This consequently leads to more reduction once the controller is turned on and adapted to the situation. As soon as this stable situation is reached, it is found that still a small fraction of the tonal noise arrives at the error microphone area. Measuring the radiated intensity over the complete plate, it is found that the upper part of the plate, the area on which no actuator has been attached, is still transmitting and radiating noise. Being unable to control that part of the plate well limits the ANC reduction possibilities for this set-up.

Using a sweep function as a noise source signal the ANC capabilities are tested for tonal noise with changing frequency. The results show that reduction is not as high as for the steady state situation with tonal noise. The time that the controller used to adapt to the changing tonal noise was too long to achieve the same results for a single constant tone. For some frequencies the controller seemed to be able to adapt quicker than for others.

In the plate's simulation model a virtual controller has been implemented trying to actively increase the transmission loss inside the simulation. This is done by introducing variable bending moments at the actuator positions. Before noise control, the impulse responses from all actuators to all error positions need to be determined and it has been showed that this can be done very efficiently by using delta pulses as source signals.

Similar to the experiment with random incident white noise, the simulation also showed that the reduction is limited and only present in a few frequency areas. White noise at the source side is highly unpredictable. Only in situations with long (1-dimensional) acoustic ducts, there is a chance of reducing such a noise type actively. In our situation, the broadband noise travels through a plate with its own resonances. Some frequency components travel through the plate without reduction, other frequencies are damped. The noise at the radiating side of the plate can be seen as white noise filtered with the transfer function of the plate. The more tonal character the noise has, the higher chance of reducing the noise arriving at the error microphones.

Compared to the corresponding experiment the simulation with tonal noise showed a higher reduction. Causes might be, among others, that the simulated set-up did not have background noise. Also could be seen from the radiated intensity plots that the extremes between maximum and minimum reduction over the plate's surface were smaller than for the experiment. And so we can say that the simulated actuators had a wider range of influence on the plate vibrations than the real ones.

Last simulation discussed was the simulation with a sweep function as noise signal. The reduction during this simulation was in the same order as the experimental one. A difference noticed was that the simulation was better able to handle some frequencies, which is shown in the form of horizontal stripes in the spectrogram. It also slightly better handled the higher frequencies, an aspect seen for all simulations and probably due to the higher frequency limit of the simulations compared to the real controller.

Chapter 7

Summary

In this thesis the reduction of sound transmitted by a plate using active noise control has been investigated. Both an experimental set-up as well as a simulation model have been developed to be able to predict the transmission loss, without and with active noise control.

In the experimental set-up the 1 mm aluminium plate of our investigation has been built between a reverberation room on the source side and an anechoic room on the receiver side. The reverberation room contains two source loudspeakers and a rotating arm with a microphone to determine the average sound intensity of the diffuse sound field. Using an intensity probe the radiated intensity at the output side has been measured to determine the plate's transmission loss. The hardware used for the active part were a controller, a reference microphone in front of the plate in the reverberation room, five error microphones at 1.5 m behind the plate in the anechoic room and as actuators three piezo-electric patches that were attached to the plate.

The developed finite element model consisted out of plate elements only and did not contain any air elements. The acoustic radiation towards and from the plate was calculated during the pre- and post-processing phases. To determine the noise input, the random incidence character of the diffuse sound field has been simulated by the sum of a large amount of plane waves with random angle, distance and signal. The advantage of the air-free model is that solving the equation of motion does not take too much time and transient simulations are practicable. This gives us the possibility to implement a time-dependent active noise control algorithm without getting a too slow model. The disadvantage of an air-free model is that possible plate-air coupling has not been considered.

Similar to the real controller, the active part of the simulation model contained a filtered-reference algorithm (FxLMS). The algorithm can be integrated into our time-domain simulation rather efficiently using matrix calculations. However, not all calculation steps can be executed with efficient matrix multiplications: some reordering and making use of

calculation loops was necessary. To reduce the overall calculation time, the ANC algorithm has not been executed during every time-step. The relatively high sample rate of the FE simulation allowed us to only execute the FxLMS procedure every fourth step in time. Negative consequence of this calculation reduction is that extra anti-aliasing and up-/down sampling calculations are needed.

The experimental and numerical investigations that have been executed can be divided into three parts: modal analysis, passive transmission loss and active transmission loss.

The first part, the modal analysis, showed that some modes that could be determined experimentally match the numerical results quite well. Other modes that were found could not be named, this because they did not have the straightforward (N_x, N_y)-layout. Causes might be the non-uniformity of plate and boundary conditions, as well as the fact that for a (nearly) square plate some resonance frequencies are so close to others that the modes mix and can not be identified independently. To prevent this, a smaller plate of different shape and with more focus on a uniform boundary condition could be investigated. A disadvantage will be that certified transmission loss measurements require a large enough plate and comparison with other transmission loss measurements can only be done for partitions with the same uniform size.

The second part of the investigation, the passive transmission loss experiments and simulations, have shown that it is generally possible to use the described simulation set-up as a transmission loss prediction tool. Looking at the narrow band results, the lines are not exactly the same. This is probably caused by differences between the plate and the plate's model, as well as possible excitation differences between reverberation room and the used diffuse sound field simulation. A possible solution for the first problem has been briefly discussed above and was about a rectangle but non-square plate and better boundary handling. The problem of noise excitation differences a further investigation of the sound field in reverberation room and inside the model would be interesting. Using the scanning robot arm that is located at the radiation side of the baffle, an "image" of the incident sound field could be made and compared to or used for the simulations.

The third part dealt with the investigations into the instrument of active noise control to increase the transmission loss through the plate. Both the experiments as well as the simulations showed a strong dependency on the *predictability* of the incident sound. For broadband noise the reduction was small and only around some resonance frequencies of the plate; for tonal noise the transmission loss increased much more using ANC, only limited by the maximum number of three actuators. The active tonal reduction was significantly higher for the simulations than for the experiments. Investigating the radiating intensity over the plate's surface confirmed that the simulated actuators seemed to have a larger working area than the real ones and were therefore better able to control the en-

tire plate. Sweep signal experiments showed a moderate reduction which was in between broadband and tonal noise, both for the experiments as well as the simulations.

The prediction of transmission loss values for certain materials and structures is more and more requested by the industry. At the moment two approaches are commonly used: Statistical Energy Analysis (SEA) and a combination of the Boundary Element Method (BEM) and the Finite Element Method (FEM). The last one, in which an FE model is imported into the BEM simulation and the radiation is calculated by using the surface vibration information, resembles the method which is proposed in this dissertation. The FEM-BEM combination used in the often used software LMS Sysnoise is able to do transient simulations, but unfortunately does not allow extensive in-loop calculations like an ANC algorithm.

Due to the decreasing structural wavelengths for increasing frequencies, the finite element techniques available are only usable for the lower frequency spectrum. The SEA approach is more reliable for higher frequencies, because it assumes a high modal density (Norton [42]). Due to the relatively high frequencies and statistical character, an ANC algorithm integration for this method is not realisable either.

In general we can say that usage of active noise control to increase the passenger's comfort is a promising technique, but has its limits. In the investigations we have seen that high-frequencies, broadband noise with low modal character and fast-changing tonal noise have a negative impact on the controller's performance. Before testing the set-up in a real vehicle, it's behaviour could be investigated using recorded vehicle noise for different engine states. With the reverberation room being more diffuse than an engine compartment, the reduction will most probably be not as high as it could be in the real vehicle.

In a possible vehicle or aircraft integration, the heavy laboratory equipment of course needs to be replaced by lightweight hardware. Without this step the advantage of ANC above normal acoustic isolation techniques would be gone. This hardware has to be especially designed for that specific purpose and application. The commercially available head phones with microphones and active controller show that this hardware minimisation is technically possible.

Using ANC as an instrument to reduce the noise coming from the vehicle's engine, the tire-road contact and the wind-body interaction will be the most challenging; using ANC to reduce low-frequency vehicle resonances is the most realistic one. Truck drivers suffer from strong cabin modes and so called beat noise from engine driven components while driving long hours at monotone speeds. The noise exposure significantly contribute to the drivers physical fatigue and, consequently, reduces traffic safety (Bein [7]). These effects can be reduced using active control; not the ANC algorithms but the development of

intelligent materials that are able to produce the required anti-noise and -vibration will be the most interesting part.

In aviation, propeller or rotor driver aircraft suffer from strong low-frequency tonal noise and vibrations. Usually the blades' profiles are aerodynamically optimised, not taken into account the acoustic properties (Breitbach [13]). First, passive measures are taken to reduce noise and vibration for passengers and payload, but the general problem is that low-frequency noise requires too much extra damping weight. To comply to noise and vibration safety regulations, (semi-)active systems seem to be the best solution.

In this thesis the focus has mainly been laid on interior noise exposure. Another field which is at least as important is the exterior noise of traffic. Where the interior noise reduction efforts mainly have economical motives (the customer prefers to travel in a quiet vehicles or aircraft), the exterior noise radiation for people that live close to roads and/or airports as been more or less neglected. This although long exposure to certain types of noise can cause stress and illness.

Growing cities and growing transportation require strict noise regulations. When, for example, an airport will restrict the landing of loud airplanes, an economical motive is there to reduce the exterior aircraft noise. Although newer airplanes are generally quieter than older ones, it does not automatically mean that living close to a runway is less noisy these days; for an airport a quiet airplane means that more take-offs and landings can take place before reaching the daily noise limit.

Taken into account the sensitivity of the human ear (or better: the insensitivity of the human ear for very low frequencies) an ANC system could be configured in such a way that it maximises the noise reduction as it is perceived by the passenger by using weighted filters ([31]). This would reduce the focus of the controller on low frequencies and therefore reduce the problem that many lightweight actuator have: lack of power in the low frequency area.

Fatigue is an important safety aspect in especially aircraft constructions. Long time exposure of materials to vibrations can cause cracks and failure, a thing that should be prevented by all means. In the design of active noise control systems it should be considered that reducing the passengers noise in e.g. an airplane cabin by actuators on the fuselage not automatically implies less surface vibrations. The other way around, minimising the fuselage vibrations does not automatically mean that the noise that is perceived by the passengers is minimised.

With the investigations discussed in this thesis it is shown that structural mechanics, acoustics and control algorithms can be integrated into one simulation. Now a prediction can be made about the noise reduction influence of material properties and constructions, as well as the effectiveness and stability of ANC algorithm parameters.

Appendix A

Modal participation

As we have seen in paragraph 2.2.2 there are usually more then one solutions to an eigenvalue problem. The analytical situation of Eq. 2.28 has a list of mode shapes and so has the solution of the FEM eigenvalue problem of Eq. 4.22. To be able to compare different FE mode shapes with each other they are generally normalised towards the mass matrix as follows:

$$\tilde{\boldsymbol{\phi}}_i = \frac{\boldsymbol{\phi}_i}{\sqrt{\boldsymbol{\phi}_i{}^{\mathrm{T}} \boldsymbol{M}\, \boldsymbol{\phi}_i}} \tag{A.1}$$

with for $\tilde{\boldsymbol{\phi}}_i$ the i^{th} normalised mode shape. Normalised to the mass matrix means that the following can be said for every i:

$$\tilde{\boldsymbol{\phi}}_i^{\mathrm{T}} \boldsymbol{M} \tilde{\boldsymbol{\phi}}_i = 1 \tag{A.2}$$

Using the weight factors β_i we can write any displacement state of the plate, for example $\boldsymbol{u}(x, y)$, as a summation of mode shapes (Cremer [17]):

$$\boldsymbol{u}(x, y) = \sum_i \beta_i \tilde{\boldsymbol{\phi}}_i. \tag{A.3}$$

In case we are dealing with a steady state transient situation, the (time-dependent) weight factor β_i is not complex but is a sinusoid with certain amplitude and phase and with the same frequency ω as the load signal.

Combining the equations above with the equation of motion of Eq. 4.19 we get:

$$\boldsymbol{M} \sum_i \ddot{\beta}_i \tilde{\boldsymbol{\phi}}_i + \boldsymbol{B} \sum_i \dot{\beta}_i \tilde{\boldsymbol{\phi}}_i + \boldsymbol{K} \sum_i \beta_i \tilde{\boldsymbol{\phi}}_i = \boldsymbol{f}_{\text{ext}}. \tag{A.4}$$

If we pre-multiply this equation with a different mode shape called $\tilde{\boldsymbol{\phi}}_j$ we get:

$$\tilde{\boldsymbol{\phi}}_j^{\mathrm{T}} \boldsymbol{M} \sum_i \ddot{\beta}_i \tilde{\boldsymbol{\phi}}_i + \tilde{\boldsymbol{\phi}}_j^{\mathrm{T}} \boldsymbol{B} \sum_i \dot{\beta}_i \tilde{\boldsymbol{\phi}}_i + \tilde{\boldsymbol{\phi}}_j^{\mathrm{T}} \boldsymbol{K} \sum_i \beta_i \tilde{\boldsymbol{\phi}}_i = \tilde{\boldsymbol{\phi}}_j^{\mathrm{T}} \boldsymbol{f}_{\text{ext}}. \tag{A.5}$$

The normalised mode shapes are orthogonal and this means that:

$$\tilde{\boldsymbol{\phi}}_j^{\mathrm{T}} \tilde{\boldsymbol{\phi}}_i = \begin{cases} 1, & i = j \\ 0, & i \neq j, \end{cases}$$

which results into the following equation:

$$\ddot{\beta}_j \tilde{\boldsymbol{\phi}}_j^{\mathrm{T}} \boldsymbol{M} \tilde{\boldsymbol{\phi}}_j + \dot{\beta}_j \tilde{\boldsymbol{\phi}}_j^{\mathrm{T}} \boldsymbol{B} \tilde{\boldsymbol{\phi}}_j + \beta_j \tilde{\boldsymbol{\phi}}_j^{\mathrm{T}} \boldsymbol{K} \tilde{\boldsymbol{\phi}}_j = \tilde{\boldsymbol{\phi}}_j^{\mathrm{T}} \boldsymbol{f}_{\mathrm{ext}}. \tag{A.6}$$

Splitting up the damping matrix $\boldsymbol{B}$ as in Eq. 4.17, this becomes:

$$(\ddot{\beta}_j + \alpha_1 \dot{\beta}_j) \tilde{\boldsymbol{\phi}}_j^{\mathrm{T}} \boldsymbol{M} \tilde{\boldsymbol{\phi}}_j + (\beta_j + \alpha_2 \dot{\beta}_j) \tilde{\boldsymbol{\phi}}_j^{\mathrm{T}} \boldsymbol{K} \tilde{\boldsymbol{\phi}}_j = \tilde{\boldsymbol{\phi}}_j^{\mathrm{T}} \boldsymbol{f}_{\mathrm{ext}}. \tag{A.7}$$

Taking into account Eq. A.2 and applying the following eigenvalue equation:

$$\boldsymbol{K} \tilde{\boldsymbol{\phi}}_j = \omega_j^2 \boldsymbol{M} \tilde{\boldsymbol{\phi}}_j,$$

we can simplify Eq. A.7 into:

$$\ddot{\beta}_j + (\alpha_1 + \alpha_2 \omega_j^2) \dot{\beta}_j + \omega_j^2 \beta_j = f_j \tag{A.8}$$

with for f_j:

$$f_j = \tilde{\boldsymbol{\phi}}_j^{\mathrm{T}} \boldsymbol{f}_{\mathrm{ext}}.$$

Because of the harmonic properties of the modal participation factors β_i, we can write its derivatives as follows:

$$\begin{aligned} \dot{\beta}_j &= \mathrm{j}\Omega\beta_j \\ \ddot{\beta}_j &= -\Omega^2\beta_j \end{aligned}$$

with for Ω the (angular) frequency of interest. Filling this in into Eq. A.8, it becomes:

$$\left[-\Omega^2 + 2\mathrm{j}\left(\alpha_1 + \alpha_2 \omega_j^2\right)\Omega + \omega_j^2\right] \beta_j = f_j \tag{A.9}$$

and this leads to the equation for the complex participation of mode shape j with angular frequency ω_j at an external load with frequency Ω:

$$\beta_j = \frac{f_j}{\left(\omega_j^2 - \Omega^2\right) + 2\mathrm{j}\left[\left(\alpha_1 + \alpha_2 \omega_j^2\right)\Omega\right]}. \tag{A.10}$$

Appendix B

Shape functions

A local coordinate system (x, y, z) with origin in the center of the element is assumed and the displacement at a point (x, y) on the element is called $u_z^{(e)}$ (see Fig. 4.2 and B.1). This displacement can be determined by interpolating between the displacements of the four element's nodes $u_z^{(1)}$ to $u_z^{(4)}$ (Beer et al. [6]):

$$u_z^{(e)} = \sum_{m=1}^{4} N^{(m)} \; u_z^{(m)} \tag{B.1}$$

where the functions $N^{(m)}$ are called the *shape functions*:

$$\begin{aligned} N^{(1)} &= \tfrac{1}{4}(1 - \tfrac{2x}{L_1})(1 - \tfrac{2y}{L_2}) \\ N^{(2)} &= \tfrac{1}{4}(1 + \tfrac{2x}{L_1})(1 - \tfrac{2y}{L_2}) \\ N^{(3)} &= \tfrac{1}{4}(1 + \tfrac{2x}{L_1})(1 + \tfrac{2y}{L_2}) \\ N^{(4)} &= \tfrac{1}{4}(1 - \tfrac{2x}{L_1})(1 + \tfrac{2y}{L_2}). \end{aligned}$$

The property L_1 is the length of the element in the x-direction and L_2 the length in the y-direction.

Similar to the displacement, the element functions for the rotations, $\theta_x(x, y)$ and $\theta_y(x, y)$, can be created:

$$\begin{aligned} \theta_x^{(e)} &= \sum N^{(m)} \; \theta_x^{(m)} \\ \theta_y^{(e)} &= \sum N^{(m)} \; \theta_y^{(m)}. \end{aligned} \tag{B.2}$$

Although the element's nodes only have a displacement degree of freedom in the z-direction, it does not mean that a point somewhere in the element can not have a displacement in the x- or y-direction. Due to bending, we can use Eq. B.2 and express the

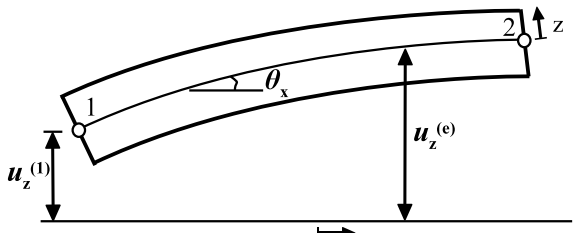

Figure B.1: Side view of the shell element.

displacements $u_x^{(e)}$ and $u_y^{(e)}$ as (Beer at al. [6]):

$$\begin{aligned} u_x^{(e)} &= \theta_y^{(e)} z \\ u_y^{(e)} &= -\theta_x^{(e)} z \end{aligned} \tag{B.3}$$

with z being the axis along the normal of the surface of the element and $z = 0$ for the midsurface (see Fig. B.1).

Appendix C

The strain-displacement matrix

Using Eq. B.1 - B.3 we can write the strains in terms of the shape functions and therefore in terms of the nodal displacement and rotations. As an example, the strain ϵ_x is given:

$$\epsilon_x = \frac{\partial u_x}{\partial x} = z\frac{\partial \theta_y^{(\mathrm{e})}}{\partial x} = z\sum\left(\frac{\partial N^{(m)}}{\partial x}\theta_y^{(m)}\right) \tag{C.1}$$

and so, writing out every element in Eq. 4.12, we can change the summation into a matrix multiplication:

$$\boldsymbol{\epsilon} = \boldsymbol{T}\boldsymbol{u} \tag{C.2}$$

with for $\boldsymbol{u}$ the nodal displacement vector as in Eq. 4.8 and $\boldsymbol{T}$ is the *strain- displacement matrix* with dimension 5×12 containing all partial derivatives of N:

$$\boldsymbol{T} = z\cdot$$

$$\begin{bmatrix}
0 & 0 & \frac{\partial N^{(1)}}{\partial x} & 0 & 0 & \frac{\partial N^{(2)}}{\partial x} & 0 & 0 & \frac{\partial N^{(3)}}{\partial x} & 0 & 0 & \frac{\partial N^{(4)}}{\partial x} \\
0 & \frac{-\partial N^{(1)}}{\partial y} & 0 & 0 & \frac{-\partial N^{(2)}}{\partial y} & 0 & 0 & \frac{-\partial N^{(3)}}{\partial y} & 0 & 0 & \frac{-\partial N^{(4)}}{\partial y} & 0 \\
0 & \frac{-\partial N^{(1)}}{\partial x} & \frac{\partial N^{(1)}}{\partial y} & 0 & \frac{-\partial N^{(2)}}{\partial x} & \frac{\partial N^{(2)}}{\partial y} & 0 & \frac{-\partial N^{(3)}}{\partial x} & \frac{\partial N^{(3)}}{\partial y} & 0 & \frac{-\partial N^{(4)}}{\partial x} & \frac{\partial N^{(4)}}{\partial y} \\
\frac{\partial N^{(1)}}{z\partial y} & -\frac{N_1}{z} & 0 & \frac{\partial N^{(2)}}{z\partial y} & -\frac{N_2}{z} & 0 & \frac{\partial N^{(3)}}{z\partial y} & -\frac{N_3}{z} & 0 & \frac{\partial N^{(4)}}{z\partial y} & -\frac{N_4}{z} & 0 \\
\frac{\partial N^{(1)}}{z\partial x} & 0 & \frac{N_1}{z} & \frac{\partial N^{(2)}}{z\partial x} & 0 & \frac{N_2}{z} & \frac{\partial N^{(3)}}{z\partial x} & 0 & \frac{N_3}{z} & \frac{\partial N^{(4)}}{z\partial x} & 0 & \frac{N_4}{z}
\end{bmatrix}$$

Appendix D

The flexibility matrix

In the strain-stress relationship of Eq. 4.13,

$$\begin{aligned} \boldsymbol{\sigma} &= \boldsymbol{D}\boldsymbol{\epsilon}, \\ \boldsymbol{\epsilon} &= \boldsymbol{D}^{-1}\boldsymbol{\sigma}, \end{aligned} \tag{D.1}$$

the matrix $\boldsymbol{D}$ transforms from strain to stress and $\boldsymbol{D}^{-1}$ vice-versa. Taking into account that we neglect the normal strain and stress in the z-direction, for an isotropic material $\boldsymbol{D}^{-1}$ becomes (MacNeal [38]):

$$\boldsymbol{D}^{-1} = \begin{bmatrix} 1/E & -\nu/E & 0 & 0 & 0 \\ -\nu/E & 1/E & 0 & 0 & 0 \\ 0 & 0 & 1/G & 0 & 0 \\ 0 & 0 & 0 & 1/G & 0 \\ 0 & 0 & 0 & 0 & 1/G \end{bmatrix} \tag{D.2}$$

with for G the shear modulus:

$$G = \frac{E}{2(1+\nu)}.$$

Appendix E

Modal analysis results

Graphical results of experimental modal analysis. The amplitude data is plotted in two colours and pasted over a picture of the plate and baffle. The frequency and damping results can also be found in Table 6.1.

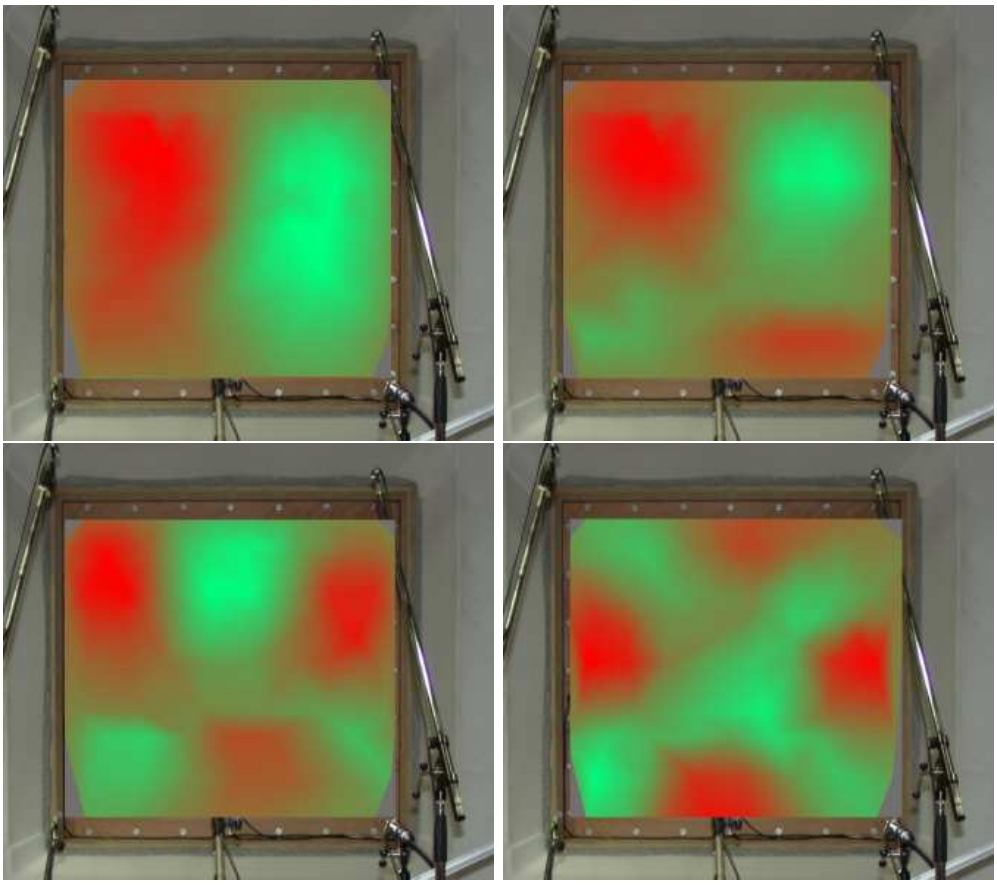

Figure E.1: *Upper left*: Mode (2,1), 15.2 Hz *Upper right*: Mode (2,2), 20.2 Hz *Lower left*: Mode (3,2), 36.6 Hz *Lower right*: Mode (3,3), 50.5 Hz.

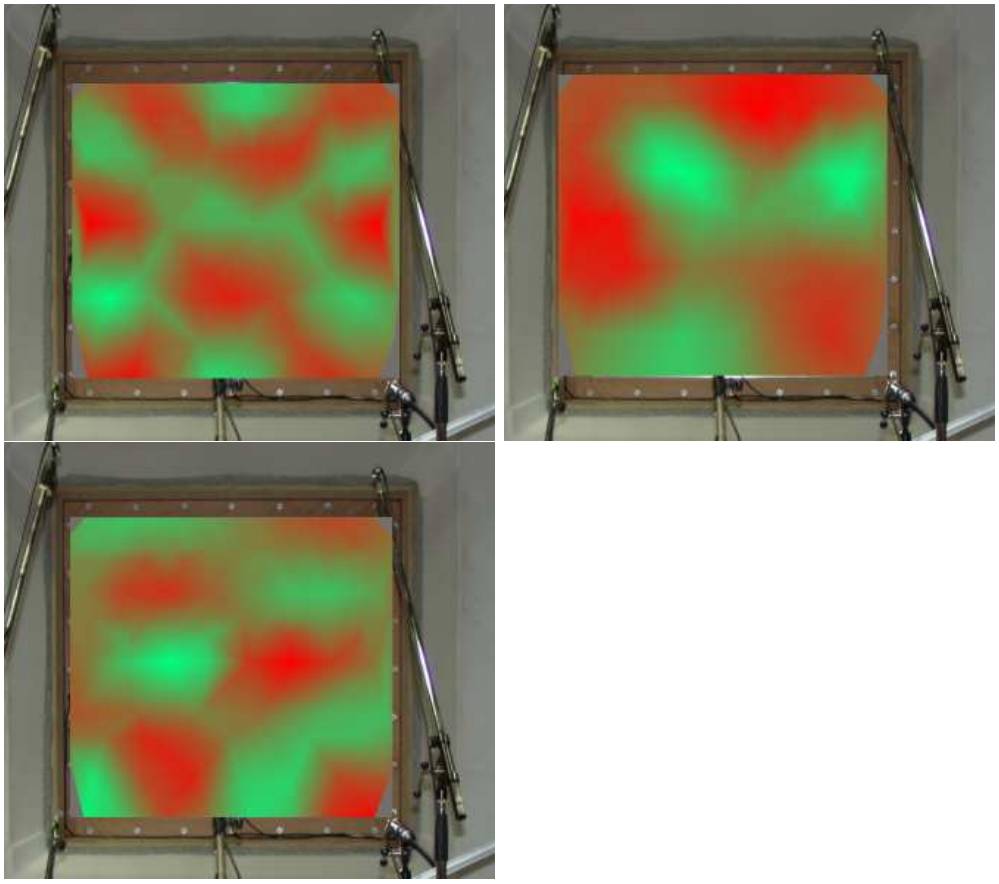

Figure E.2: *Upper left*: Mode (4,2), 52.4 Hz. *Upper right*: More (4,4), 90.4 Hz *Lower left*: Mode (5,2), 96.3 Hz.

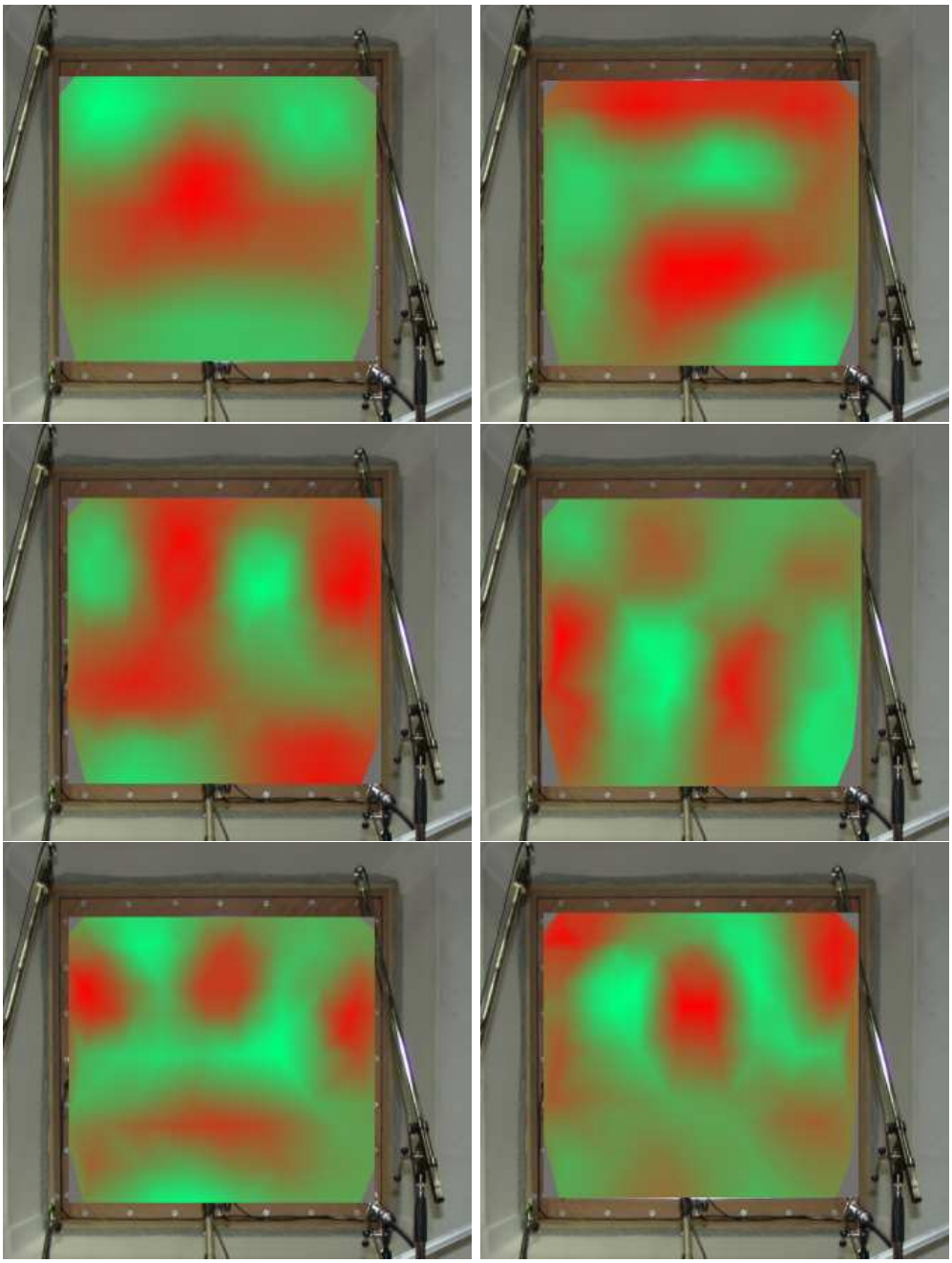

Figure E.3: *Upper left*: 44.5 Hz *Upper right*: 55.5 Hz *Center left*: 59.5 Hz *Center right*: 75.7 *Lower left*: 84.1 Hz *Lower right*: 86.7 Hz.

Bibliography

[1] Lutz Ackermann. *Simulation der Schalltransmission durch Wände.* Dissertation, Technische Universität Braunschweig, 2002.

[2] W. Akl and Amr Baz. Active vibration and noise control using smart foam. *Journal of Vibration and Control*, 12(11):1173–1203, 2006.

[3] Moustafa Al-Bassyiouni and B. Balachandran. Sound transmission through a flexible panel into an enclosure: structural-acoustic model. *Journal of Sound and Vibration*, 285:467–486, 2005.

[4] Ansys. *Ansys Multiphysics Theory Reference*, 2005.

[5] Klaus-Juergen Bathe. *Finite Element Procedures in Engineering Analysis.* Prentice-Hall Inc., New Jersey, USA, 1982.

[6] G. Beer and John O. Watson. *Introduction to Finite and Boundary Element Methods for Engineers.* John Wiley & Sons, 1992.

[7] Thilo Bein and Holger Hanselka. *The integrated project Intelligent Materials for Active Noise Reduction - An overview and first results.* 3rd Styrian Noise, Vibration and Harshness Congress, Graz, 2005.

[8] Leo L. Beranek. *Noise and Vibration Control.* Institute of Noise Control Engineering, 1971.

[9] Arthur P. Berkhoff and Niek J. Doelman. Efficient radiation mode sensing strategies for active structural acoustic control. *Proceedings of Active 99*, 1999.

[10] Augustinus J. Berkhout. *Applied Seismic Wave Theory.* Elsevier Science Publishers, Amsterdam, The Netherlands, 1987.

[11] Marinus M. Boone, Diemer de Vries, and Augustinus J. Berkhout. *Geluidsbeheersing/ Sound Control - Part 1.* Delft University of Technology, Delft, the Netherlands, 1995.

[12] Marinus M. Boone, Kees P.A. Wapenaar, and Diemer de Vries. *Grondslagen der Akoestiek - Lecture Notes.* Delft University of Technology, Delft, the Netherlands, 1994.

[13] Harald Breitbach, Delf Sachau, and Sten Böhme. Acoustic challenges of the A400M for active systems. *Smart Structures and Materials: Industrial and Commercial Applications of Smart Structures Technologies, Proceedings of SPIE*, 6171:25–32, 2006.

[14] Maarten C. Brink. The acoustic representation of bending waves. M.Sc. Thesis, Delft University of Technology, Delft, The Netherlands, 2002.

[15] Randolph H. Cabell. *A Principal Component Algorithm for Feedforward Active Noise and Vibration Control*. Dissertation, Virginia Polytechnic Institute and State University, 1998.

[16] James P. Carneal, F. Charette, and Chris R. Fuller. Minimization of sound radiation from plates using adaptive tuned vibration absorbers. *Journal of Sound and Vibration*, 270:781–792, 2004.

[17] Lothar Cremer and Manfred Heckl. *Körperschall: physikalische Grundlagen und technische Anwendungen*. Springer, 1996.

[18] Wouter Dehandschutter, Kris Henrioulle, and Paul Sas. Active control of sound transmission loss through a single panel partition using distributed actuators. part 2: Experiments. *International Conference on Noise and Vibration Engineering (ISMA23)*, 1998.

[19] Stephen J. Elliott. *Signal Processing for Active Control*. Academic Press, Lodon, UK, 2001.

[20] Otto von Estorff. *Boundary Elements in Acoustics: Advances and Applications*. WIT Press, Southampton, 2000.

[21] Frank J. Fahy. *Sound and Structural Vibration*. Academic Press Inc., London, UK, 1985.

[22] P. de Fonseca, Paul Sas, H. van Brussel, and Kris Henrioulle. Active reduction of sound tranismission through double panel partitions - a physical analysis of the observed phenomena. *International Conference on Noise and Vibration Engineering (ISMA25)*, 2000.

[23] Christopher R. Fuller. Active control of sound transmission/radiation from an elastic plate by vibration inputs: I. analysis. *Journal of Sound and Vibration*, 136(1):1–15, 1990.

[24] Christopher R. Fuller, Stephen J. Elliott, and Phil A. Nelson. *Active control of vibration*. London Academic Press, Lodon, UK, 1996.

[25] Jörg Hechenblaikner. *Aktive Lärmminderung in Transportsystemen durch randangeregte Flächenelmente*. Dissertation, Technische Universität Darmstadt, 2004.

[26] Kris Henrioulle, Wouter Dehandschutter, and Paul Sas. Active control of sound transmission loss through a single panel partition using distributed actuators. part 1: Simulations. *International Conference on Noise and Vibration Engineering (ISMA23)*, 1998.

[27] INA-Schäffler KG. *Technisches Taschenbuch.* Herzogenaurach, Germany, 2002.

[28] International Electrotechnical Commission. *IEC 61260:1995 - Electroacoustics - Octave-band and fractional-octave-band filters*, 1995.

[29] International Organisation for Standardization. *ISO 140-1 - Acoustics - Measurement of sound insulation in buildings and of building elements - Part 1: Requirements for laboratory test facilities with suppressed flanking transmission - Part 3: Laboratory measurements of airborne sound insulation of building elements*, 1995-1997.

[30] International Organisation for Standardization. *ISO 15186-1:2000 - Acoustics - Measurement of sound insulation in buildings and of buiding elements using sound intensity - Part 1: Laboratory measurements*, 2003.

[31] International Organisation for Standardization. *ISO 226:2003 - Acoustics - Normal equal-loudness-level contours*, 2003.

[32] International Organisation for Standardization. *ISO 354 2003 - Acoustics - Measurement of sound absorption in a reverberation room*, 2003.

[33] Rolf Isermann. *Identifikation dynamischer Systeme - Band I.* Springer-Verlag, Berlin, Germany, 1988.

[34] Finn Jacobsen. *The Sound Field in a Reverberation Room.* Technical University of Denmark, Copenhagen, Denmark, 2007.

[35] Brody D. Johnson and Christopher R. Fuller. Broadband control of plate radiation using a piezoelectric, double-amplifier active-skin and structural acoustic sensing. *Journal of the Acoustical Society of America*, 107(2):876–884,, 1999.

[36] Karl-Dirk Kammeyer and Kristian Kroschel. *Digitale Signalverarbeitung - Filterung und Spektralanalyse.* B.G. Teubner, Stuttgart, Germany, 2002.

[37] LMS International. *User Manual SYSNOISE Rev 5.6.* Leuven, 2002.

[38] Richard H. MacNeal. *The Nastran Theoretical Manual, MSR-40, Level 15.5.* The MacNeal-Schwendler Corporation, 1972.

[39] The Mathworks Inc. *Matlab - Signal Processing Toolbox User's Guide*, 1988.

[40] Midé Technology Corporation. *Factsheet ACX Quickpack actuators*, 2000.

[41] Nathan M. Newmark. A method of computation for structural dynamics. *Journal of Engineering Mechanics ASCE*, 8:67–94, 1959.

[42] Michael P. Norton and Denis G. Karczub. *Fundamentals of Noise and Vibration Analysis for Engineers*. Cambridge University Press, Cambridge, UK, 2003.

[43] Alan V. Oppenheim and Ronald W. Schafer. *Digital Signal Processing*. Prentice-Hall Inc., New Jersey, USA, 1975.

[44] Alan V. Oppenheim, Ronald W. Schafer, and Ian T. Young. *Signals and Systems*. Prentice-Hall Inc., New Jersey, USA, 1983.

[45] Marco Oude-Nijhuis and André de Boer. Finite element modelling approach in active structural acoustic control. *The 8th Mechatronics Forum International Conference, University of Twente*, 2002.

[46] Athanasios Papoulis. *Signal Analysis*. McGraw-Hill Book Company, New York, USA, 1984.

[47] Vipul Prakash, Graham H. Powell, and Scott D. Campbell. *DRAIN-2DX: Static and Dynamic Analysis of Inelastic Plane Structures*. University of California, Berkeley, USA, 1993.

[48] Maurice B. Priestley. *Spectral analysis and time series*. Academic Press, San Diego, USA, 1999.

[49] Boaz Rafaely. Spatial-temporal correlation of a diffuse sound field. *Journal of the Acoustical Society of America*, 107(6):3254–3258, 2000.

[50] Carol Z. Rosen, Basavarai V. Hiremath, and Robert Newnham. *Piezoelectricity*. American Institute of Physics, New York, 1992.

[51] Werner Soedel. *Vibrations of Shells and Plates*. Marcel Dekker Inc., New York, 1993.

[52] Stephan Tewes. *Active Trim Panel Attachments for Control of Sound Transmission through Aircraft Structures*. Dissertation, Technische Universität München, 2007.

[53] M.O. Tokhi and R.R. Leitch. *Active Noise Control*. Oxford University Press, Oxford, 1992.

[54] Gerrit Verkerk and Johan Broens. *Binas - Informatieboek vwo-havo voor het onderwijs in de natuurwetenschappen*. Wolters-Noordhoff Groningen, 1986.

[55] Vibro-Acoustic Sciences. *AutoSEA2 - Advanced Technology for Noise & Vibration Design - User's Guide*, 2001.

Acknowledgements

I would like to express my gratitude to the people that helped me in any way during my work for this dissertation. A special thanks goes to Dr. I.U. Borchers for giving me the opportunity to work for his department at DaimlerChrysler Research & Technology at EADS/Dornier in Friedrichshafen and allowing me to continue my work at the EADS Research Center in Ottobrunn. Also I owe a lot to Prof. Dr.-Ing. H. Hanselka and Prof. Dr.-Ing. R. Nordmann for giving me the possibility to present my work at the Technical University Darmstadt, as well as Dr.-Ing. R. Storm for his advices and his support during the last phase of my promotion.

Also a thanks goes to my colleagues at Dornier in Friedrichshafen and EADS in Ottobrunn, especially to Andreas Gündel for his introduction into the world of finite element simulation, Stefan Tewes for his instructions for measuring the transmission loss, Roland Uhlig and Ludwig Schauwecker for their general support during the past few years and my brother Wilbert Brink for the correction advises.

Curriculum Vitae

Personal Data

Name:	Brink
First Names:	Maarten Cornelis
Date of Birth:	11^{th} of October, 1976
Place of Birth:	Oss, The Netherlands
E-mail address:	maartenbrink@yahoo.com

Educational Career

1983 - 1989:	Basisschool St. Joseph, Berghem
1989 - 1995:	Titus Brandsma Lyceum, Oss *Degree: High School Diploma*
1995 - 2000:	Faculty of Applied Physics, Delft University of Technology *Degree: Bachelor of Science in Applied Physics*
2000 - 2002:	Acoustical Imaging and Sound Control, Delft Uni. of Tech. Degree: *Master of Science in Applied Physics*

Professional Career

03/2003 - 02/2006:	Ph.D. student / Scientific employee, DaimlerChrysler Research & Technology EADS Dornier GmbH, Friedrichshafen, Germany
03/2006 - 09/2006:	Ph.D. student employee, EADS Corporate Research Center, Munich, Germany
10/2006 - present:	Temporary scientifical employee, EADS Innovation Works, Munich, Germany

Publications

2003: D. de Vries, M.C. Brink, *A new bending wave analysis technique for insulation control*, German Annual Conference on Acoustics (DAGA), Aachen, 2003

2007: A.J. Berkhout, D. de Vries, M.C. Brink, *Array technology for bending wave field analysis in constructions*, Journal of Sound and Vibration, Vol. 300:25-42, 2007

2008: (*Accepted*:) R. Drobietz, M.C. Brink, I.U. Borchers, *Jet noise source distribution measurements with an acoustic mirror*, 14th AIAA/CEAS Aeroacoustics Conference (29th AIAA Aeroacoustics Conference), Vancouver, May 2008

Memberships

Member of the German Acoustics Association DEGA